5-2021

Characterization of Near Isothermal Compression and Expansion for Energy Storage

Saiid Kassaee
University of Tennessee, Knoxville, skassaee@vols.utk.edu

To the Graduate Council:

I am submitting herewith a dissertation written by Saiid Kassaee entitled "Characterization of Near Isothermal Compression and Expansion for Energy Storage." I have examined the final electronic copy of this dissertation for form and content and recommend that it be accepted in partial fulfillment of the requirements for the degree of Doctor of Philosophy, with a major in Mechanical Engineering.

Matthew M. Mench, Major Professor

We have read this dissertation and recommend its acceptance:

Matthew M. Mench, Ayyoub M. Momen, Kenneth D. Kihm, Michael W. Berry, Doug Aaron, Ahmed G. Abuheiba

Accepted for the Council:

Dixie L. Thompson

Vice Provost and Dean of the Graduate School

(Original signatures are on file with official student records.)

Characterization of Near Isothermal Compression and Expansion for Energy Storage

A Dissertation Presented for the

Doctor of Philosophy

Degree

The University of Tennessee, Knoxville

Saiid Kassaee

May 2021

It is always sunny above the dark clouds, if you fly high enough.

Acknowledgments

I am forever grateful to all who have helped me through this journey. The list would be very long to thank everyone by name and one section of the dissertation would not do it justice. I would like to start off by thanking to my two advisors. Dr. Matthew Mench at the University of Tennessee for his continuous support since my undergraduate, involving me in meetings with top aerospace companies to improve the aerospace program at UT, and for allowing me to join his research group. I am forever grateful for his mentorship and flexibility in allowing me to collaborate with ORNL on a PhD topic which I have grown to enjoy working on. And Dr. Ayyoub Momen at ORNL, for his mentorship, continuous support, constant encouragement, and enthusiasm, for allowing me to grow and learn by involving me in various projects and exposing me to all aspects of research from writing proposals, to having a seat at the table with high-level collaborators and meeting high-level officials. I am forever grateful to them both. I would like to thank my research group at Oak Ridge National Laboratory (ORNL) and the University of Tennessee for their nonstop support. At ORNL I am grateful to Ahmad Abu-Heiba for always willing to help, Yang Chen, Adewale Odukomaiya, Praveen Cheekatamarla, and Joe Rendall for many brainstorming sessions and serving as co-authors and reviewers on paper manuscripts. I am also grateful to Tony Gehl, Brandy Milun, and Jeff Taylor for their help with my experimental work. At the University of Tennessee, I am grateful to Dr. Doug Aaron and the Electrochemical Energy Storage and Conversion Laboratory group, Dr. Andy Sarles, Dr. Zhili Zhang, Dr. Mark Barker, and Dr. Farshad Rabib for many helpful conversations and encouragements during my journey. Next, I am grateful to Dr. Kenneth Kihm, Dr. Michael Berry, Dr. Doug Aaron, and Ahmad Abu-Heiba for serving as my PhD committee members and for their encouragements during my graduate studies. I would also like to thank my friends in Knoxville and all around the world and my friends and coworkers

at American Airlines. I am grateful for their friendship, memories, and help during my undergraduate and graduate studies.

I would like to thank the Department of Energy Water Power Technologies program, Building Technologies Office, and Office of Electricity for the financial support throughout my PhD journey. I am grateful to Oak Ridge National Laboratory (ORNL) and specifically Building Technologies Research and Integration Center (BTRIC) and Building Equipment Research Group for creating such positive environment for treating me as one of their own and allowing me to learn from them and grow my knowledge of their various projects. I am grateful to Oak Ridge Institute for Science and Education (ORISE) student programs Higher Education Research Experience (HERE) and Advance Short Term Research Opportunity (ASTRO) for creating the opportunity for me to experience research on this level and to allow me work along some of the best scientists in the world.

I would like to thank my family who without them none of this would be possible. Although words cannot do it justice, I would like to thank my parents Dr. Massoud Kassaee and Azam Sodagar. I am forever grateful for their unconditional love and support, for their sacrifices to help me both financially and emotionally, and for always pushing me to reach higher. I am forever grateful to my brother Hadi for paving the way before me, for his unconditional love and support, and for always pushing me to go farther no matter how crazy it sounded. I am forever grateful to my sister Fereshte for her love and support from thousands of miles away and to my sister-in-law Lena for her support.

Last but certainly not least, I would like to thank God for placing the dreams in my heart and providing the means to chase after them. Everything sure happens for a reason; dare to dream.

Abstract

As the global share of electricity generation from intermittent renewable energy sources increases, developing efficient and scalable electricity storage technologies becomes critical to modernizing the grid, matching the supply and demand, and raising the capacity factor of renewable generation. The Ground-Level Integrated Diverse Energy Storage (GLIDES) is an efficient energy storage technology invented at Oak Ridge National Laboratory (ORNL). GLIDES stores energy by compressing gas using a liquid piston in pressure vessels benefiting from employing hydraulic turbomachinery which are more efficient than gas turbomachinery. Therefore, GLIDES has higher round-trip efficiency (RTE) than Compressed Air Energy Storage (CAES). Since GLIDES employs pressure vessels, it is not geographically limited as CAES and pump storage hydro (PSH) are. Two proof-of-concept prototypes were design and built at ORNL with nominal capacity of 1 and 3 kWh. GLIDES 2nd generation prototype achieved 98.5% isothermal compression efficiency experimentally. A physics-based performance model was developed simulating the GLIDES behavior during operation and was validated using the experimental data. For cost reduction purposes, the first cost of GLIDES when employing steel vessels, carbon fiber vessels, pipe segments, and underground pressure reservoirs was modeled. The results of the cost model showed first cost as low as $\sim\$14/kWh$ and $\sim\$346/kWh$ could be achieved for a grid-scale GLIDES using depleted oil/gas reservoirs and high-pressure pipe segments, respectively. Employing the studies done on liquid piston compression and direct heat exchange with micron-sized sprayed droplets in GLIDES, a one of a kind near isothermal liquid compressor (IsoLiqComp), capable of compressing any refrigerant, is designed and developed at ORNL. A secondary physics-based performance model was developed to study the condensable gas behavior. Based on simulation results, 95% isothermal efficiency can be achieved. A 1st generation IsoLiqComp prototype was

built using a 0.005 m^3 compression chamber. The results of this research show GLIDES is a low-cost efficient energy storage technology competitive to conventional Lithium-ion and Lead acid batteries. Significant increase in compression efficiency in comparison to conventional compressors is achievable using IsoLiqComp. HVAC systems, natural gas transportation, and CO_2 extraction systems (etc.) can highly benefit from employing IsoLiqComp and the studies performed in this research.

Table of Contents

List of Tables

List of Figures

Nomenclature

Abbreviations

Bcf	Billion cubic feet
CAES	Compressed air energy storage
CF	Carbon fiber
DOE	Department of energy
ED	Energy density [kWh/m^3]
FBES	Flow battery energy storage
FES	Flywheel energy storage
GLIDES	Ground-level integrated diverse energy storage
LIB	Lithium-ion battery
ORNL	Oak Ridge national laboratory
PD	Positive displacement
PSH	Pumped storage hydroelectricity
RTE	Roundtrip efficiency

Subscripts

amb	of ambient air
avg	average
g	of gas
i	inner
l	of liquid
max	maximum
min	minimum
o	outer
t	of tank walls
v	at constant volume

Symbols

A	Heat transfer area [m^2]
c	Specific heat capacity [$J/kg.K$]
E	Energy [kWh/m^3]
G	Generator
h	Heat transfer coefficient [W/m^2K]
m	Mass [kg]
M	Motor
$\dot{m}$	Mass flow rate [kg/s]
n	Polytropic constant
p	Pressure [bar]
t	Time [s]
T	Temperature [K]
V	Volume m^3
ρ	Density [kg/m^3]
η	Efficiency

Chapter 1: Introduction

1.1 Motivation

Grid modernization is vital to the nation's safety, economy, and modern way of life. Grid modernization can reduce the societal cost of power outage by more than 10%, decrease the cost of reserve margins by 33%, and reduce the cost of wind and solar integration by 50%, providing more than $7 billion in annual benefits for the US economy [1]. On the other hand, with the increase in the release of greenhouse gases into the atmosphere and their effect on the environment, the shift from fossil fuels to renewable energies is more critical now than ever before. In 2018, around 63% of the world's total electricity production was from fossil fuels, 5% from nuclear energy and around 36% from renewable energy sources (including 23% from natural gas and 13% from other renewable sources) [2].

Based on the Renewables 2018 Global Status Report by the Renewable Energy Policy Network for the 21st Century (REN21), with the commitment to phase out coal power by 2030, more than 20 countries including Italy, Mexico, and the United Kingdom launched the Powering Coal Alliance in 2017. Along with these countries in 2017, China, the United States, and Europe provided nearly 75% of the total global investment in renewable power and fuels [3]. In addition, with the passage of US Senate Bill 100 in 2018, electric utilities and other service providers are required to increase the amount of electricity generated by renewable energies from 50% to 60% by 2030 and the state of California is required to phase out coal power and replace it with clean sources to produce 100% of its power by 2045 [4]. The challenge with renewable energies is the variability in their output, which is due to their availability (e.g., lack of sunlight at night or lack of wind). Given the unpredictability of electricity demand, the output variability of the renewable

energies, and the need for a power supply to meet the demand, the concept of energy storage is critical. Higher employment of renewable energies, grid modernization, and the global goal of decarbonizing the energy economy has increased the need for energy storage. As reported by California ISO (CAISO), in 2019, California slashed more than 950,000 MWh [5] of solar and wind power to balance supply and demand as the renewables are intermittent. To meet the electricity demand and have a low error margin, current power generation and distribution infostructures are forced to generate continuously resulting in losses during off-peak hours. The challenge with renewable energies is the variability in their output, which is due to their availability (e.g., lack of sunlight at night or lack of wind). Given the unpredictability of electricity demand, the output variability of the renewable energies, and the need for a power supply to meet the demand, the concept of energy storage is critical and by employing energy storage, the losses due to excess electricity generation can be neglected. Various energy storage technologies have been developed over the past few decades storing energy when available from the renewable sources or when cheap electricity is available during off-peak hours from the grid and using the stored energy when renewable sources are unavailable or during peak hours when electricity is expensive, aiming to improve grid reliability and meet the increase in use of renewable energies. Given the limitations associated with intermittent renewable energies and to avoid grid instability, developing low-cost, efficient energy storage systems is critical and can provide many benefits. For example, electricity generated from renewable sources, such as wind and solar, can be stored when available and used when those sources are unavailable or the price of electricity is high from the grid (grid services and peak shaving); stored when the demand is lower than the supply, such as nights when low-cost power plants continue to operate. Peak shaving is a technique used to reduce building power consumption during high-demand periods by employing behind the meter energy storage and has

the potential to lower the consumer's electric bill. Energy storage technologies can both discharge power quickly and slowly depending on the technology. Energy storage is valuable in grid stabilization, beneficial in electric vehicles, during power outages, in natural disasters, and in areas located away from the grid (e.g., islands and microgrids). To date, there are 1,600 energy storage projects worldwide (operative and in progress) with a total of around 191 *GW* of energy storage, with Pumped Storage Hydro as the highest existing capacity and electrochemical technology (batteries) as the leading technology with the highest number of projects in progress [6] [7].

1.2 State-of-the-Art Energy Storage Systems

To promote the integration of the expected growth in renewables into the electricity generation mix and grid modernization, various energy storage technologies have been developed. These technologies can be classified into four major categories: mechanical, electrical, chemical, and electrochemical [8]. The main characteristics used to compare energy storage technologies are rated power, energy capacity, energy density (ED), round-trip efficiency (RTE), and energy cost in *$/kWh*. Rated power is the maximum instantaneous power the system can output (*kW, MW, GW, etc*.); however, since the energy stored in the system is finite, the time in which the system can output the maximum instantaneous power until all energy is discharged plays an important role. Energy capacity is the numerical integration of the instantaneous power over the time it takes to completely discharge the energy stored in the system. Energy density (ED) is the amount of energy stored per unit of volume of the storage system. Roundtrip efficiency (RTE) is the ratio of the total energy that can be extracted from the system through discharging to the energy needed to charge the system to its full energy capacity. Many energy storage technologies have been deployed to date. Some of the existing energy storage technologies include but are not limited to those discussed below.

1.2.1 Mechanical Energy Storage

Some of the mechanical energy storage technologies include Pumped Hydroelectric Storage (PHS), Compressed Air Energy Storage (CAES), and Flywheel Energy Storage (FES). The technical and economical characteristics of these energy storage technologies are included in Table 1.

1.2.1.1 Pumped Hydroelectric Storage (PHS)

Pumped hydroelectric storage is the most widely used large-scale electrical energy storage. PHS technology accounts for around 97% of the world's electricity storage [9]. This technology converts electrical energy to potential energy using two water reservoirs at different elevations, a unit to pump water to the higher elevation, and a turbine to generate electricity.

During charging, a hydraulic pump is used to pump water from a lower reservoir (e.g., a lake or river) to a higher water reservoir (e.g., pond). During discharge, the elevated water can be released back into the lower reservoir. The water spins a hydraulic turbine that drives an electric generator to generate electricity [10,11].

Pumped hydroelectric storage has a relatively low capital cost, high roundtrip efficiency, and more than 40 year lifetime. The capacity of this system solely depends on the difference in elevation between the two reservoirs and the size of the reservoirs. The main disadvantage of this technology is its limited expansion prospect in the United States because most of the favorable sites have already been developed. Pumped hydroelectric storage also suffers from scalability and geographical limitations [10,11].

1.2.1.2 Compressed Air Energy Storage (CAES)

Compressed Air Energy Storage (CAES) stores electrical energy in the form of high-pressure air using gas compressors. The compressed air is stored in a container (i.e., underground caverns or aboveground tanks), and a multi-stage turbine is employed to dispatch the stored energy.

During charging, CAES use gas compressors to compress air into an underground cavern or aboveground pressure reservoir. During discharging, the compressed air is expanded through a high-pressure gas turbine. The air is then mixed with fuel, and the mixture is combusted and expands through a low-pressure gas turbine. The low- and high- pressure turbines are connected through a common shaft to a generator to generate electricity.

There are only two operating CAES facilities in the world. Both systems are cavern based. The first ever CAES plant built is in Huntorf, Germany. It uses two salt dome-based caverns as the storage reservoirs. The other operating CAES is in the United States, in McIntosh, Alabama. It uses one salt dome–based cavern. CAES technology provides good part-load performance and a reasonable response speed. However, it suffers from low roundtrip efficiency due to the usage of gas turbomachines and also suffers from geographical limitations. High construction cost is the major barrier to deploying large-scale CAES plants [10,11].

1.2.1.3 Flywheel Energy Storage (FES)

Flywheels have been used for centuries to store energy in the form of kinetic energy. A flywheel energy storage system consists mainly of a flywheel, a reversible motor/generator, and an evacuated chamber. These systems can be classified as low and high speed. The flywheels themselves are usually made of steel and an advanced composite material such as carbon fiber.

During charging, the flywheel is spun by an electric motor. During discharging, the rotational energy of the flywheel is then used to spin the same motor, which now acts as a generator, to generate electricity.

The advantages of FES include long lifetime, high roundtrip efficiency, and relatively quick charging. Normally, FES systems can supply power for a short period of time. Therefore, they are not used as standalone backup power unless they are used with other energy storage technologies. Other disadvantages of this technology include idling losses during standby time and the need for a vacuum chamber. Flywheel malfunction during rotation is common and is usually caused by the propagation of cracks through the rotors [10–12].

1.2.2 Electrochemical Energy Storage (Batteries)

Electrochemical energy storage batteries have different chemistries and include lead acid, lithium ion, sodium-based, nickel-based, and flow batteries. The first large-scale battery storage installation in the United States entered service in 2003 using nickel-based and sodium-based batteries [13]. By the end of 2017, 708 *MW* of large-scale battery storage was in operation in the United States [14]. Some of the Electrochemical Energy Storage technologies include but are not limited to Lead Acid Batteries, Lithium-ion Batteries, Sodium-Sulfur Batteries, and Flow Battery Energy Storage. The technical and economical characteristics of these energy storage technologies are also included in Table 1.

1.2.2.1 Lead Acid Batteries

Lead acid batteries use two electrodes—one is composed of highly porous lead dioxide (PbO_2) and the other of finely divided metallic lead (Pb). The lead-dioxide electrode is the positive electrode, and the metallic lead is the negative electrode. The two electrodes are submerged in an

electrolyte solution of dilute aqueous sulfuric acid. The negative electrode reacts with the hydrogen sulfate ion (HSO_4^-) of the electrolyte and produces lead sulfate ($PbSO_4$), hydronium ions (H_3O^+), and electrons (e^-). The positive electrode reacts with the hydrogen sulfate ion of the electrolyte, hydronium ions, and electrons to produce lead sulfate and water.

Lead acid batteries are the most popular low-cost batteries. Their RTE is around 70%. The disadvantages of these batteries, compared to other battery technologies, include relatively low cycle life (50–500 cycles), and the possibility of corrosion [12].

1.2.2.2 Lithium-ion Batteries

Lithium-ion battery (LIB) technology is based on the use of lithium-intercalation compounds. A cathode, the electrode where a reduction reaction takes place and electrons enter the cell, is a lithiated metal oxide (an oxide due to higher potential) that is often characterized by a layered structure. An anode, where an oxidation reaction takes place, is made of graphitic carbon which holds lithium in its layers. Both electrodes are capable of reversibly inserting and removing lithium ions from their structure.

Lithium-ion batteries outperform other electrochemical energy storage technologies by a factor of 2.5 in terms of energy capacity while providing high specific power. Over the last decade, the energy density of lithium-ion batteries has improved from 100 kWh/m^3 to around 730 kWh/m^3 [15]. The high energy density, around 97% roundtrip efficiency, relatively long life, and rapid charging of lithium-ion batteries have made them the first choice for powering electric vehicles [8,10,11]. Lithium-ion batteries suffer from degradation of maximum charge storage at high temperatures, thermal runaway and capacity loss when overcharged, and chemical and fire hazards [12].

1.2.2.3 Sodium-Sulfur Batteries

Sodium-sulfur batteries are an energy storage technology with the potential for use in grid support due to their long discharge period. Sodium-sulfur batteries use molten sodium as the anode (negative electrode), molten sulfur as the cathode (positive electrode), and beta alumina as the conducting solid electrolyte. These batteries operate at a temperature range of 270℃ to 350℃. Hazardous materials, including metallic sodium, which is combustible when exposed to water, are used in sodium-sulfur batteries. This requires sodium-sulfur batteries construction to be airtight, double-walled, and sealed in stainless-steel enclosures. These enclosures contain arrays of sodium-sulfur cells to mitigate fire and to anchor the cells. These cells are sealed and surrounded with sand [12].

1.2.2.4 Flow Battery Energy Storage (FBES)

Flow batteries can be classified to redox flow batteries and hybrid flow batteries. The power of flow battery energy storage systems, unlike other electrochemical technologies, is independent of its storage capacity and is determined by the number of cells in the stack and the size of the electrodes used. The storage capacity of these systems is based on the concentration and the volume of the electrolyte used, meaning the system capacity can be increased by simply increasing the volume of reactants used or by increasing the electrolyte concentration [11]. Redox flow batteries use two circulating soluble redox couples as the electroactive species contained in external liquid electrolyte tanks. The simplicity of the reactions is distinct from other battery chemistries. Other batteries typically involve phase change, electrolyte degradation, and electrode morphology changes. There have been few field demonstrations of redox-flow batteries to date. The electrolytes, the electrodes, tanks, pumping systems, structure, power electronics, and controls have a longer lifespan than the cell stack, making the cell stack the life-limiting component of

redox-flow batteries. Other drawbacks include nonuniform pressure drops (pressure drop due to the flow of electrodes in channels) and the limitation in the reactant mass transfer, causing low system performance, high manufacturing costs, and low energy density [8,11,12].

1.3 US Department of Energy's Energy Storage Goal

The DOE's 2010 "ARPA-E's Grid-Scale Rampable Intermittent Dispatchable Storage (GRIDS) program [16] focused on development of low-cost storage technologies for the electric grid. Specifically, GRIDS aimed to address the challenge of renewable generation ramping. Initiated in 2010, ARPA-E's GRIDS program is aimed at developing new storage technologies at a capital cost of less than *$*100 per *kilowatt-hour* that can scale to store *megawatt-hours* of electricity and be used at any location on the grid" [17]. Therefore, there is a need for a low-cost high-RTE high-energy-density dispatchable energy storage system that can meet the DOE's target.

As explained above, CAES suffers from low efficiency of around 54% [19]. CAES also suffers from low efficiency due to employing gas turbomachinery, heat loss during the compression process, and need for heat addition during the expansion process. With rapid air compression to high pressures and minimal heat transfer using the conventional gas compressors, high amount of energy is converted into increasing the air temperature [22]. This increase in temperature decreases the compression efficiency as at the end of the compression process, as air temperature drops, the air pressure and compression efficiency decrease. To improve the CAES efficiency, variety of different CAES applications have been studied including Diabetic CAES (DCAES), Adiabatic CAES (ACAES), and Isothermal CAES (ICAES) [23]. In DCAES the heat generated during the compression process is dissipated and lost to the ambient as the compressed air would not be discharged immediately; and external heat source is used to increase air temperature prior to expansion to prevent any condensation or icing. The two existing CAES plants use this

Table 1, Technical and economical characteristics of energy storage technologies.

Technology	ED (kWh/m^3)	Rated (MWh)	Lifetime (Years)	RTE %	Discharge Time ($hours$)	Energy cost ($/$kWh$)
PHS [18,19]	0.2–2	400-32,000	30–60	70–85	4-16	106-200 5–100
CAES [18,19]	2–6	200-30,000	20–40	40–70	20-30	94-229
Flywheel [19–21]	20–80	<0.1	~15+	85–95	15 s–15 min	4,320- 11,520 1,500–6,000
Lead-acid [18,19]	50–80	0.001–800	5–15	50-90	< 10	358-631
Li-ion [9,19,20]	200–400	0.001–2,000	5–15	90–95	~1 min–8 h	393-581 360–1200
Na-S [19–21]	150–300	0.01–800	10–15	70–90	~1	599-1,293 263–735

mechanism. On the other hand, in ACAES the heat generated during the compression process is stored in thermal energy storage (TES) and used prior to expansion and eliminate the need for external heater. In ICAES, it is proposed to minimize the heat generated during the compression process and achieve near-isothermal compression, increasing the compression efficiency [23]. Liquid Air Energy Storage (LAES) is another energy storage technology which stores energy by liquifying air and storing at low pressure in insulated vessels [24]. LAES suffers from low efficiency as gas turbomachinery are used.

Research has been performed on various ways to increase compression efficiency to achieve near-isothermal compression as it requires less work to achieve the same pressure ratio as an adiabatic process. As conventional mechanical gas compressors and combustion engines suffer from poor heat transfer due to high frequency and low heat transfer from the gas to the surroundings, other ideas have been proposed to increase the surface area to volume ration of the gas [22]. Coney et al. described the development of a reciprocating compressor with water injection capability and built a prototype along simulation model and reported compression up to around 25 bar maintaining the temperature below 100 ℃ compared to 500 ℃ of an adiabatic compression [25]. Van de Van et al. proposed employing liquid piston in multi-chamber gas compressor to improve compression efficiency and reported increase in compression efficiency from 70% to 83% based on a simulation model (no experimental data was reported) [22]. To farther increase the compression efficiency of liquid piston Van de Van et al. had proposed, Qin et al. proposed addition of spray droplets to a liquid piston on top of reciprocating piston and reported 98% compression efficiency based on simulation modeling validated using experimental data of addition of spray droplets to shock waves (no prototype was built) [26,27]. Patil et al. experimentally investigated the heat transfer in a liquid piston compressor by employing a

hydraulic pump to pump water into the compression chamber as the liquid piston and to spray water into the chamber compressing air to 70 psi (4.8 bar) maximum pressure and reported 95% isothermal compression efficiency [28]. The applications of employing liquid piston and spray injection compression mentioned above are all used in low-pressure fast-stroke gas compressors. As air compressed to 300 bar has energy density comparable to that of lead-acid batteries [29] and hydraulic turbomachinery have high efficiencies around 90% , the hydropneumatics energy storage system of interest, Ground-Level Integrated Diverse Energy Storage (GLIDES), is designed as a combination of pumped storage hydro and compressed air energy storage which stores energy by gas compression using a spray piston and employing spray compression and using a liquid piston to achieve more than 98% isothermal compression efficiency. In the next chapter, the GLIDES concept is explained along introduction of the two proof-of-concept prototypes and detailed analysis of experimental and simulation analysis of near-isothermal spray compression employing the 2nd generation prototype built at ORNL.

Chapter 2: Ground-Level Integrated Diverse Energy Storage, GLIDES

Ground-Level Integrated Diverse Energy Storage (GLIDES) is an energy storage system that was invented at the Oak Ridge National Laboratory (ORNL) [30]. GLIDES stores energy by compression and expansion of air using water as a liquid piston inside high-pressure reservoirs. This system is a combination of CAES and PHS systems but is more efficient and has higher energy density than either technologies. As shown in Figure 1, the GLIDES system consists of a hydraulic motor, a hydraulic pump, high-pressure reservoirs (i.e., pressure vessels), a hydraulic turbine, and an electrical generator. The high-pressure reservoirs in this system are sealed vessels. These high-pressure reservoirs are pre-pressurized with air to a certain pressure. The choice of this initial pressure is explained in section 7.3. During charging, an electric motor is run which drives a positive displacement (PD) hydraulic pump. The pump pushes water into the pressurized reservoirs. With the water volume increasing inside the high-pressure reservoirs, the air above the water is compressed, causing its pressure to increase and storing energy. During discharging, water is discharged from the vessels, causing the air above the water column to expand. The water flows through a hydraulic turbine that drives an electric generator, and electricity is generated. Multiple lab-scale prototypes of GLIDES have been built at ORNL since 2015 [31] and a preliminary analysis of market potential of the GLIDES system including a mathematical model is introduced in [32]. The first prototype was built with a system nominal size of 3 kWh. This system consisted of an ambient pressure water storage, electric motor, electric generator, PD hydraulic pump, four steel high-pressure vessels, and a hydraulic Pelton turbine. Use of a hydraulic PD pump and Pelton turbine to charge/discharge the GLIDES system is one of the main advantages over CAES systems as no gas turbomachinery used, resulting in much higher roundtrip efficiency. The GLIDES system is easily scalable and dispatchable. The storage capacity can be increased by simply adding high-

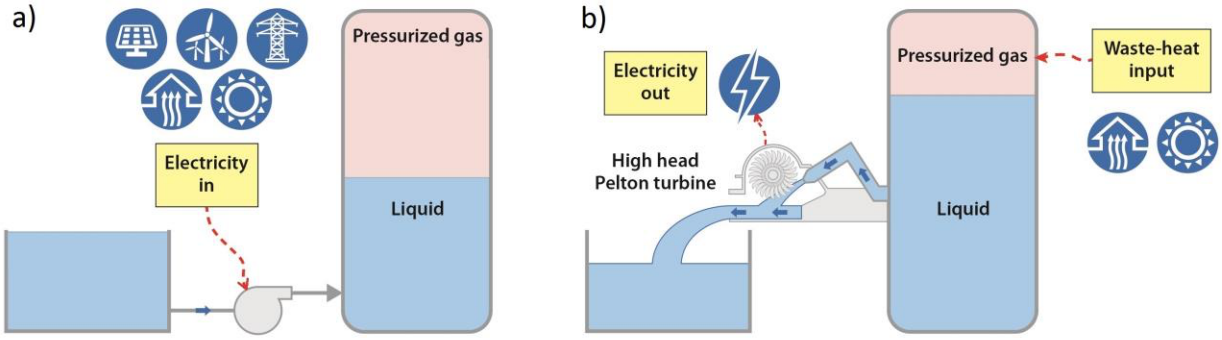

Figure 1, The invented GLIDES layout during (a) charging and (b) discharging [31].

pressure storage volume (i.e. more vessels). The power capacity can be increased by using larger hydraulic machines, or several in parallel. The proof-of-concept prototypes are described in the following sections.

2.1 GLIDES Proof-of-Concept Prototypes

2.1.1 1st Generation Prototype

The first-generation proof-of-concept prototype of the GLIDES technology was developed at ORNL using four 500-liter carbon steel pressure vessels, an 11 kW electric motor, a 42 LPM positive displacement pump, two Pelton turbines, and a 5 kW single phase 120 VAC 60 Hz electrical generator [33]. As shown in the experimental data reported by [31] (Figure 2.a), the air temperature increases by around 45℃ during the charging process. This increase in air temperature, as explained before and although not as high as adiabatic compression in CAES, decreases the compression efficiency. This loss due to the increase in air temperature can be shown as the area enclosed between the curves from 1 to 2 (compression process) and 3 to 4 (expansion process) on the P-V diagram shown in Figure 2.b. Other losses in the 1st generation prototype include losses in motor, 30-40% losses from the pump, 50% losses from the turbine and 25-32% losses from the generator [33]. To explain in more detail why the increase in gas temperature increases the losses in the system, the P-V diagram shown in Figure 3 was made. As seen in Figure 3, comparing two different compression processes, adiabatic and isothermal compression, it can be seen that starting at the same gas volume and pressure (point 1), at the same compression rate (inlet water flow rate), the maximum gas pressure is reached faster during an adiabatic compression (point 2), meaning less water is pumped into the vessel than during an isothermal process (lower volume ratio) due to the increase in air temperature causing the air pressure to

increase at a faster rate. As the charging stops, during the pause process (the time between charging ends and discharge begins), after an adiabatic compression, as the air temperature inside the vessel is higher than the ambient, heat transfer occurs between air and water in the vessel and the surrounding ambient air through the vessel walls and therefore air temperature drops (if not isolated). As the gas temperature decreases, the gas pressure drops as well. This drop in gas pressure during the pause process results in lower available output power during the discharge process and therefore lower system efficiency.

It is therefore desired to achieve isothermal compression during GLIDES charging process to increase the compression efficiency. To achieve near-isothermal compression, other configurations of the GLIDES system were introduced by Odukomaiya et al. [31]. As shown in Figure 4, compression using the first configuration (Figure 4, a), is done by pumping water into the vessel from the bottom of the vessel (same as the compression using the 1st prototype). To achieve near-isothermal compression, the second configuration is introduced which employs spray cooling during the compression process (Figure 4, b). This configuration is set to pump water to the top of the vessel and spray into the vessel. As the water is sprayed into the vessel, each micro size sprayed droplet has direct heat exchange with the compressed air while traveling from the top of the vessel to the water level. As the water level rises in the vessel, water acts as a liquid piston and air compression takes place. The third configuration (*Figure 4*, c) represents the discharge process. As the air temperature decreases during the discharge process, a third configuration is proposed which employs a circulating pump and an active heat exchanger to achieve near isothermal expansion/discharge and other cycles. With this configuration, during the discharge process, some of the water leaving the pressure vessel goes through the hydraulic turbine and some gets pumped to the top of the pressure vessel and sprayed into the vessel to prevent decrease in air

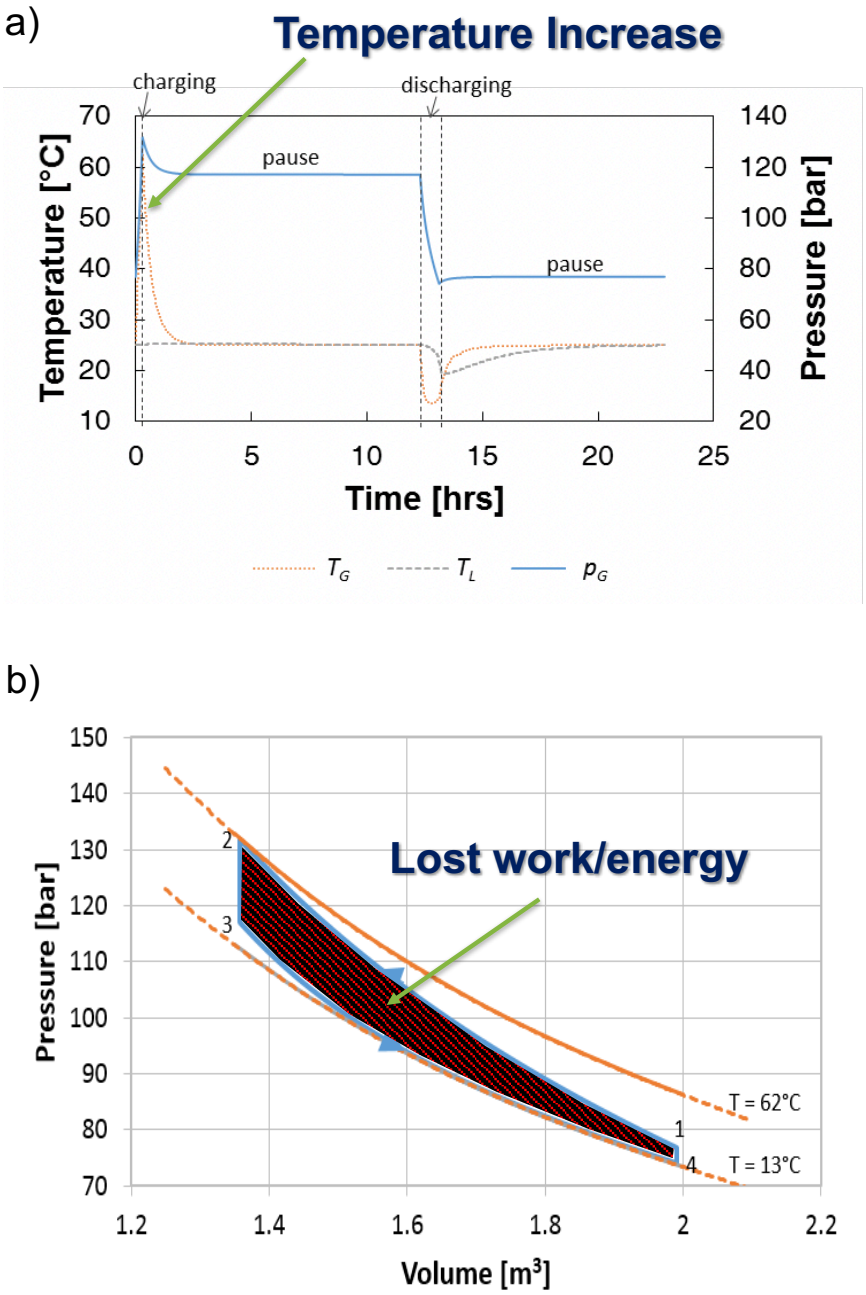

Figure 2, a) Air and water temperature (left axis), and air pressure (right axis) during a complete GLIDES run. b) GLIDES 1st generation prototype experimental full-cycle P-V diagram [31].

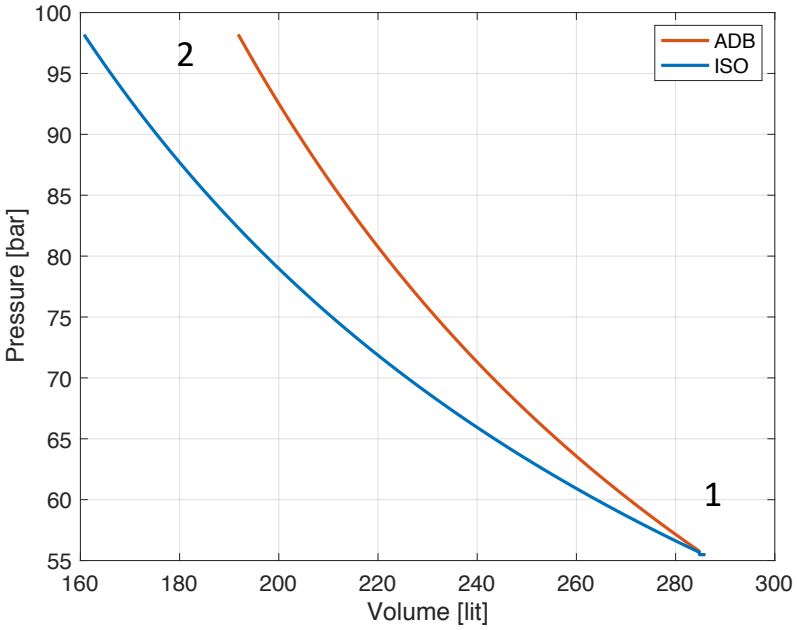

Figure 3, P-V diagram showing the pressure difference at the same final air volume.

temperature.

To achieve isothermal compression and expansion using the second and third configuration and to showcase GLIDES scalability, a 1 kWh 2nd generation proof-of-concept GLIDES prototype was built at ORNL. This prototype was built using a carbon fiber pressure vessel as the pressure reservoir.

2.1.2 Experimental Set Up / 2nd Generation Prototype

GLIDES 2nd generation prototype (shown in Figure 5) is a 1 kWh system which consists of a high-pressure vessel, a 200-liter atmospheric-pressure water tank, a reversible electric motor/generator which works as a motor during the charging process and as a generator during the discharge process, a reversible hydraulic pump/turbine which works as a hydraulic pump during charging and as a hydraulic turbine (motor) during generation. Employing reversable motor/generator and pump/turbine decreases the losses in turbomachinery as both more efficient parts are used and instead of four parts, as in the 1st generation prototype, only two parts are employed. The pressure vessel selected for this prototype is a Luxfer 287-liter polymer lined carbon fiber pressure vessel capable of handling pressures up to 248 bars. The reversible electric motor/generator is a 2 horsepower, 115/208-230 volts, 60 Hz brushless permanent magnet motor/generator and the reversible positive displacement hydraulic pump/turbine is a 1.7 kW, 4 cm^3/revolution axial piston hydraulic pump. The piping and instrumentation diagram (P&ID) of GLIDES second generation prototype is shown in Figure 7. As explained above, this system consists of a water tank, a hydraulic pump (PM1), the pressure vessel, and a second pump which is added on a secondary flow path (explained in future research). Two pressure relief valves were installed on the system for safety including one on the pressure vessel and one on the pump. The lines shown in the diagram all represent ½" high-pressure stainless-steel tubing. Several instruments including

pressure transducers and thermocouples were added to the system for data collection purposes. Motorized valves with 5 seconds cycle time, manual valves, and check valves were also added to the system to control the flow. Also, a full cone spray nozzle with spray angle of 80-85 degrees, producing droplets with average diameter of 50-660 μm is added to the top of the pressure vessel to break the flow entering the vessel from the top. A LABVIEW environment was modeled as well to collect the data using the DAQ system. The list of the pressure transducers, thermocouples, the valves, and their functions are shown in Table 2.

2.1.2.1 P&ID Charging Process

The first step before storing energy in GLIDES is to pressurize the vessel with air. The analysis on the best initial pressure was done in [34] and is shown in section 7.3. GLIDES 2nd generation prototype can be charged two ways (Figure 8). First way being the first configuration (Figure 4 ,a) which is to pump water into the vessel from the bottom of the vessel (same way as the first prototype). To charge GLIDES using this method, manual valves MV1, 2, 4, and 6 along motorized valve M2 are opened while keeping all other valves closed. The reversable electric motor/generator, acting as a motor, runs the reversable hydraulic pump/turbine (PM1), acting as a pump, pumping water into the pressurized vessel, compressing the air on top, and storing energy. The second way of charging GLIDES 2nd generation prototype is to use the second configuration (Figure 4, b). To charge the system using the second configuration with spray cooling, manual valves MV1, 2, 4, and 5 along motorized valve M3 are opened (while all the other valves remain close), water is pumped to the top of the vessel and sprayed into the vessel through the spray nozzle. As the water level rises in the vessel, the air on top is compressed and energy is stored.

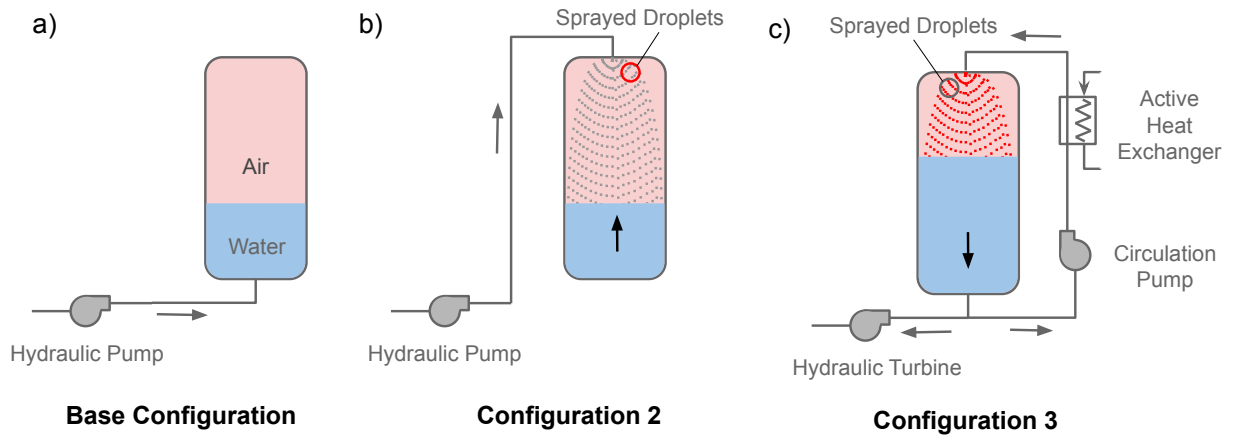

Figure 4, GLIDES a) Base, b) 2nd, and c) 3rd configuration.

Figure 5, GLIDES 2nd generation proof-of-concept prototype.

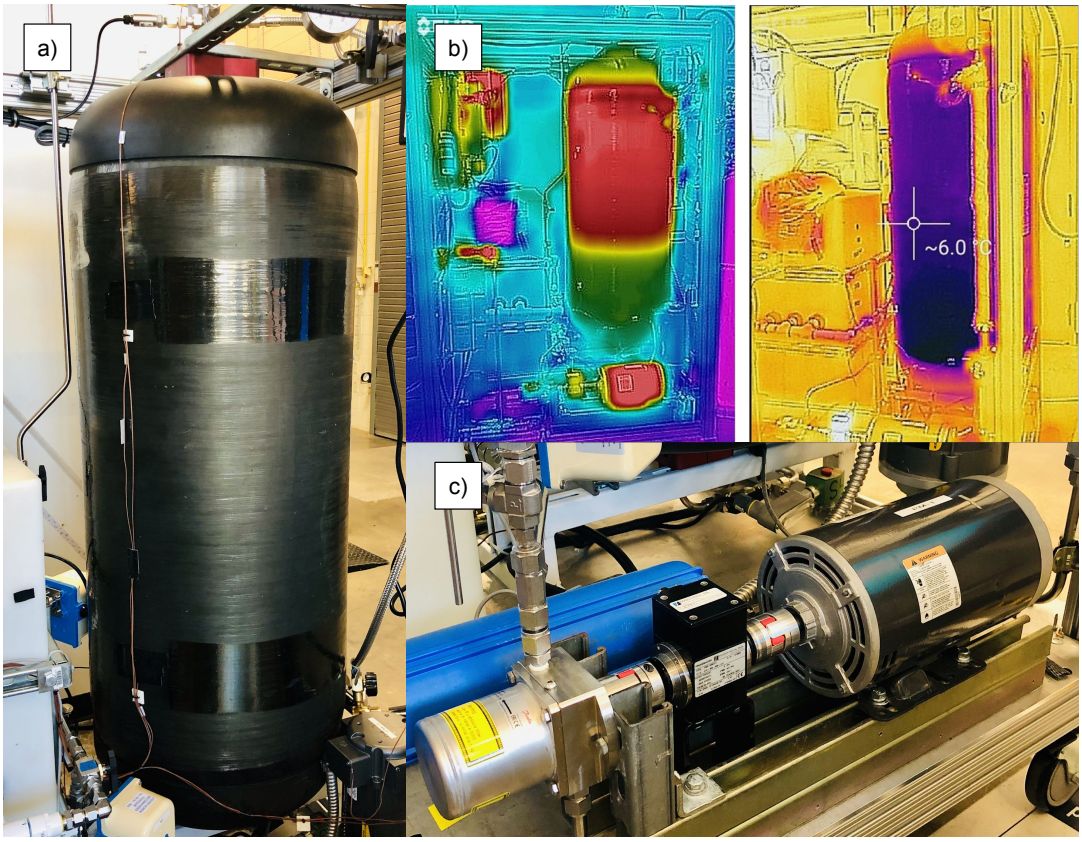

Figure 6, GLIDES 2nd generation prototype.

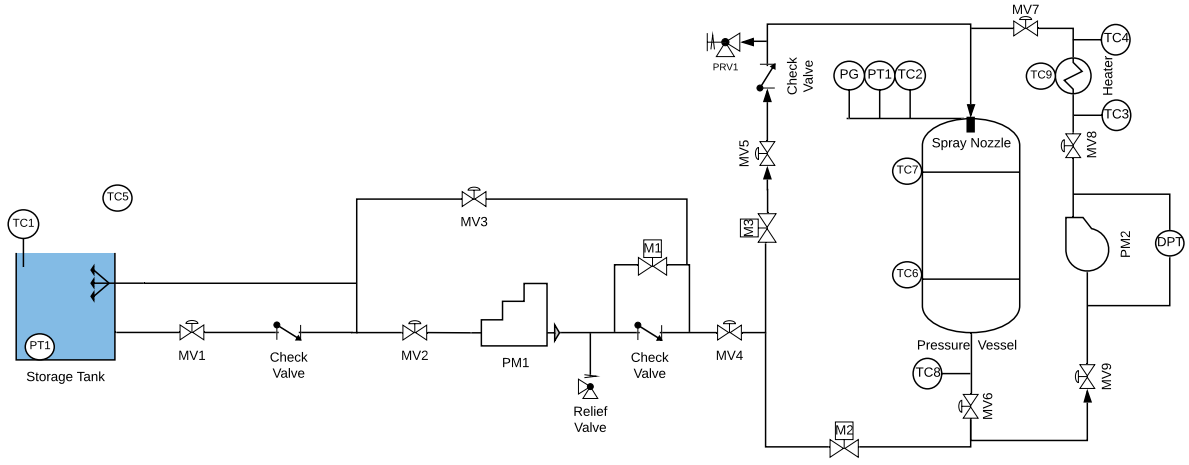

Figure 7, GLIDES 2nd generation piping and instrumentation diagram (P&ID).

Table 2, Instrumentation summary.

P&ID Code	Function
Thermocouples	
TC1	Storage tank water temperature
TC2	Pressure vessel air temperature
TC5	Ambient temperature
TC6	Lower vessel temperature
TC7	Upper vessel temperature
TC8	Water temperature below vessel
Pressure Transducers	
PT1	Storage tank water level
PT2	Air pressure inside the vessel
Motorized Valves	
M1	Controls the water flow from the pressure vessel to PM1
M2	Controls the flow below the vessel
M3	Controls the flow from the top of the vessel
Manual Valves	
MV (1-9)	Manually directing the flow

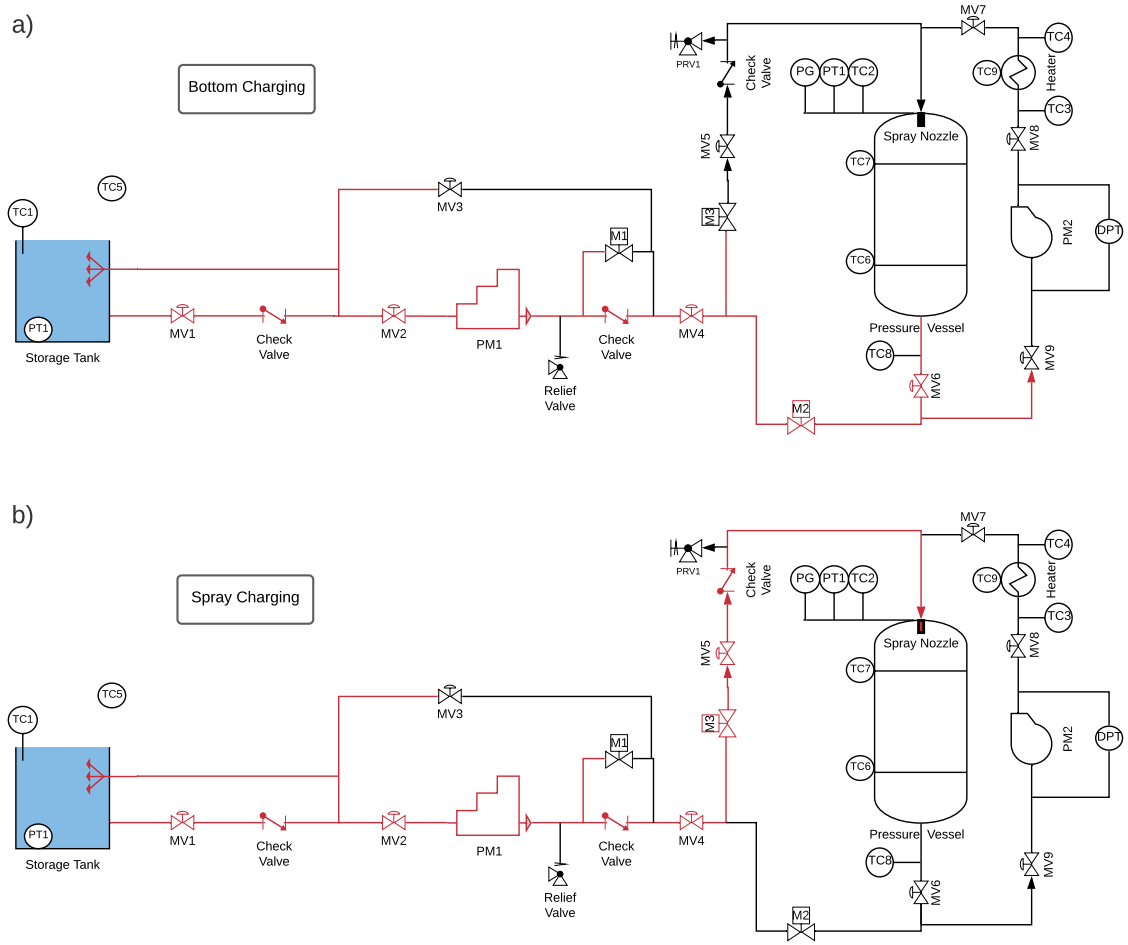

Figure 8, GLIDES 2nd generation prototype P&ID. Charging using a) 1st configuration, b) 2nd configuration.

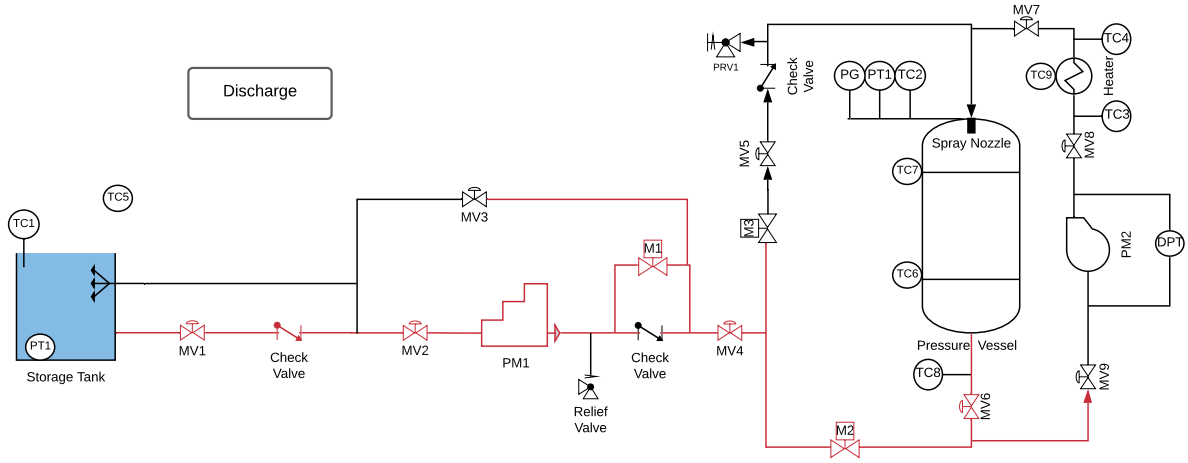

Figure 9, GLIDES 2nd generation prototype P&ID, discharge.

Chapter 3: Experimental Data Employing Spray-Cooling

To study the thermodynamic behavior of the 2nd generation prototype, various experiments were conducted. The experimental data collected during these studies are presented in this section.

The first experiment conducted was to run the prototype using the first configuration. To do so, the vessel was pressurized to an initial air pressure of 35 bars. Using the ideal gas law at room temperature, around 12 kg air exists in the pressure vessel. During the operation of the system, a torque meter is used to read the actual speed of the motor/generator (rpm). Based on these data and the equations provided by the pump manufacturer, the actual effective flow rate (Q_{eff}) entering the pressure vessel is calculated. The flow rate (Q_{eff}) at various pressure (P) can be calculated using Equation (1) [35].

$$Q_{eff} = Q_{th} - [(Q_{th} - Q(P_{max})) \times (P/P_{max})] \quad (1)$$

$$Q_{th} = \frac{V \times n}{1000} \quad (2)$$

Where

- Q_{th}: Theoretical flow (l/min)
  - V: Displacement (cm^3/rev)
  - n: Motor speed (rpm)
- $Q(P_{max})$: Flow rate at maximum pressure (l/min)
- P_{max}: Maximum pressure (barg / psig)
- P: Pressure (barg / psig)

Setting the motor to a speed of around 1090 rpm, flow rates of around 4 l/min was achieved. As explained above, the flow rate was affected by the pressure, but since a positive displacement pump is used, the change in flow rate was insignificant. With 4 l/min flow rate, 30 bars initial air pressure, and 21℃ initial air temperature, the charging began. Using the data collected, the pressure-volume (PV) diagram of the GLIDES full-cycle is plotted and shown in Figure 10.

As seen in Figure 10, starting from point 1 initial conditions, with the decrease in air volume, the air pressure increases from 35 bars to 87 bars. Charging can be continued to desired pressure while the pressure is lower than the maximum allowable pressure specified by the manufacturer. For this experiment, charging was stopped at around 87 bars pressure and 45℃ temperature. As the charging is stopped at point 2, the pause process between the end of the charging and start of the discharge process is shown between 2 and 3. From 3 to 4 discharge takes place. As the air volume is expanded, air pressure drops as well as the air temperature. During this experiment, discharge was continued until (almost) no water was left in the vessel. Charge and discharge can be done continuously or can be broken down to meet electricity demands. As the discharge comes to an end, the second pause process takes place before charging restarts. It should be mentioned that based on the electricity needs, the pause processes can be neglected.

As seen in Figure 10, the area between the top curve (compression) and the bottom curve (expansion) marks the heat transfer losses during both the compression and the expansion process. The temperature and pressure profile of this experiment are shown in Figure 11.

It can be seen during the charging process, as the pressure increases, the air temperature increases from 21℃ to around 45℃ and as the charging process stops, the air temperature drops to room temperature after around 6 hours. This loss in temperature during the pause process is the cause of the drop in pressure and therefore, the drop in available energy to discharge and lower compression

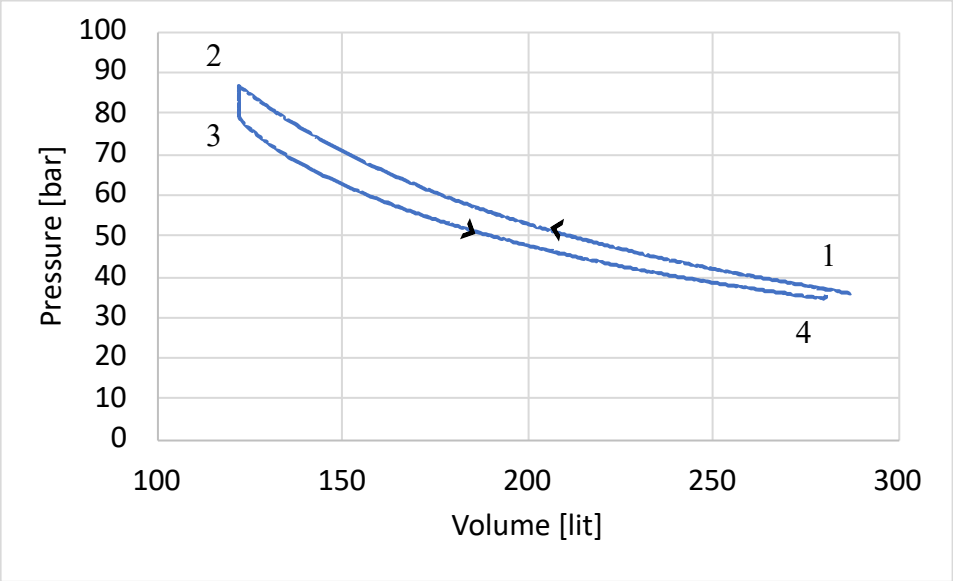

Figure 10, 2nd generation GLIDES full cycle using the base configuration.

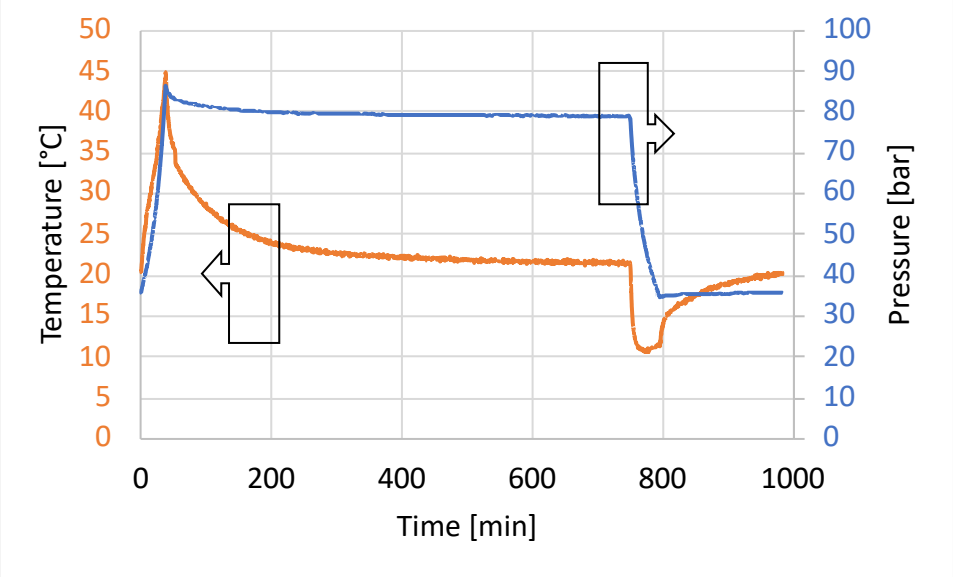

Figure 11, Base-configuration full-cycle temperature (left axis) and pressure (right axis) vs. time, first experiment.

efficiency. The second experiment employed spray cooling as in the second configuration. For this experiment, the pressure vessel was filled with 10 kg of air at initial conditions of 30 bars pressure and 22℃ temperature. Running the motor at 1172 rpm for this run, the effective flow rate was calculated to be around 4.5 LPM. Based on the data provided by the manufacturer and the PM1 flow rate, the pressure difference across the spray nozzle varies between 0 and 1 MPa. This pressure difference has been implemented in pressure and flow rate calculations. Calculations were also done on pressure losses due to the excess piping needed, but since this pressure drop was insignificant, it was neglected. During this run, as shown in Figure 12, compression was done from 30 bars to 87 bars air pressure from 287 liters to 100 liters air volume respectively. During the charging process of this experiment, an interesting trend occurred to the temperature profile. As shown in Figure 13, during the compression process, the air temperature decreased from 21.1℃ to 18.9℃ instead of increasing or constant (isothermal condition), but right after charging stopped, the temperature jumped to around 23.4℃. After analyzing the data, it was discovered the water temperature being pumped into the pressure vessel dropped during the charging process. As the charging is in process, as the water level in the water reservoir drops below around 50 cm, the pump cavitates. To prevent this from happening and still achieve the desired air pressure in the vessel, buckets of tap water were added to the water reservoir. Analyzing the data, it was clear that the air temperature followed the pattern of the water temperature (TC1) which as the buckets of tap water were added decreased by 4℃. On the other hand, as there is no drop in vessel wall temperature (TC7), the jump in air temperature at the end of the charging process cannot be from heat transfer from the vessel walls to the compressed air. Therefore, since this increase in air temperature occurs over around 30 seconds after charging has stopped, it is concluded the temperature reported by the thermocouple inside the vessel is affected by contact with the water

droplets and it can be assumed that the actual air temperature rises to the value reported at the end of the 30 seconds temperature increase. Although there is an increase in air temperature during the charging process, this increase is not significant and the maximum temperature during this run is around 23.4℃ making this an overall 2.3 degrees increase in air temperature (near isothermal with a polytropic constant of 1.0085 (isothermal = 1)). As anticipated, less than 1 bar air pressure was lost during the pause process decreasing the thermodynamic losses compared to the first experiment.

As explained, the change in water temperature due to adding tap water had a high impact on air temperature during the compression process. To study the behavior of the system without the effect of change in water temperature, a third experiment was conducted. To prevent cavitation and still have enough water to achieve a desired high pressure, a couple of buckets were filed with tap water and were left overnight to be in equilibrium with ambient temperature. For this experiment, the vessel was filled with 18 kg of air at an initial pressure of 55 bar and initial temperature of 21.7℃. Setting the motor to 1177 rpm, compression starts using spray charging with an average flow rate of 4.4 l/min and is continued to a maximum pressure of 98 bars. During the compression process, as seen in Figure 14, the air temperature increases from 21.7℃ to a maximum temperature of 26.3℃, which is a 5.4 degrees increase in air temperature; making this a near isothermal compression with a polytropic constant of 1.03.

GLIDES 2nd generation prototype roundtrip efficiency depends mainly on indicated efficiency which is highly dependent on the compression efficiency, motor/generator, and pump/turbine efficiencies. Figure 16 and Figure 17 show the change in indicated (multiplication of pressure and flow rate) and shaft power (multiplication of torque and speed) on the left axis and pump efficiency ($\frac{Q_{eff}}{Q_{th}}$) on the right axis vs. time and pressure respectively.

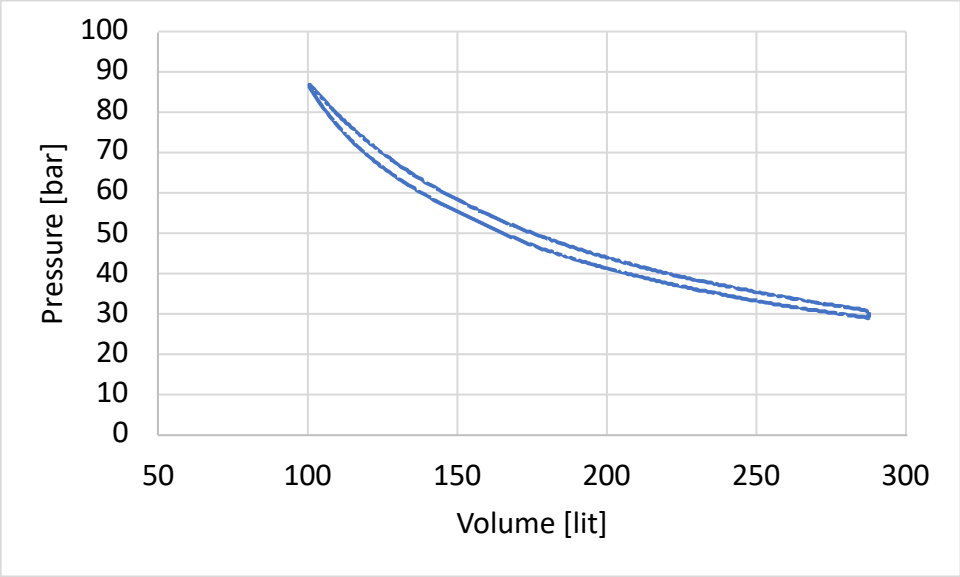

Figure 12, 2nd generation GLIDES full cycle PV using spray cooling, 2nd experiment.

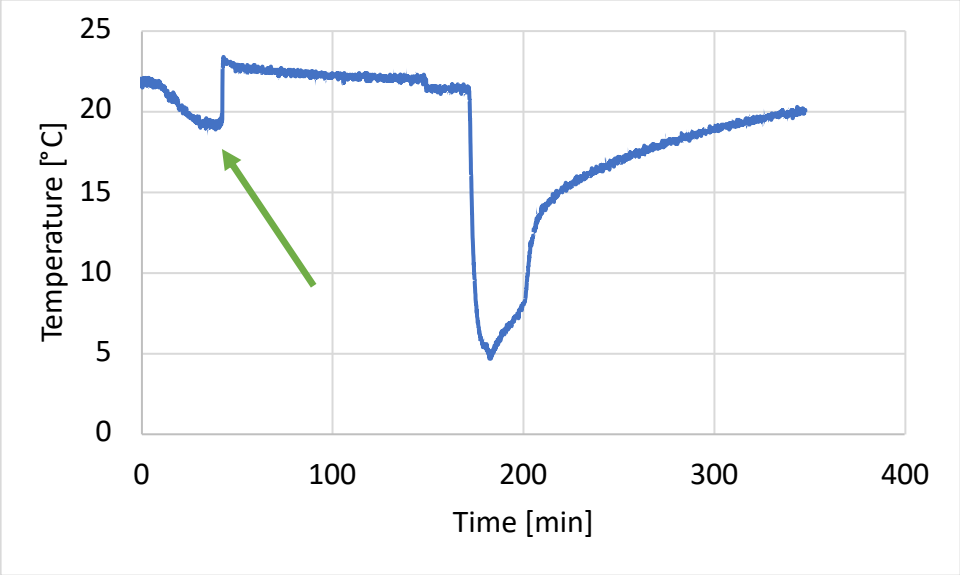

Figure 13, 2nd generation GLIDES full cycle air temperature vs. time using spray cooling, 2nd experiment.

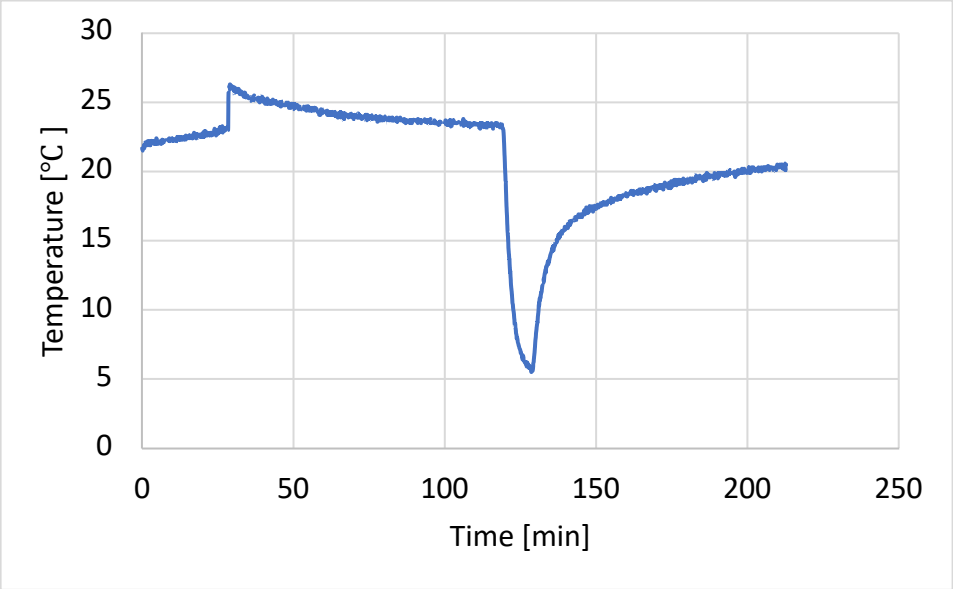

Figure 14, 2nd generation GLIDES full cycle air temperature vs. time using spray cooling, 3rd experiment.

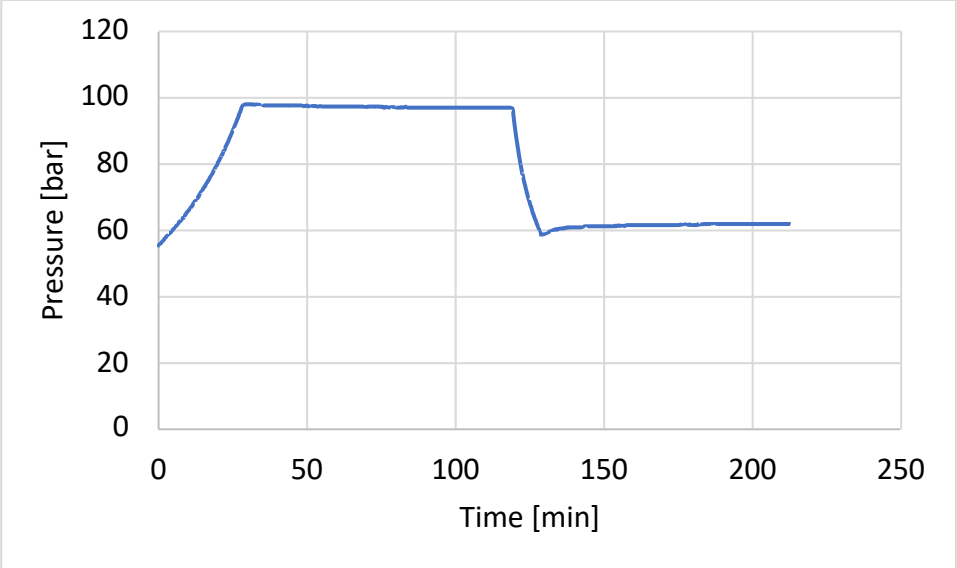

Figure 15, 2nd generation GLIDES full cycle air pressure vs. time using spray cooling, 3rd experiment.

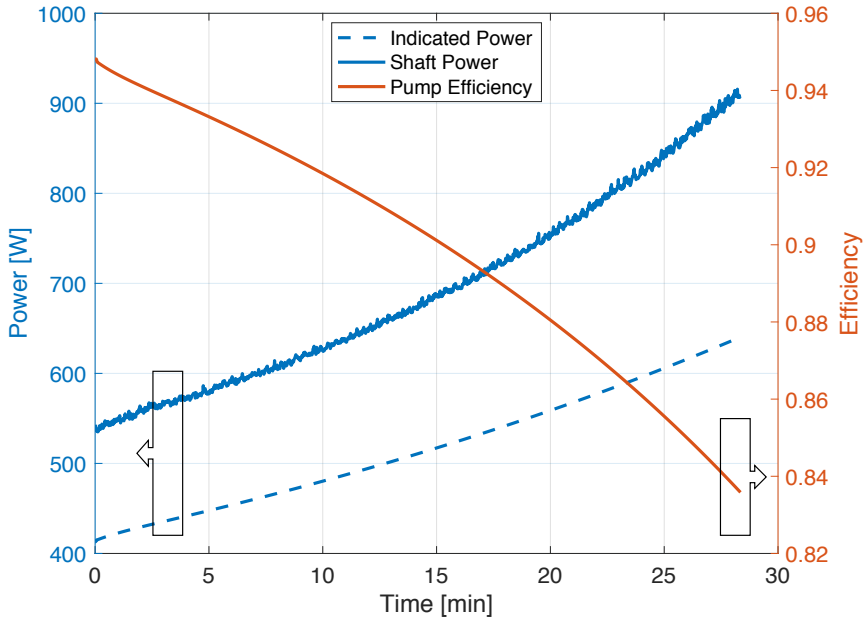

Figure 16, Indicated and shaft power (left axis) and pump efficiency (right axis) vs. time.

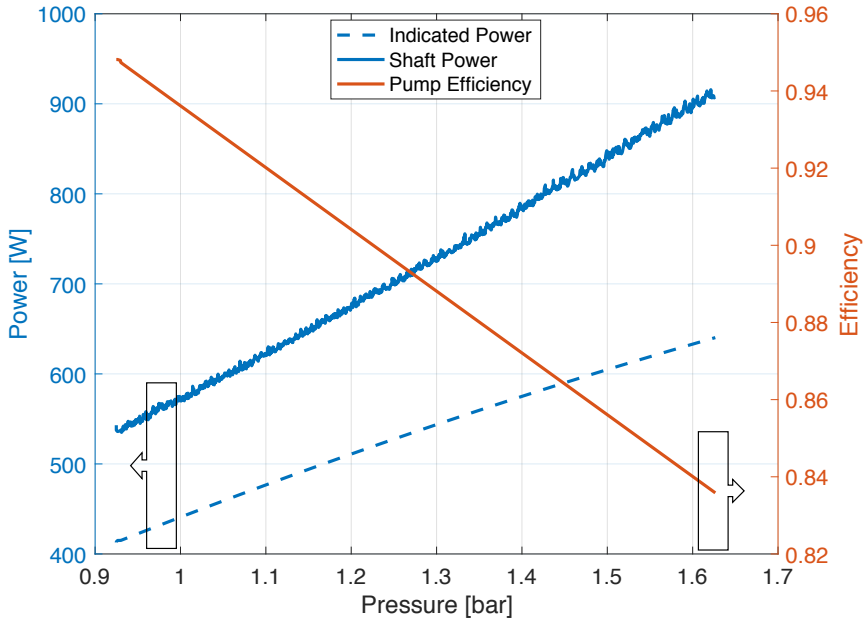

Figure 17, Indicated and shaft power (left axis) and pump efficiency (right axis) during the charging process vs. pressure.

The losses due to the turbomachinery can be seen as the area between the shaft and indicated power. Comparing the power used to charge GLIDES 1st and 2nd generation prototypes (1st generation data reported by Odukomaiya et al. [33]), the indicated power required to charge the 1st prototype is more than 10 times higher than that required to charge the 2nd prototype. It should be mentioned, as the 1st prototype has four pressure vessels, higher power is required.

Chapter 4: Simulation Model

A physics-based performance model was developed to match the experimental data collected employing the GLIDES 2nd generation prototype using spray cooling. The physics-based performance model takes 1. Vessel specifications, 2. Air mass, 3, Initial temperature, 4. Initial pressure, 5. Motor speed, 6. Desired maximum pressure, and 7. Pause times as inputs and simulates the four parts of the GLIDES operation, charging process (compression), pause time after charging, discharge (expansion), and the pause time after the discharge ends. The model, developed in MATLAB, uses various equations and energy balances developed by [31] to simulate, in detail, the system behavior and heat transfer from the compressed air to the water droplets, to the water level in the vessel, and to the surrounding vessel walls and ambient. The model is developed using four while-loops.

As explained above, the model simulates three main thermal masses including air, water, and vessel walls Figure 18. The vessel walls are split into two sections, one in contact with air and the other in contact with the rising water. To simulate the behavior of these masses, energy balance was done on each of them. The energy equation for air simulates the convection heat transfer between air and the sprayed droplets, air with the rising water level, air with the vessel walls and the ambient, and the compression work done on the air. Equation (3) shows air's energy equation where the term on the left is the time rate of change of contained energy in air, the first term on the right represents the rate of heat transfer between air and water, the second term on the right is the net rate of heat transferred from the compressed air to the tank walls and the ambient during the charging process, the third term on the right is the rate of heat transfer from the compressed air to the sprayed droplets, and the last term on the right is the rate of work done on the air by the rising water level [31].

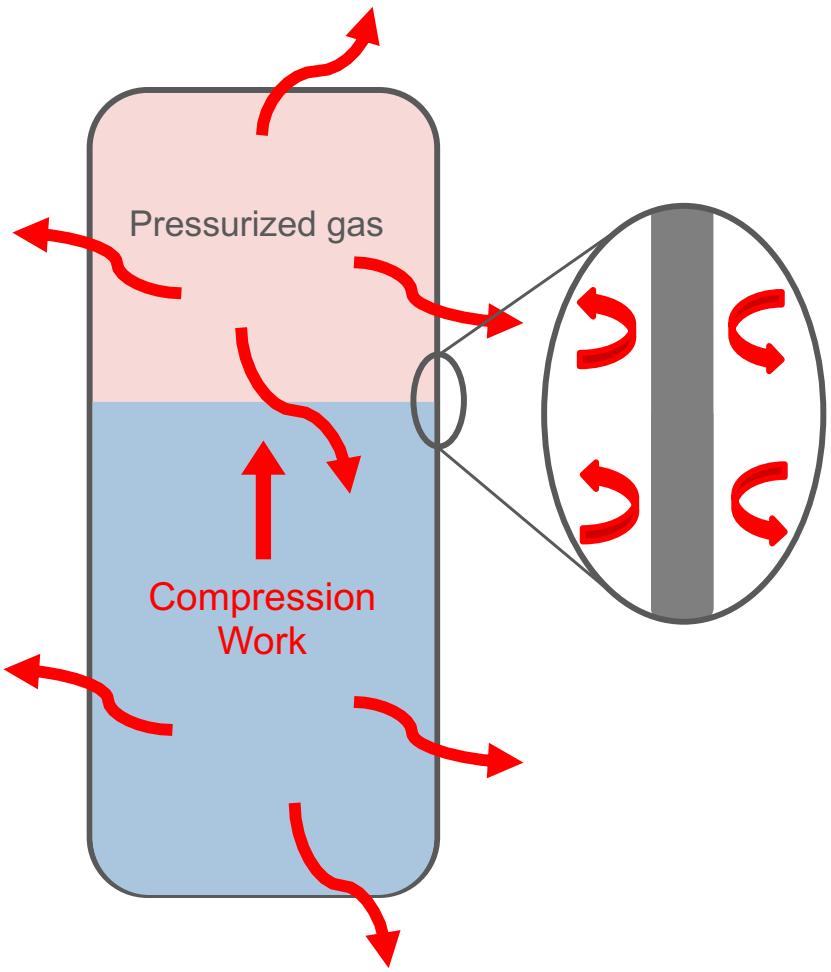

Figure 18, Heat transfer bodies and energy balance.

$$m_G c_{v,G} \frac{dT_G}{dt} = -h_{G,L} A_{G,L} (T_G - T_L) - UA_G (T_G - T_{amb}) - \dot{Q}_{spr} - P_G \frac{dV_G}{dt} \quad (3)$$

Where the overall heat transfer coefficient of air, UA_G, represents the air convection heat transfer inside the vessel, conduction heat transfer through the vessel walls, and convection heat transfer of the surrounding outside air.

$$UA_G = \frac{1}{\left(\frac{1}{h_{i,G} A_{i,G}}\right) + \left(\frac{t_T}{K_T A_{ave,G}}\right) + \left(\frac{1}{h_0 A_{0,G}}\right)} \quad (4)$$

On the other hand, $\dot{Q}_{spr}$ represents the rate of direct heat exchange from the compressed air to the sprayed droplets. To calculate this heat transfer rate, it is assumed a single droplet falls at constant velocity which can be calculated using Equation (5). Using the calculated droplet velocity, the time it takes the droplet to reach the existing water level is calculated using Equation (6). The number of droplets generated can also be calculated using the flow rate and the spray droplet diameter as shown in Equation (7). As at each time step, a certain number of droplets are generated, Equation (8) can be used to calculate the total number of droplets traveling through the air at any given instance.

$$v_{term} = \sqrt{\frac{4 D_{dr} \rho_{dr} g}{3 \rho_G C_D}} \quad (5)$$

$$t_{trav} = \frac{L(t)}{v_{term}} \quad (6)$$

$$\dot{N}_{dr} = \frac{6\dot{V}_{spr}}{\pi D_{dr}^3} \tag{7}$$

$$N_{dr} = \dot{N}_{dr} \cdot t_{trav} \tag{8}$$

Using the calculated convection heat transfer coefficient, the thermal time constant of the droplet is calculated using Equation (11).

$$Nu_{dr} = 2 + 0.6Re^{1/2}Pr^{1/3} \tag{9}$$

$$h_{dr} = \frac{Nu \cdot k_{dr}}{D_{dr}} \tag{10}$$

$$\tau_{dr} = \frac{\rho_{dr} V_{dr} c_{dr}}{h_{dr} A_{s,dr}} \tag{11}$$

As each droplet travels through the air from the top of the vessel to the existing water level (the bottom of the vessel at the beginning of the charging process), heat is transferred from the compressed air to these droplets. Equation (12) is used to calculate the temperature of the droplets right before hitting the surface of the existing water level.

$$\frac{T_{dr,out} - T_G}{T_{dr,in} - T_G} = \mathrm{e}^{-\frac{t_{trav}}{\tau_{dr}}} \tag{12}$$

Where $T_{dr,in}$ is the droplet temperature as it enters the vessel and $T_{dr,out}$ is the droplet temperature right before hitting the existing water level in the vessel. Using Equation (13), and the calculated

droplet temperature, the heat transfer from the compressed air to the water droplets is calculated and the rate of the total heat transfer from all the spray droplets is calculated using Equation (14).

$$Q_{dr} = \rho_{dr} V_{dr} c_{dr} (T_{dr,out} - T_{dr,in}) \tag{13}$$

$$\dot{Q}_{spr} = \dot{N}_{dr} \cdot Q_{dr} \tag{14}$$

To simulate the change in air pressure, Redlich-Kwong equation of state was used. As shown in Equation (15), this equation relates the pressure, temperature, and volume.

$$P = \frac{R\,T}{V_m - b} - \frac{a}{\sqrt{T}\,V_m\,(V_m + b)} \tag{15}$$

Where, P is the pressure, R is the gas constant, T is the air temperature, V_m is the molar volume, and a and b are constants calculated based on the air critical temperature and pressure as shown below.

$$a = 0.42748\,\frac{R^2 T_c^{2.5}}{P_c} \tag{16}$$

$$b = 0.08664\,\frac{R\,T_c}{P_c} \tag{17}$$

The energy balance of water in the vessel is shown using Equation (18). As seen in this equation, the time rate of change of the energy contained within the liquid (term on the left) depends on the heat transfer with air (first term on the right), with the vessel walls and the ambient (second term

on the right), and the net rate of energy transfer due to the mass flow entering the vessel (third term on the right).

$$m_L c_L \frac{dT_L}{dt} = -h_{G,L} A_{G,L} (T_G - T_L) - UA_L (T_L - T_{amb}) + \dot{m}_L c_L (T_{amb} - T_L) \tag{18}$$

Where the overall heat transfer coefficient UA_L is calculated using Equation (19) representing the water convection heat transfer inside the vessel, conduction heat transfer through the vessel walls, and convection heat transfer of the surrounding outside air.

$$UA_L = \frac{1}{\left(\frac{1}{h_{i,L} A_{i,L}}\right) + \left(\frac{t_T}{K_T A_{ave,L}}\right) + \left(\frac{1}{h_0 A_{0,L}}\right)} \tag{19}$$

As explained above, the droplet temperature leaving air and entering the existing water level was calculated using equation (12). Using this temperature, as the droplets enter the existing water, heat transfer occurs between the entering droplets and the existing water and therefore, a mixed water temperature is calculated using Equation (20).

$$T_{L,mixed} = \frac{\dot{m}_{spr}\, \Delta t\, c_{dr} T_{dr} + m_L c_L T_L}{(\dot{m}_{spr}\, \Delta t + m_L) c_L} \tag{20}$$

The other mass simulated in this model is the vessel wall, which is broken into two sections, the top part in contact with the air and the bottom part in contact with the rising water. Equations (21) and (22) are used to simulate the rate of energy contained within the corresponding mass in contact with air and water respectively.

$$m_{T,G} c_T \frac{dT_{T,G}}{dt} = h_{i,G} A_{i,G} \left(T_G - T_{T,G}\right) - h_0 A_{0,G} \left(T_{T,G} - T_{amb}\right) \quad (21)$$

$$m_{T,L} c_T \frac{dT_{T,L}}{dt} = h_{i,L} A_{i,L} \left(T_L - T_{T,L}\right) - h_0 A_{0,L} \left(T_{T,L} - T_{amb}\right) \quad (22)$$

4.1 Simulation Results

The experimental data gathered were used to validate the developed simulation model. To validate the model, vessel volume 287 liter, 19 kg of air, 21.3℃ initial air temperature, 55 bar initial air pressure, 1177 rpm motor speed, 97 bar maximum pressure, and 1.5 and 1.4 hours of pause time for the first and second pause respectively were given to the model as the inputs. Figure 19 and Figure 20 show the data comparison on the P-V diagram and temperature profile vs time respectively. Data in Figure 19 show almost exact match other than volume at the end of the compression process which is lower than the volume recorded in the experimental data. Also, it can be seen in Figure 20 the air temperature increase during the compression process is lower than what is recorded in the experimental data. It should be mentioned the discharge process was stopped before all water was discharged from the vessel due to safety issues and should be neglected in this study.

As explained before, the main force preventing increase in gas temperature during the compression process using the 2nd configuration is the direct heat exchange of the droplets with air. As seen in Figure 20, the increase in gas temperature during the compression process is lower than the experimental data gathered. Analyzing the data, it was concluded the simulation model accounts for 100% of the air volume being sprayed on and not account for air volume not being sprayed on. To account for the nozzle angle, some geometry equations were added to the simulation model.

Based on the spray angle and the vessel height, maximum diameter of the sprayer cone is calculated. If maximum diameter is higher than the vessel diameter, the height at which the vessel diameter is reached is calculated and using this height, cone volume is calculated. If the cone diameter is less than the vessel diameter, cone volume is calculated and gas volume is calculated based on the cone volume. Volume not sprayed is calculated by subtracting sprayed gas volume from the total gas volume. Based on the data provided by the nozzle manufacturer for the full cone nozzle used on the GLIDES 2nd generation prototype, depending on the pressure, spray angle can vary between 45 to 85 degrees. As shown in Figure 19, the air volume matches perfectly and as seen in Figure 20 as seen in the compression process, at the beginning of the process, the air temperature increases around 3℃ during the first 2 minutes. This makes sense as temperature difference is needed to have any heat transfer. Hence the air temperature increases at first. The air temperature reaches the maximum temperature by the end of the charging process. The pressure profile vs time is also shown in Figure 23.

Using the simulation model, the change in flow rate at various initial pressures vs. time are shown in Figure 24. It is seen as the air pressure increases, the flow rate decreases around 1 l/min. Figure 25 and Figure 26 show the change in flow rate and change in indicated power (product of pressure and flow rate) during an isothermal and adiabatic process along the experimental data vs. time respectively.

Based on the experimental data and the simulation analysis, it is therefore determined using spray compression during charging of the GLIDES 2nd prototype, isothermal compression efficiencies as high as 98.5% are achievable. GLIDES capital cost depends on various parameters including the thermodynamic efficiency. To study the capital cost of the GLIDES system, a technoeconomic model was developed and is discussed in the next chapter.

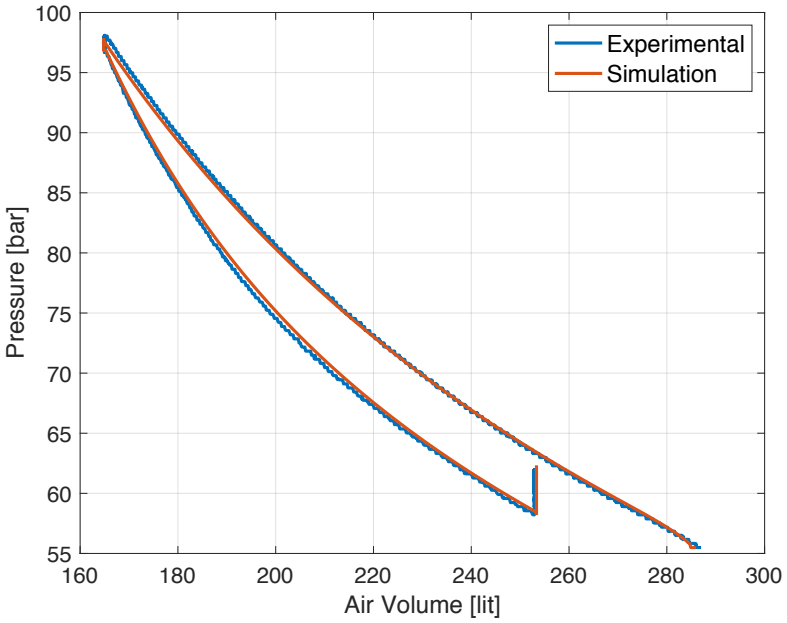

Figure 19, P-V diagram experimental vs. simulation data.

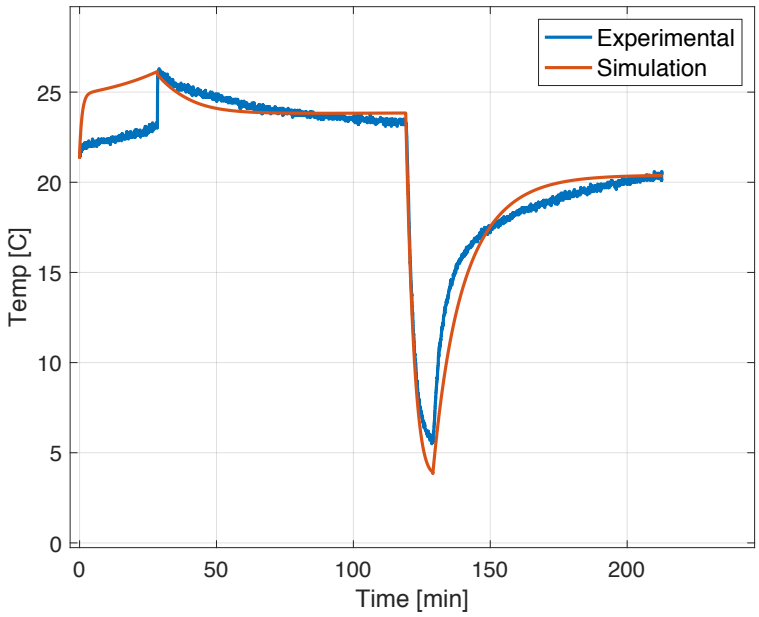

Figure 20, Temperature vs. time experimental vs. simulation data.

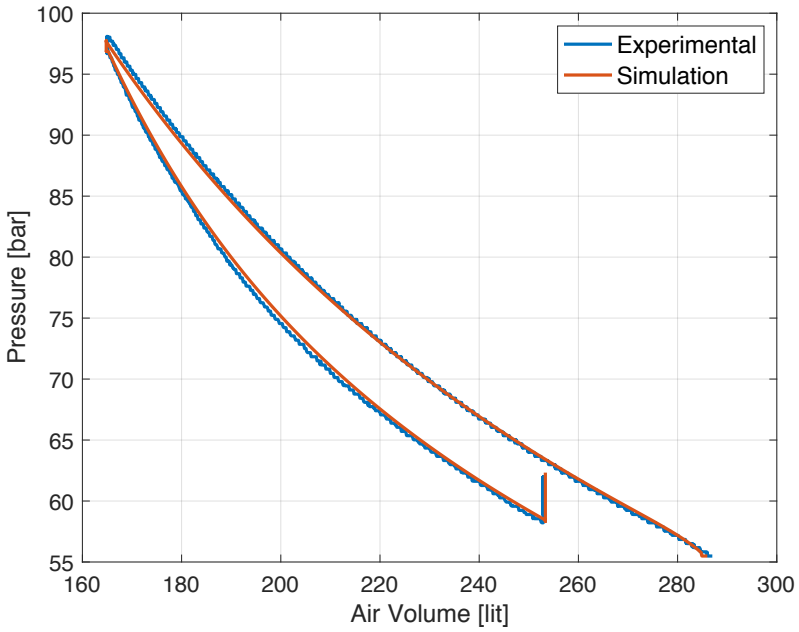

Figure 21, P-V diagram experimental vs. simulation data.

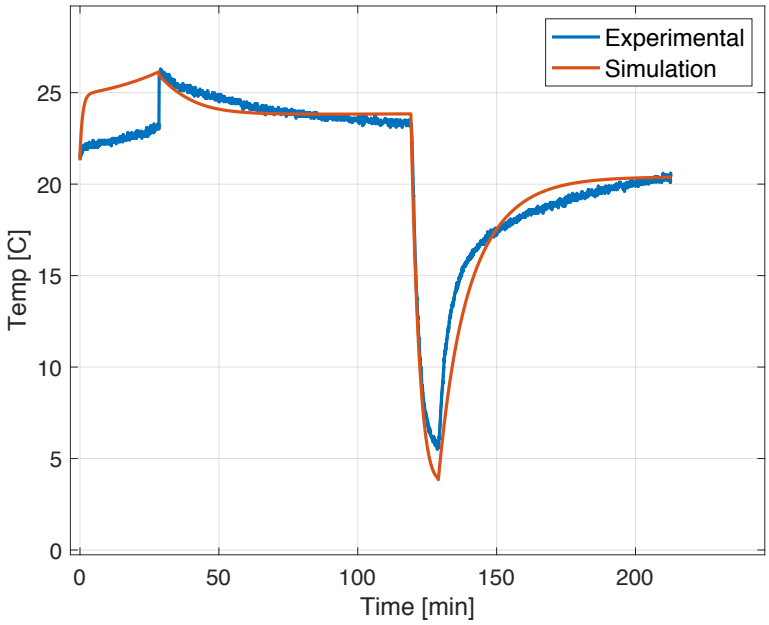

Figure 22, Temperature vs. time experimental vs. simulation data.

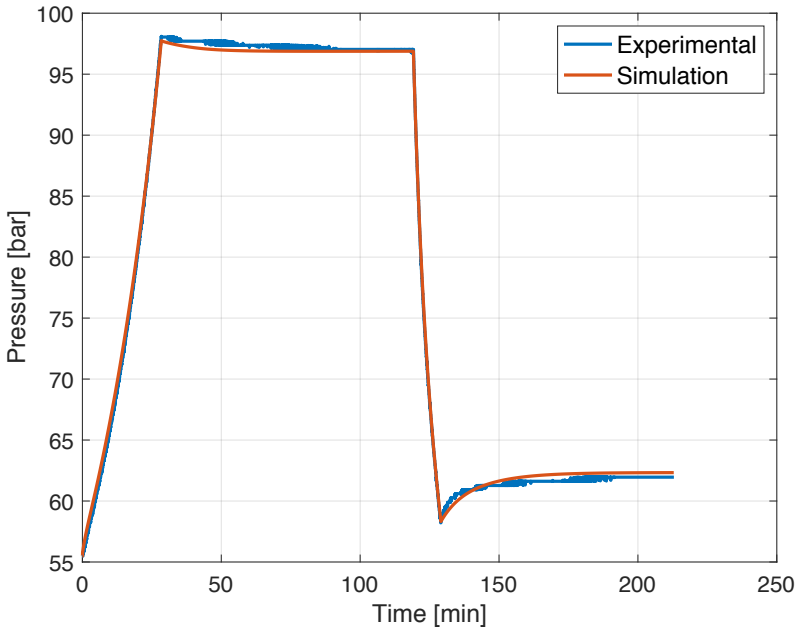

Figure 23, Pressure vs. time.

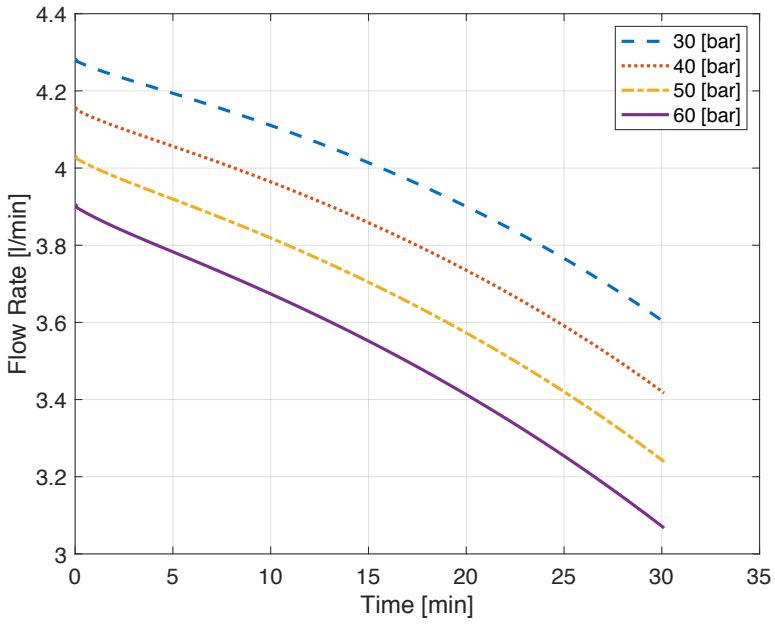

Figure 24, Flow rate profile during the charging process vs. time.

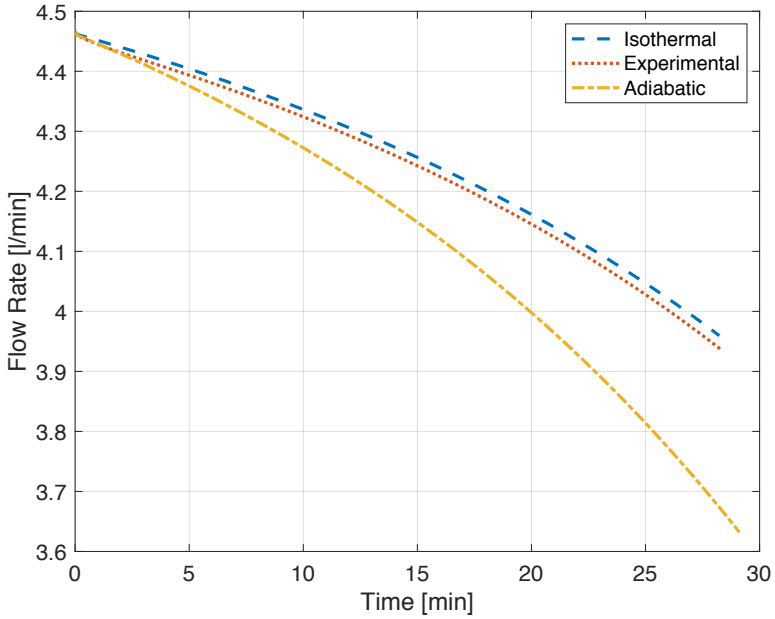

Figure 25, Change in flow rate during isothermal and adiabatic compression along the experimental data vs. time.

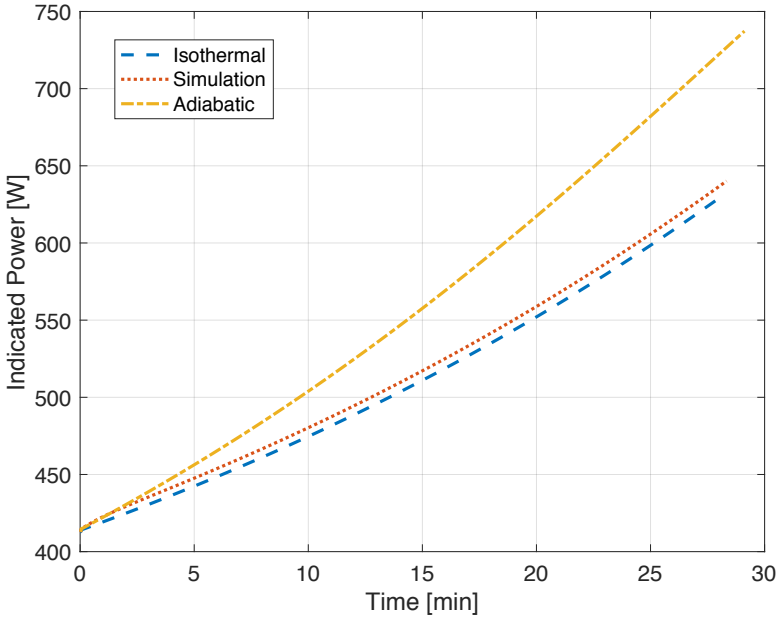

Figure 26, Change in indicated power during an isothermal and adiabatic compression along the experimental data vs. time.

Chapter 5: Waste Heat Integration

As explained in previous chapters, increase in gas temperature during the compression process and decrease in gas temperature during the discharge process decrease the GLIDES efficiency. To decrease the efficiency losses due to gas expansion, spray heating is proposed to prevent air temperature from decreasing and achieving near isothermal expansion. To simulate the effect of spray heating during the discharge process, the physics-based performance model was updated to include the spray heating during the discharge process. The simulation data along experimental analysis of the GLIDES 3rd configuration is discussed in this chapter.

5.1 GLIDES 3rd Configuration

As shown in Figure 14, during the discharge process, as the high-head water is discharged through the hydraulic turbine, air expands causing the pressure and temperature to drop rapidly. Air temperature drops to temperatures as low as 5℃ which is due to the expansion work and the low heat transfer between air and the surrounding and is the cause of the losses during the discharge process. Increasing the expansion efficiency improves the cycle efficiency providing higher output power. An option to increase the expansion efficiency is to employ spray heating during the discharge process. As air temperature in the vessel reaches temperatures as low as 5 ℃, spraying water with temperatures of around 21℃ would provide direct heat exchange between air and the water droplets decreasing the change in air temperature and achieving near-isothermal expansion. As explained before and shown in Figure 4, GLIDES 3rd configuration includes a second-loop capable of pumping water from the bottom of the vessel to the top using a secondary pump and sprayed into the vessel while water is being discharged through the hydraulic turbine. To farther increase the expansion efficiency, low-grade waste heat can be employed to increase the water

temperature being sprayed into the vessel farther increasing the air temperature. Odukomaiya et al. showed results of studies done on a simulation model on system performance employing isothermal compression (spray cooling) and spray heating including the following processes: 1) an isothermal expansion after the pause process, 2) isochoric heat input during the pause process after compression is over and isentropic expansion, and 3) isochoric heat input during the pause process after the compression is over and isothermal expansion and isochoric heat out during the pause time after the discharge process [31].

5.2 Simulation Model

To simulate the system behavior during the discharge process, the discharge section of the simulation model is formed. The discharge simulation continues while water volume exists in the vessel simulating heat transfer between air and water surface in the vessel, air and the vessel walls, and air and the droplets. Various flow rates ranging from 1-10 LPM were studied using the simulation model to select the secondary pump providing the best heat transfer. As seen in Figure 28, with increasing second pump flow rate from 0 to 10 LPM, the change in discharge temperature decreases from around 22℃ to around 2℃. As explained before, the area between the charging and discharging curves on a P-V diagram represent the losses both due to losses in compression and expansion process. Figure 29 shows the decrease in the losses with increasing the second pump flow rate going from the blue line with no spray to the red line with 10 LPM flow rate, increasing the overall indicated efficiency.

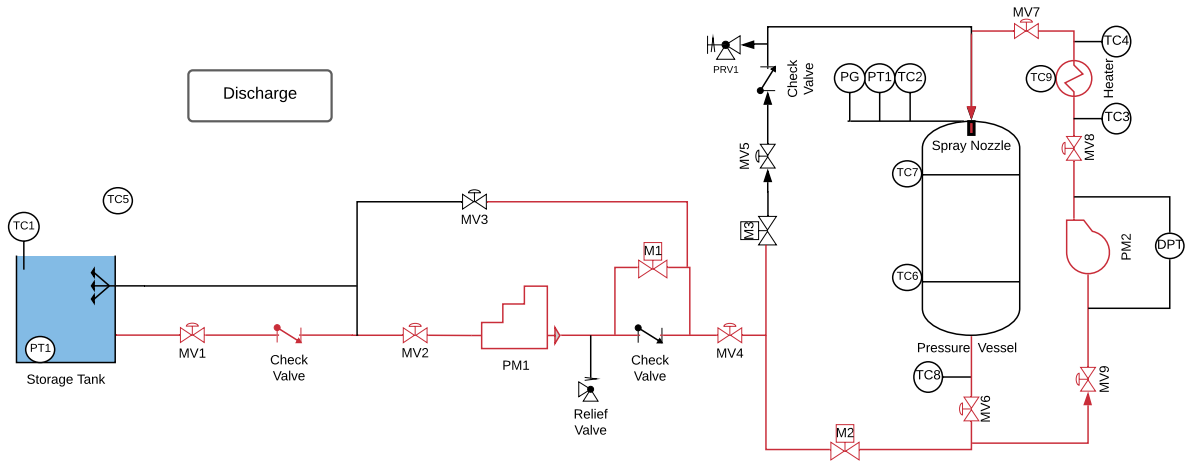

Figure 27, GLIDES 2nd prototype P&ID, discharge using spray heating.

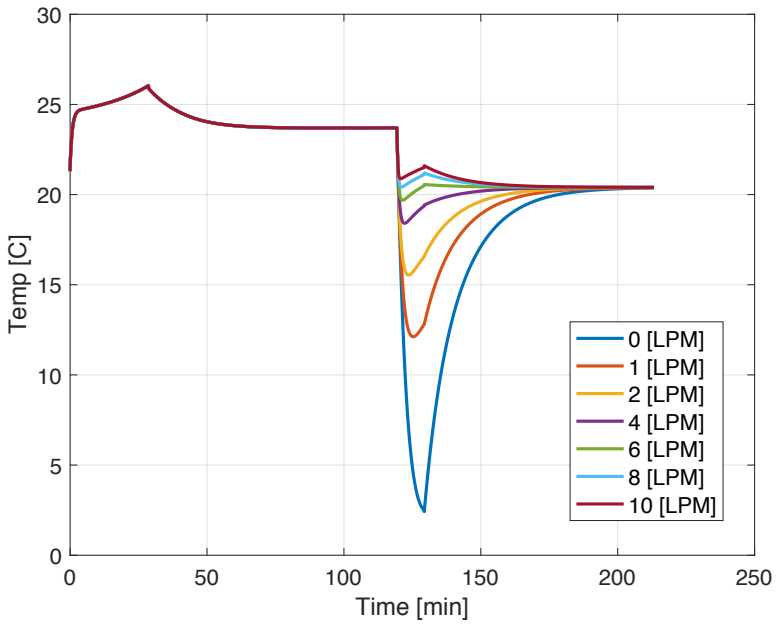

Figure 28, Air temperature profile with various second pump flow rates.

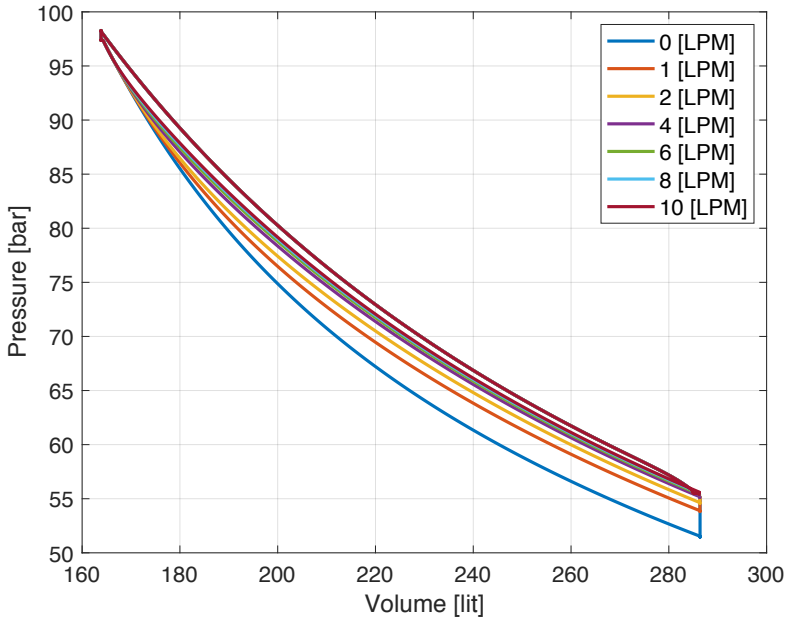

Figure 29, P-V diagram with various second pump flow rate.

To achieve the other cycles mentioned above, higher droplet temperatures are required. This can be achieved by employing waste heat to increase the droplet temperatures before spraying into the vessel. These cycles can include heating the air temperature during the pause time before discharge begins which still requires heat addition during the discharge process to achieve a near isothermal expansion or adding heat only during the discharge process. If heat is added during the pause process, less heat would be required to achieve a near isothermal expansion. Another way would be to add heat during both pause and the discharge process and either store the excess heat after the discharge or dissipate to the ambient. Using excess heat can have the benefit of using a lower flow rate second pump. To show the change in data by adding heat during the discharge process employing 8 LPM secondary pump, Figure 30 was developed. It can be seen during the discharge process, if droplet temperature is less than that of air temperature at the end of the pause process, air temperature experiences a U-shaped temperature profile during which temperature decreases initially and then increases.

Figure 32 through Figure 34 were plotted to show how the cycle changes by employing spray heating during both pause and discharge process assuming heat addition to increase the water temperature before spraying to 25℃, 30℃, and 35℃.

5.3 Experimental Data

To perform experiments on GLIDES employing spray heating, an 8 LPM positive displacement pump was installed. GLIDES vessel was pressurized with air to initial pressure of 32 bar. Using spray charging, GLIDES was charged to maximum pressure of 89 bar. The second pump was turned on right before the discharge process. While discharging, a Variac was used to keep the speed at around 1000 RPM.

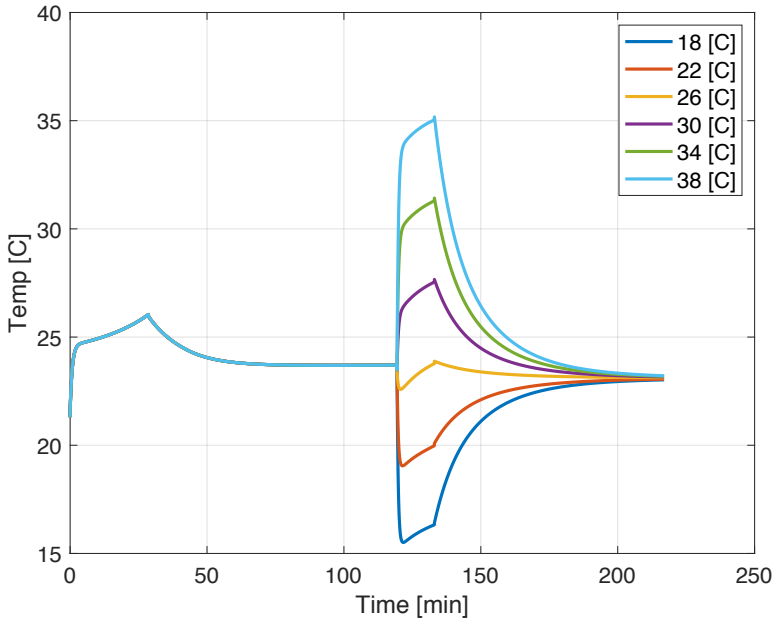

Figure 30, Temperature profile using various temperature droplets during the discharge process.

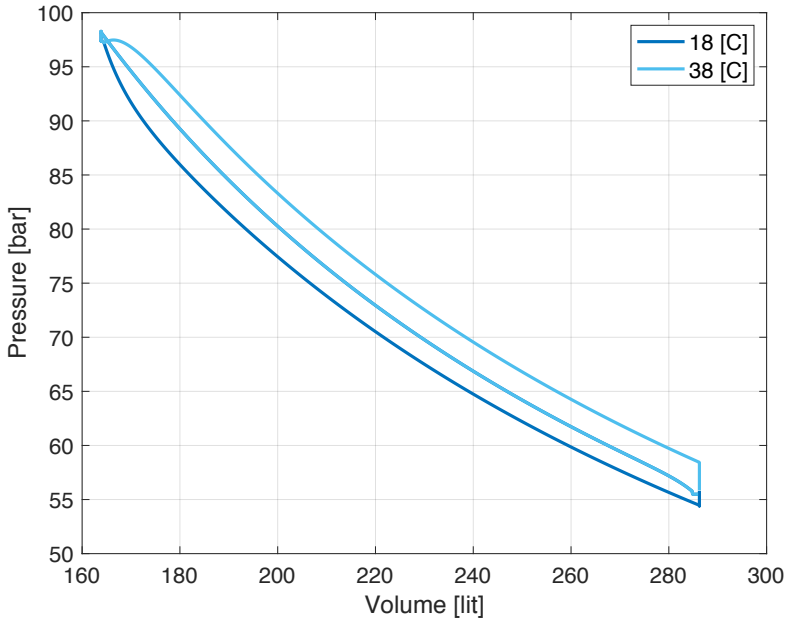

Figure 31, P-V diagram showing the difference between spraying with low- and high-temperature droplets.

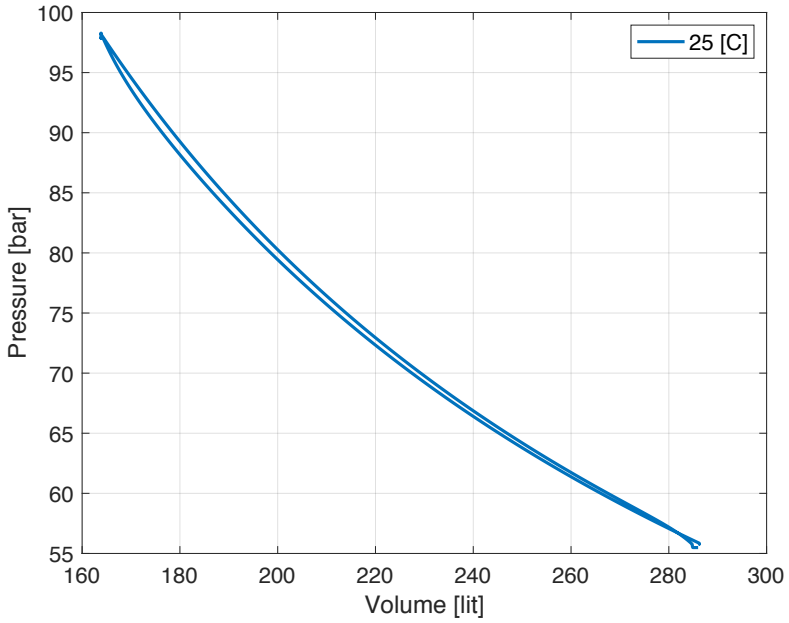

Figure 32, P-V using 25C spray during both pause and discharge process.

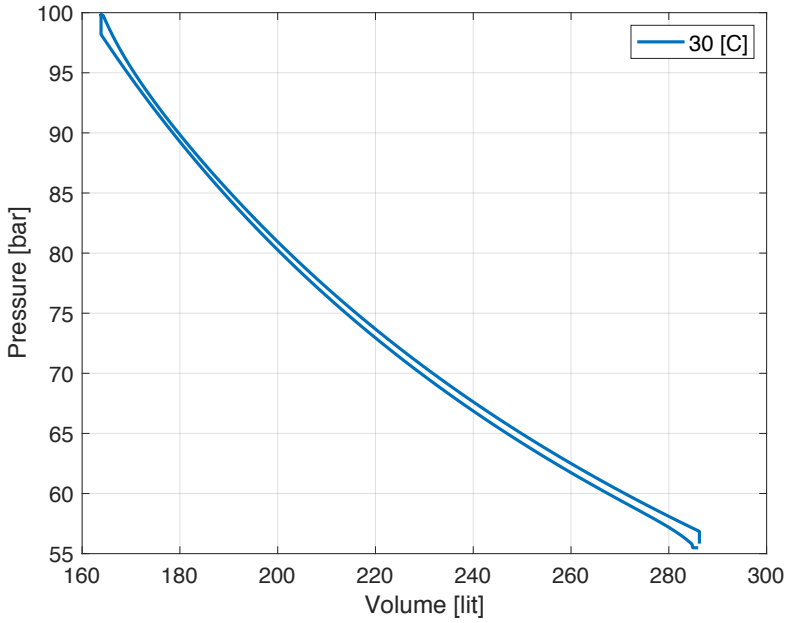

Figure 33, P-V diagram using 30 C spray during both pause and discharge.

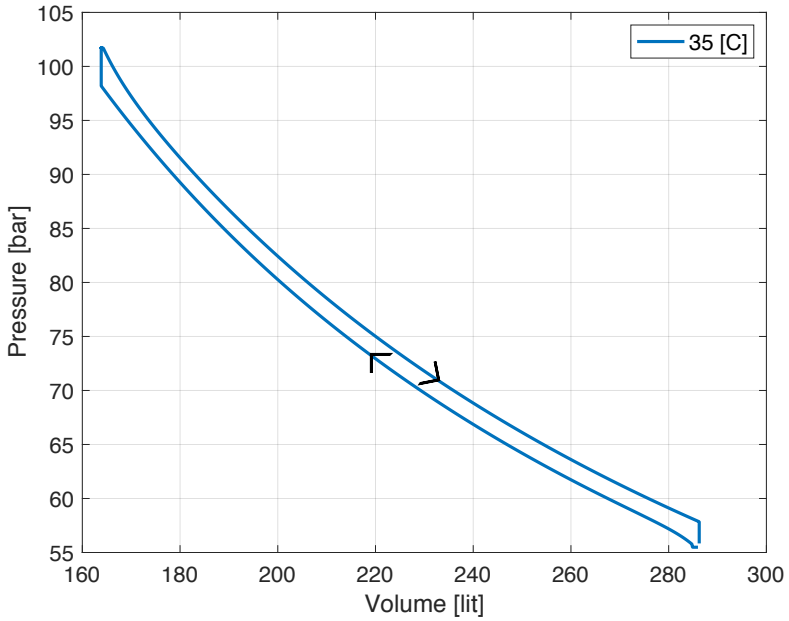

Figure 34, P-V diagram using 35C spray heating during both pause and discharge process.

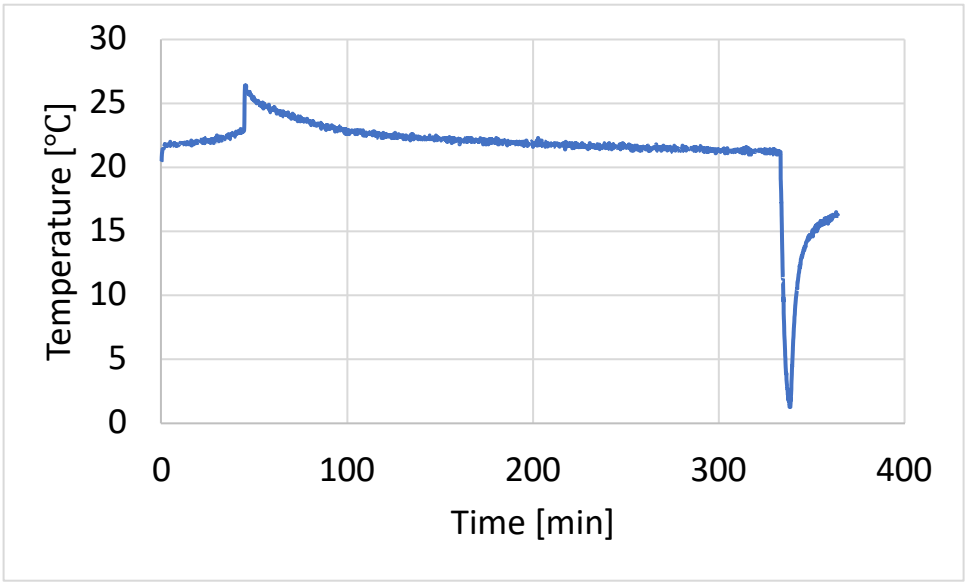

Figure 35, Temperature profile during discharge vs time.

Figure 35 shows the air temperature profile vs time during the discharge process. As seen in this figure below, air temperature dropped to temperatures as low as 1.2℃ and therefore the experiment was stopped to prevent ice forming in the vessel and prevent equipment malfunction. It should be noted the minimum air temperature without employing the second pump was around 5℃.

The P-V diagram of this process is shown in Figure 36. To study the effect of using the second pump during discharge, the data collected during this experiment were compared to another experiment without employing the second pump. One way to compare the two experiments is to compare the polytropic coefficients during the expansion process. To do so, although the initial volume was not exactly similar, natural log of the pressure was plotted vs natural log of the volume for both experiments with and without spray heating. As seen in Figure 37, the polytropic coefficient of the process with spray heating is around 1.07 and the process without spray heating is around 1.33, which for an isothermal process n=1 and n=1.4 for an adiabatic process. Although this plot/calculation propose an isothermal expansion for the experiment using spray heating, as the temperature dropped to very low temperatures, other calculations must be performed before conclusions are made. The drop in temperature can be due to evaporation in the vessel and as explained before the data is partially affected by the spray droplets coming in contact with the thermocouple.

As air is an ideal gas, Equation (23) can be employed to solve for the polytropic coefficient n using pressure and temperature. This was done as both pressure and temperature are data collected during the experiment and volume was calculated based on the motor speed and the water flow rate entering the water reservoir.

$$\frac{T_2}{T_1} = \left(\frac{P_2}{P_1}\right)^{(n-1)/n} = \left(\frac{V_1}{V_2}\right)^{n-1} \tag{23}$$

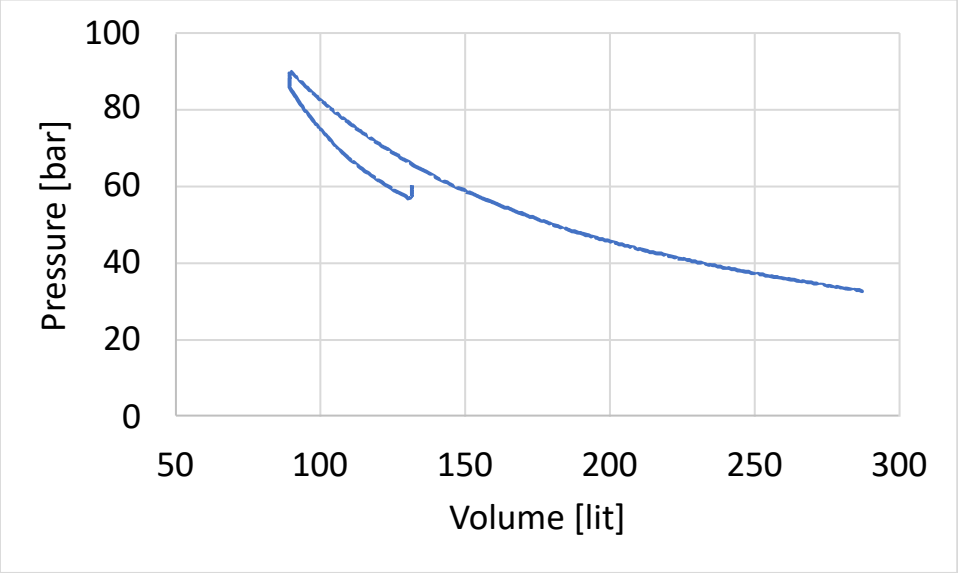

Figure 36, P-V diagram of the entire cycle employing second pump.

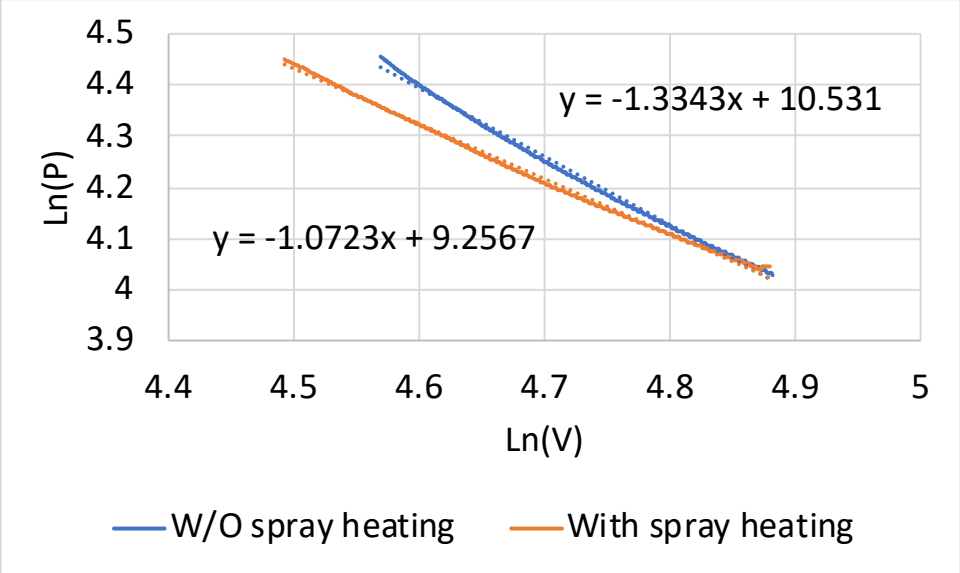

Figure 37, Ln(P) vs Ln(V).

Using pressure and temperature in Equation (23), $n = 1.12$ and $n = 1.17$ were calculated for the experiment without spray heating and with spray heating respectively making these processes almost identical. Based on the calculations done, it is concluded the second pump either malfunctioned and failed to pump the desired flow rate against the high pressure air inside the vessel or isothermal expansion was achieved, but due to evaporation lower temperatures were recorded.

After the experiment was stopped, an electric resistance heater wrapped around the secondary loop piping was turned on and off maintaining a pipe surface temperature of around 45℃ (and not higher to prevent issues with the pipes and couplings) to increase the water temperature inside the vessel as second pump was running to circulate the water. As the heater power is low (~1kW), it would take hours to heat up the water in the vessel. To achieve the cycles mentioned above experimentally, other methods to increase water temperature are required to perform the experiments.

Chapter 6: Isothermal Liquid Compressor (IsoLiqComp)

The overall goal of the project is to prototype and characterize the performance of liquid-piston spray-cooled gas compressor. The working principle of the compressor enables optimized high-efficiency operation over very wide range of operating conditions, unlike conventional compressors that are optimized for a narrow range of operating conditions. The compressor is suitable for wide range of applications, such as gas pipeline transport and gas storage. The project aims to demonstrate the performance of the compressor in heat pump application.

As explained in previous sections, in traditional gas compressors, as the gas is compressed using mechanical pistons, one of the limiting factors is the temperature increase during the compression process. This limiting factor and other losses associated in traditional compressors can be avoided by leveraging two recent studies that facilitate advanced gas/refrigerant compression using liquid-piston compression and advanced heat exchange via micron-sized sprayed droplets and achieving a third innovation, large-bore, flexible stroke compressor. Successfully combining these three studies could enable a step change reduction in refrigerant compression energy consumption and achieving (near) isothermal compression. The proposed technology will provide adjustable compression ratio capabilities which make one compressor compatible with all refrigerants and applications. The designed systems are capable of simulating both CO_2/oil and air/water combinations as the working fluids. A second physics-based performance model was developed to simulate the CO_2 compression including condensation, making IsoLiqComp capable of compressing to high-pressure gas or compressing beyond condensation conditions to employ in applications which can benefit from liquid CO_2.

6.1 The Proposed Compressor

Employing spray cooling and liquid piston, it is proposed to design a near-isothermal efficient gas compressor compatible with all refrigerants and applications called Isothermal Liquid Compressor (IsoLiqComp). As seen in figure 2, IsoLiqComp has 4 main processes during which the entire cycle takes place including the low-pressure gas intake stroke, compression stroke, delivery stoke, and the expansion stroke. During the first step, the valve controlling the low-pressure gas flow is opened while all other valves remain closed, and the compression vessel is filled with gas. During the second step, after the vessel is entirely filled with gas, the gas flow is stopped, and the compression process takes place by pumping oil to the top of the vessel and spraying the oil from the top into the vessel causing a near-isothermal compression as the oil level rises. This process is continued until the gas pressure is increased to the set pressure of the regulator valve (no oil or gas exit the vessel during this process). The regulator valve is opened once the gas pressure reaches the discharge pressure in step 3. Oil is continuously sprayed until no gas is left in the vessel. In step 4, the gas flow and the oil discharge valves are opened. Oil is discharged back to the reservoir due to the pressure of the entering gas and the head of the oil in the vessel and the vessel is charged with low-pressure gas returning to step 1. As the temperature of oil has increased during the compression process, this heat is recovered using a heat exchanger as oil is discharged back to the reservoir returning to the initial temperature.

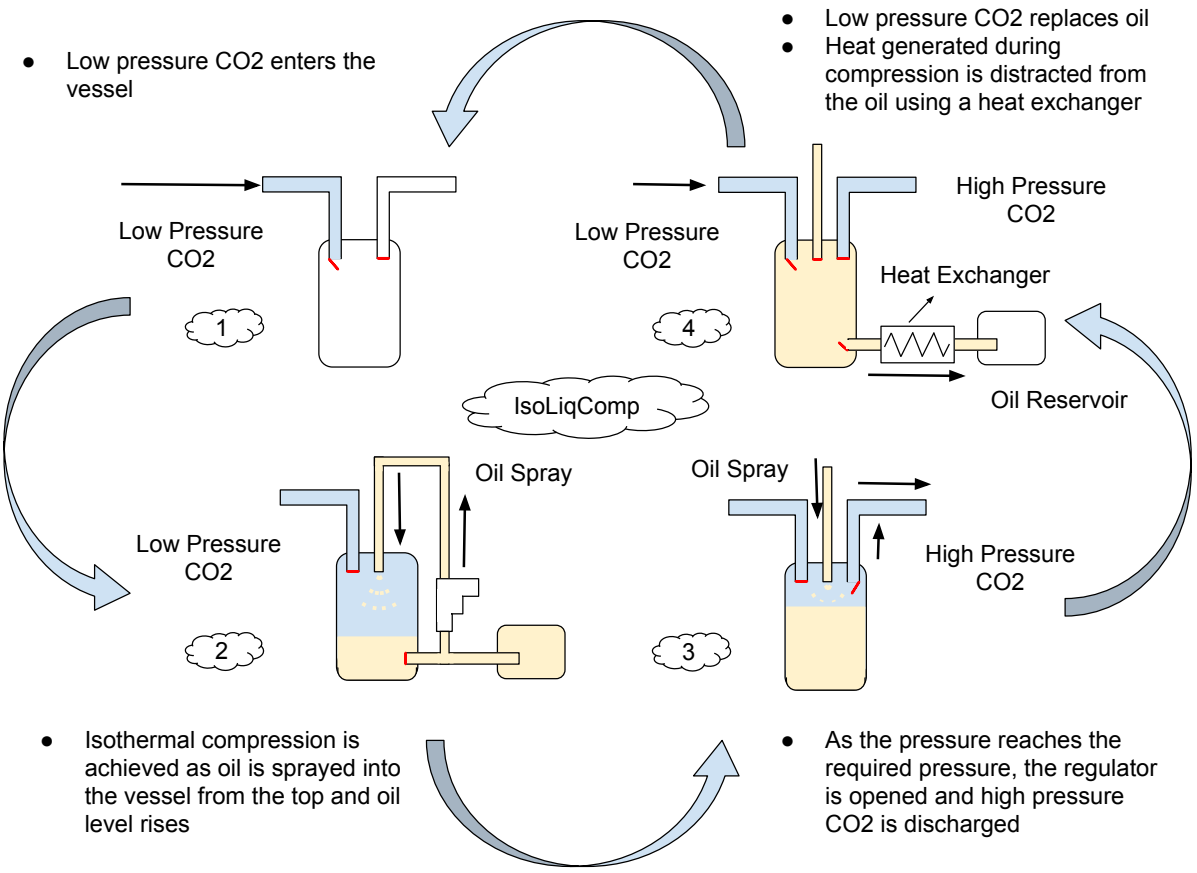

Figure 38, IsoLiqComp cycle design.

6.2 Physics-Based Performance Model

Since the start of this project, multiple physics-based performance models have been developed and reported simulating the system behavior. In the first model developed, only gas compression without considering any condensation was reported. To account for condensation, a second model was developed simulating gas compression and condensation. To simulate these conditions, many constraints were introduced including temperature, pressure, and vapor volume, limiting each loop. To make these conditions and the model more realistic and to include superheated fluid conditions, a third physics-based performance model has been developed. The new model aims to simulate all conditions during CO_2 compression including vapor compression, condensation, liquid compression, and supercritical conditions. As reported in literature, CO_2 behavior under various conditions is shown on two main diagrams: the CO_2 phase diagram and the pressure-enthalpy (P-H) diagram shown in Figure 39 and Figure 40 respectively. As seen in Figure 39, while pressure is less than the CO_2 critical pressure (72.9 bar), CO_2 can be found in vapor or liquid conditions depending on the temperature and when pressure rises above the critical point, supercritical fluid forms. On this diagram it can also be seen that when pressure is less than the critical pressure, but above the saturation pressure, and temperature is lower than the critical temperature, condensation takes place. Another way of showing these conditions, is to use a P-H diagram. As shown in Figure 40, the red star at the peak of the dome marks the critical pressure (73.9 bar) below which, both vapor and liquid conditions can be present depending on the temperature.

The most useful parameter on this diagram (Figure 40) is enthalpy. As explained before, we used temperature, pressure, and vapor volume to track the conditions in previous models. Using a P-H diagram, this can be done with much higher accuracy by employing enthalpy. As seen in Figure 40, below the critical pressure, three modes can be present depending on the temperature (each

blue line represents a constant temperature line) and enthalpy including superheated vapor region on the right side of the dome, saturated mixture (vapor and liquid mixture) within the dome and compressed liquid region on the left side of the dome. On the other hand, for pressures above the critical pressure, the supercritical region is specified. To employ this knowledge in our new physics-based model, as shown in Figure 41, the model was broken into 7 sections. Unlike previous models, only one while-loop was employed in this model which is to run the simulation while the overall pressure is less than the maximum set pressure (140 bar in this study). Within this while-loop, if-statements were employed to specify the CO_2 condition and to therefore use the right equations (see Figure 41).

While the pressure is lower than the maximum pressure, the model checks to see if the pressure is less than the critical pressure. If so, the model checks to see if the enthalpy at that temperature and pressure is less than the saturation vapor enthalpy (the enthalpy value corresponding to the saturation vapor line of the dome, right of the critical pressure). If the enthalpy is not less than the saturation vapor enthalpy, vapor compression using spray cooling mechanism takes place (to the right of the dome). If enthalpy is less than the saturation vapor enthalpy, the model checks to see if enthalpy is less than the saturation liquid enthalpy (the enthalpy value corresponding to the saturation liquid line on the dome, left of the critical pressure). If enthalpy is not less than the saturation liquid enthalpy, condensation takes place (within the dome where enthalpy is less than the saturation vapor enthalpy and higher than saturation liquid enthalpy). If enthalpy is less than the saturation liquid enthalpy (left of the dome), liquid compression takes place. On the other hand, if pressure is not less than the critical pressure, supercritical fluid exists, and supercritical compression takes place (above the dome). Since only one while-loop is used, each iteration starts from the top and checks all these statements.

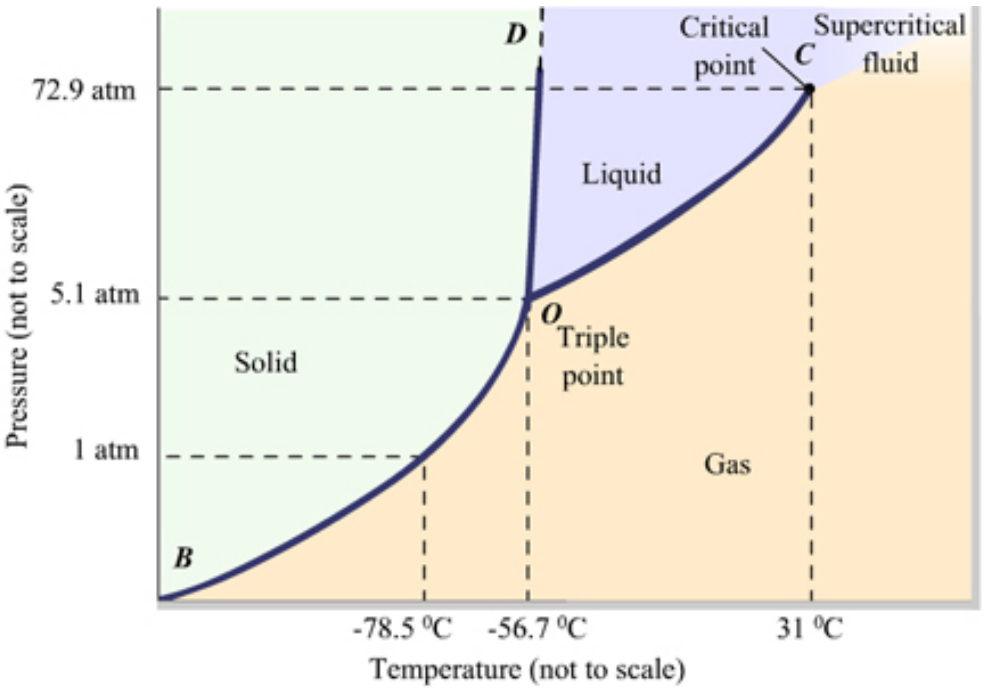

Figure 39, CO_2 phase diagram.

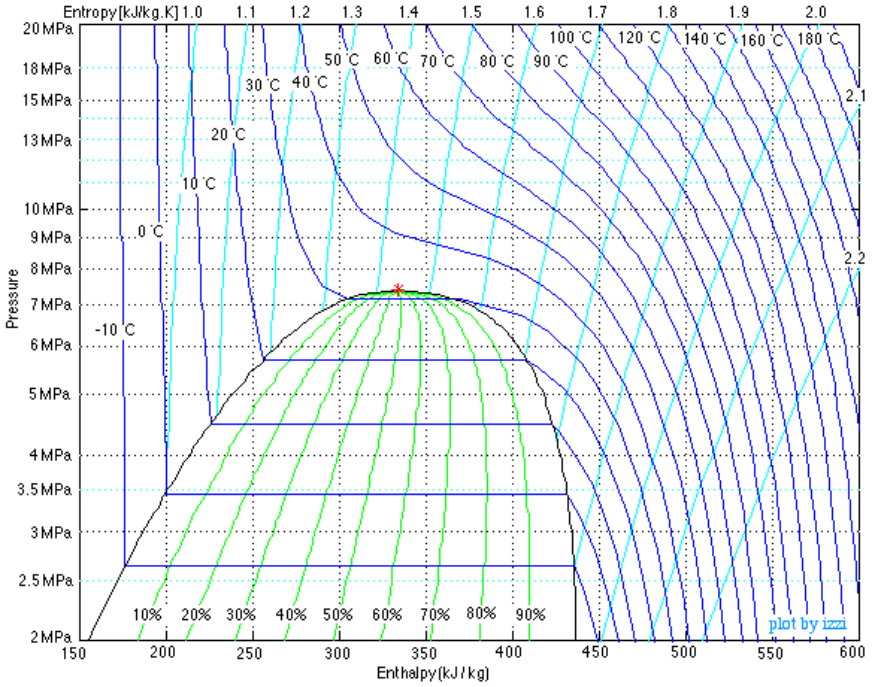

Figure 40, CO_2 pressure-enthalpy, P-H diagram.

Therefore, if pressure is less than the critical pressure, enthalpy is higher than saturation vapor enthalpy, compression occurs. If the enthalpy decreases to the saturation vapor enthalpy, condensation takes place at constant temperature and pressure until enthalpy decreases to the saturation liquid enthalpy, after which only liquid exists in the compression chamber. Liquid compression takes place until pressure reaches the critical pressure and after that, supercritical fluid compression continues until the maximum pressure is reached. Specific equations used during each statement are reported in the next section.

6.2.1 Equations

Most of the equations used to develop the new model including heat transfer due to employing spray cooling in Chapter 4: and are included here as well. To simulate the temperature and pressure change during the compression process, the spray droplet calculations below are used to calculate the number of droplets (Equation (25)), the temperature of droplet after travelling from the top of the compression chamber to the existing oil level (Equation (26)), the heat transfer rate due to direct heat exchange between the droplets and the CO_2 (Equation (29)), and the updated oil temperature after each droplet enters the existing oil volume (Equation (30)).

$$\dot{N}_{dr} = \frac{6\dot{V}_{spr}}{\pi D_{dr}^3} \tag{24}$$

$$N_{dr} = \dot{N}_{dr} \cdot t_{travel} \tag{25}$$

$$\frac{T_{dr,out} - T_V}{T_{dr,in} - T_V} = e^{-\frac{t_{travel}}{\tau_{dr}}} \tag{26}$$

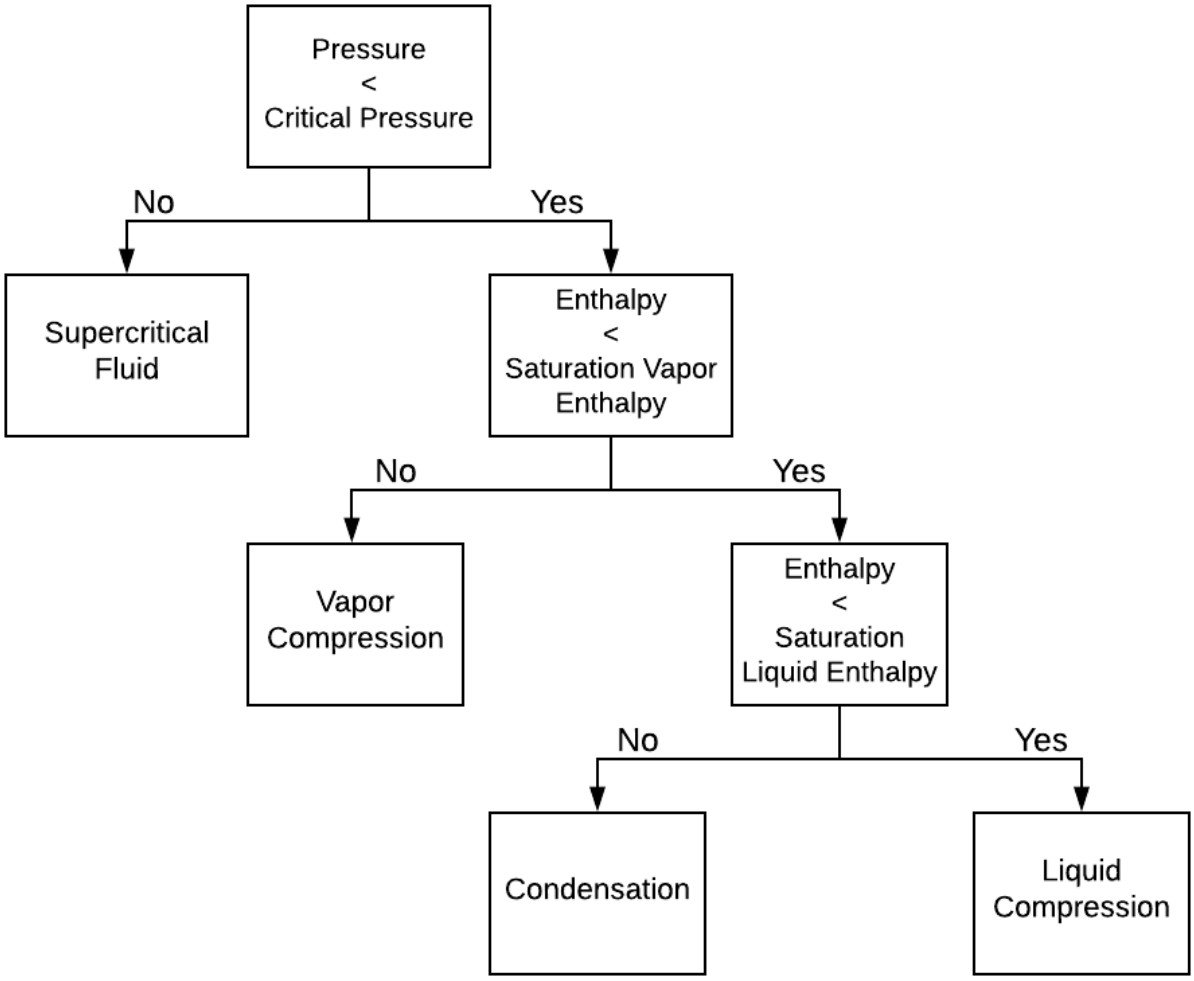

Figure 41, Model-3 flow diagram.

$$\tau_{dr} = \frac{\rho_{dr} V_{dr} c_{dr}}{h_{dr} A_{s,dr}} \tag{27}$$

$$Q_{dr} = \rho_{dr} V_{dr} c_{dr} (T_{dr,out} - T_{dr,in}) \tag{28}$$

$$\dot{Q}_{spr} = \dot{N}_{dr} \cdot Q_{dr} \tag{29}$$

$$T_{O,mixed} = \frac{\dot{m}_{spr} \Delta t c_{dr} T_{dr} + m_O c_O T_O}{(\dot{m}_{spr} \Delta t + m_O) c_O} \tag{30}$$

The following equations represent the overall heat transfer coefficients of vapor and oil (Equations (31) and (32)), energy equations used to calculate the vapor and oil temperature (Equations (33) and (34)), and Redlich-Kwong equation of state to calculate the vapor pressure while only vapor exists (Equations (35)-(37)).

$$UA_V = \frac{1}{\left(\frac{1}{h_{i,V}}\right) + \left(\frac{t_T}{k_T A_{ave,V}}\right) + \left(\frac{1}{h_o A_{o,V}}\right)} \tag{31}$$

$$UA_O = \frac{1}{\left(\frac{1}{h_{i,O} A_{i,O}}\right) + \left(\frac{t_T}{k_T A_{ave,O}}\right) + \left(\frac{1}{h_o A_{o,O}}\right)} \tag{32}$$

$$m_V \, C_V \, \frac{dT_V}{dt} = -h_{V,O} \, A_{V,O} \, (T_V - T_O) - UA_V (T_V - T_{amb}) - \dot{Q}_{spr} + P_V \, \frac{dV_V}{dt} \tag{33}$$

$$m_O\ C_O\ \frac{dT_O}{dt} = h_{V,O}\ A_{V,O}\ (T_V - T_O) - UA_V(T_O - T_{amb}) + \dot{m}_O c_O(T_{O,mix} - T_O) \tag{34}$$

$$P = \frac{R\ T}{V_m - b} - \frac{a}{\sqrt{T}\ V_m\ (V_m + b)} \tag{35}$$

$$a = 0.42748\ \frac{R^2\ T_c^{2.5}}{P_c} \tag{36}$$

$$b = 0.08664\ \frac{R\ T_c}{P_c} \tag{37}$$

While condensation is in process, temperature and pressure are assumed to be constant and the densities are found using CoolProp from the calculated temperature and pressure. Using the calculated densities, the vapor quality is calculated using (Equation (38)). During condensation, vapor mass is calculated based on (X * total mass) and liquid mass is updated accordingly.

$$X = \frac{\frac{1}{\rho_{average}} - \frac{1}{\rho_{liquid}}}{\frac{1}{\rho_{vapor}} - \frac{1}{\rho_{liquid}}} \tag{38}$$

$$X = \frac{m_{vapor}}{m_{total}} \tag{39}$$

After condensation is over, the below equations were used to simulate liquid conditions by first calculating the liquid density (Equation (40)) based on the liquid mass (which is equal to the initial vapor mass after condensation is over) and volume.

$$\rho_{liquid} = \frac{mass_{liquid}}{V_{liquid}} \tag{40}$$

Using this updated density, the overall heat transfer coefficient (Equation (41)), and the energy equation for liquid CO_2 (Equation (42)), the liquid temperature is calculated. Using the calculated liquid density and temperature, the liquid pressure is calculated using CoolProp [36].

$$UA_L = \frac{1}{\left(\frac{1}{h_{i,L}}\right) + \left(\frac{t_T}{k_T A_{ave,L}}\right) + \left(\frac{1}{h_o A_{o,L}}\right)} \tag{41}$$

$$m_V\, C_L\, \frac{dT_L}{dt} = -h_{L,O}\, A_{L,O}\, (T_L - T_O) - UA_L(T_L - T_{amb}) - \dot{Q}_{spr} + P_L\, \frac{dV_L}{dt} \tag{42}$$

As pressure rises above the critical pressure (supercritical), the density is calculated using the supercritical fluid mass and volume (mass/volume). Using the below overall heat transfer coefficient (Equation (43)) and the energy equation (Equation (44)), supercritical temperature is calculated. Supercritical pressure is therefore calculated using the temperature and density in CoolProp.

$$UA_F = \frac{1}{\left(\frac{1}{h_{i,F}}\right) + \left(\frac{t_T}{k_T A_{ave,F}}\right) + \left(\frac{1}{h_F A_{o,F}}\right)} \tag{43}$$

$$m_V \, C_F \, \frac{dT_L}{dt} = -h_{F,O} \, A_{F,O} \, (T_F - T_O) - UA_F(T_F - T_{amb}) - \dot{Q}_{spr} + P_F \, \frac{dV_F}{dt} \tag{44}$$

6.2.2 Sizing / Flow Rate Calculations

To achieve the desired cooling capacity, the required mass flow rate is calculated using Equation (45) and the following inputs.

$$\dot{m} = \frac{CoolingCapacity}{h_{evaporator_{out}} - h_{evaporator_{in}}} \tag{45}$$

- Cooling capacity is 1 kW at 35°C ambient
- Evaporator saturation temperature is 7.2°C
- Evaporator superheat is 5.8°K

Where, $h_{evaporator_{out}}$ is set by the saturation temperature of the evaporator and the evaporator superheat (Equation (46)) and $h_{evaporator_{in}}$ depends on the discharge point of the compressor.

$$h_{evaporator_{in}} = H(T^{sat}_{evaporator} + EvaporatorSuperHeat \tag{46}$$

The following EES code was developed to calculate the required mass flow rate for different compressor discharge pressures assuming

- Compression liquid temperature is 5°K higher than ambient
- Expansion from discharge pressure to evaporator pressure is isenthalpic
- Compression is isothermal

T_ambient = 35[C]

T_CL = T_ambient + 5[C]

Evap_superheat = 5.8[C]

T_evap = 7.2[C]

CoolingCapacity = 1[kW]

P_cond_out = 8000[kPa]

P_evap = **pressure**('CarbonDioxide', ***T***=T_evap, ***x***=0)

h_cond_out = **enthalpy**('CarbonDioxide', T = T_CL, P = P_cond_out)

h_evap_out = **enthalpy**('CarbonDioxide', T = T_evap+Evap_superheat, P = P_evap)

m_dot = CoolingCapacity / (h_evap_out - h_cond_out)

rho_comp_in = density('CarbonDioxide', T = T_evap + Evap_superheat, P = P_evap)

The results of this study are shown in Table 3.

6.2.3 Displacement Volume and Compression Liquid Flowrate

Mass flowrate of CO_2 is defined in terms of displacement volume and periodic time as shown below.

$$\dot{m} = \frac{\rho V}{\tau} \tag{47}$$

Table 3, Required CO_2 mass flow rate at different compressor discharge pressures.

Compressor discharge pressure, kPa	Compressor discharge pressure, psi	CO_2 mass flowrate, kg/s
8000	1168	0.0289
9333	1362.618	0.009132
10667	1557.382	0.007559
12000	1752	0.00707
13333	1946.618	0.006798
14667	2141.382	0.006615
16000	2336	0.006482
17333	2530.618	0.006379
18667	2725.382	0.006298
20000	2920	0.006232

Where ρ, the density of CO_2, is calculated at the beginning of the compression stroke (P = saturation pressure of evaporator, T = saturation temperature of the evaporator + evaporator superheat). τ is the total time of one cycle. It is the sum of the time it takes for the compression liquid flow and the time it takes for the compression liquid to flow back to its reservoir.

The displaced volume was calculated for each of the discharge pressures in Table 3 and different periodic times. These results are shown in Table 4.

For any set cycle time, the higher the discharge pressure the lower the required displaced CO2 volume. The rate of change of the required CO2 displaced volume however decreases significantly at pressure higher than 120 bar. For any discharge pressure, the required displaced CO2 volume is linearly proportional to the cycle time. Therefore, the compressor system will be designed for maximum working discharge pressure of 140 bar. Although increasing the discharge pressure beyond 120 bar does not result in reducing the required displaced volume, additional 20 bars are added for operational flexibility.

6.3 Results

To compare the results of the physics-based model and the isothermal process, the results were plotted for various flow rates in a 0.5-liter compression chamber and shown below. As shown in the figures below, temperature difference of around 4℃ is achievable during the compression process, but since the temperature and pressure are less than the critical conditions, condensation occurs.

As seen in Figure 42-Figure 51, as the heat transfer between CO_2 and oil is very high, temperature does not vary much and therefore same patterns occur including condensation. To reduce the heat transfer and show the results without spray, the following figures were plotted for a 0.5-liter compression chamber and 7 LPM flow rate.

Table 4, Displaced Volume in Liters.

Discharge pressure, kPa	Mass flowrate, kg/s	Periodic time (compression liquid flow time + drain time), seconds					
		3	5	7	10	15	20
8000	0.0289	0.7673	1.2788	1.7903	2.5575	3.8363	5.1150
9333	0.009132	0.2424	0.4041	0.5657	0.8081	1.2122	1.6163
10667	0.007559	0.2007	0.3345	0.4683	0.6689	1.0034	1.3379
12000	0.00707	0.1877	0.3128	0.4380	0.6257	0.9385	1.2513
13333	0.006798	0.1805	0.3008	0.4211	0.6016	0.9024	1.2032
14667	0.006615	0.1756	0.2927	0.4098	0.5854	0.8781	1.1708
16000	0.006482	0.1721	0.2868	0.4015	0.5736	0.8604	1.1473
17333	0.006379	0.1694	0.2823	0.3952	0.5645	0.8468	1.1290
18667	0.006298	0.1672	0.2787	0.3901	0.5573	0.8360	1.1147
20000	0.006232	0.1655	0.2758	0.3861	0.5515	0.8273	1.1030

6.4 IsoLiqComp Piping and Instrumentation Diagram (P&ID)

After meeting with the ORNL safety personnel and pressure systems subject matter expertise, an initial draft IsoLiqComp's piping, and instrumentation diagram (P&ID) was developed as shown in Figure 57.

This compressor has three main processes per cycle. These processes include filling the compression chamber with CO_2 (intake stroke), near-isothermal compression (compression stroke), and high-pressure discharge (release stroke). Each process is explained in detail and is shown on the corresponding P&ID with red lines as following.

6.4.1 Intake stroke, P&ID

As shown in the P&ID below (Figure 58), as the pressure read by PT-12 falls below a set pressure (20 bar in this study), V-12 control valve is opened and CO_2 passes through the pressure regulator PR-1 and the compression chamber is filled with vapor CO_2 until the set pressure is reached. A heater is added in-line with the pipes (red line) to prevent the temperature drop during CO_2 movement from the supply cylinder to the compression chamber. Check valve CV-2 and control valve V-12 are added to this line for flow control and flow meter FM-1, thermocouple I-6 and pressure transducer I-12 are added to this line for accurate data collection. The red line at the bottom of the compression chamber and the compression chamber specifications would be explained in discharge process.

6.4.2 Compression Stroke, P&ID

When the desired minimum pressure in compression chamber is reached (20 bar), V-12 is closed, V-11 and V-6 are opened, and the hydraulic positive displacement pump PP-1 is turned on starting the compression process shown in Figure 59.

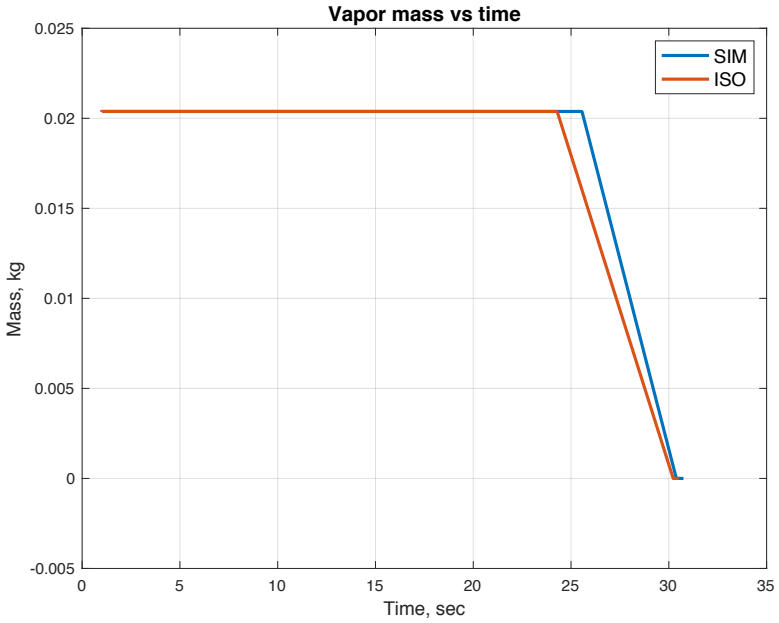

Figure 42, Vapor mass vs time, 1 LPM.

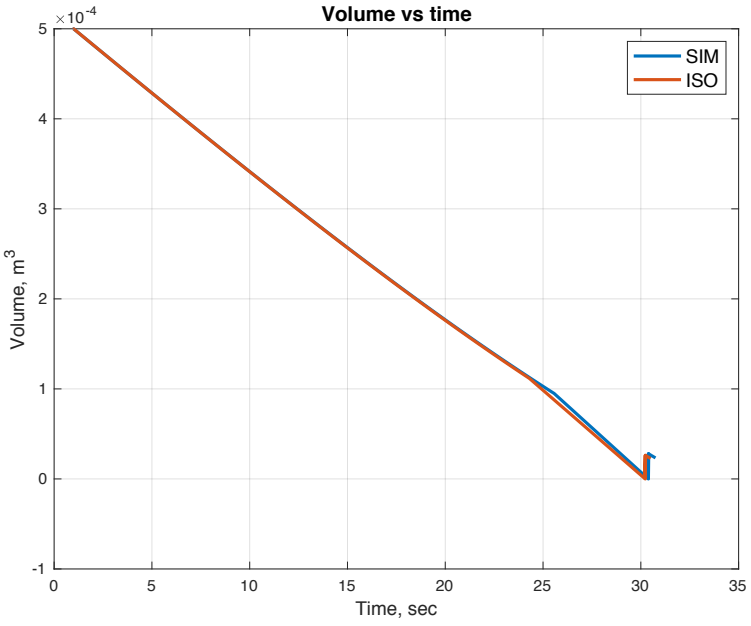

Figure 43, Total volume vs time, 1 LPM.

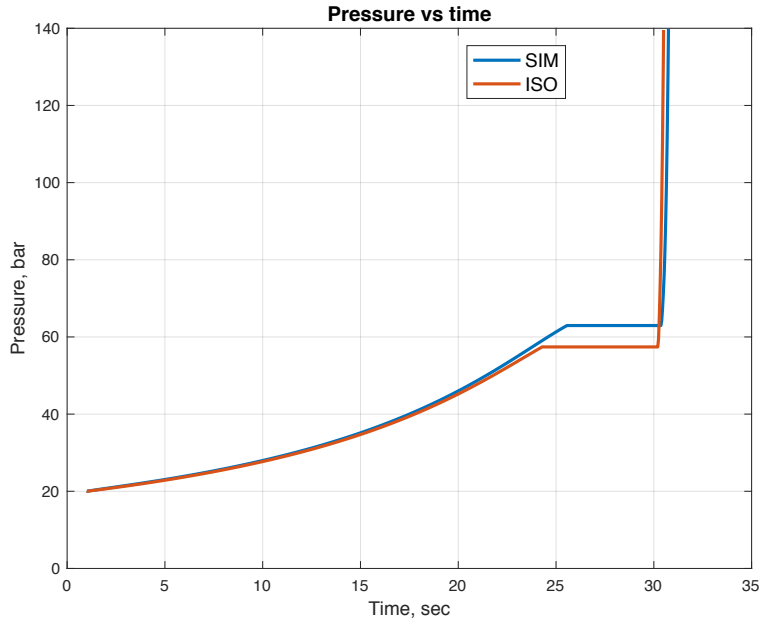

Figure 44, Pressure vs time, 1 LPM.

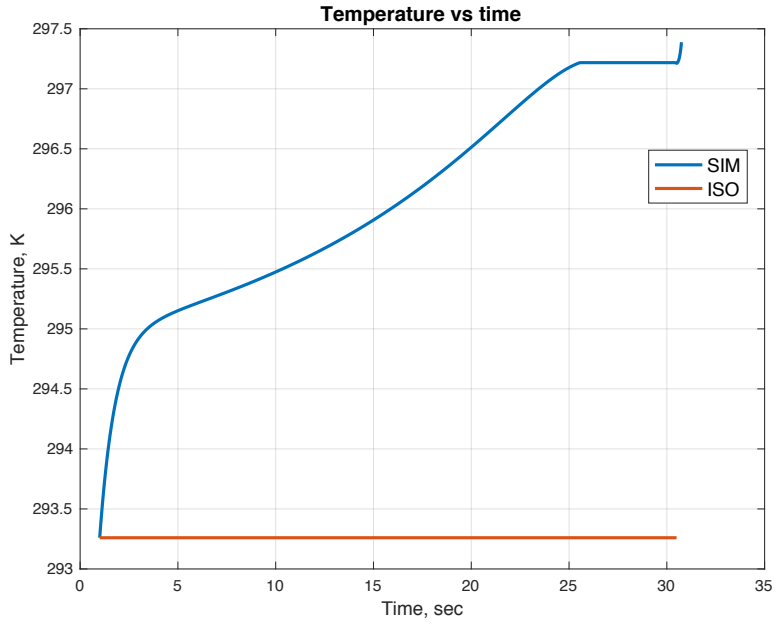

Figure 45, Temperature vs time, 1 LPM.

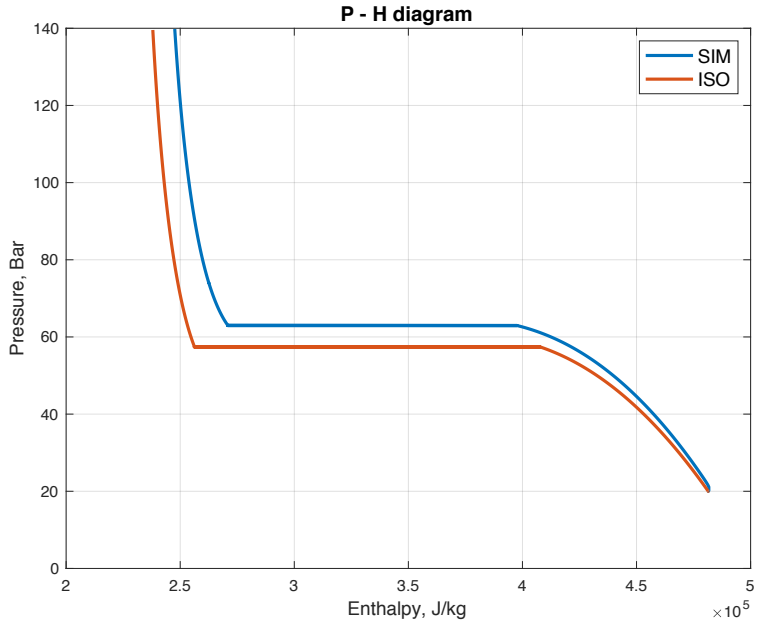

Figure 46, Pressure – Enthalpy diagram, 1 LPM.

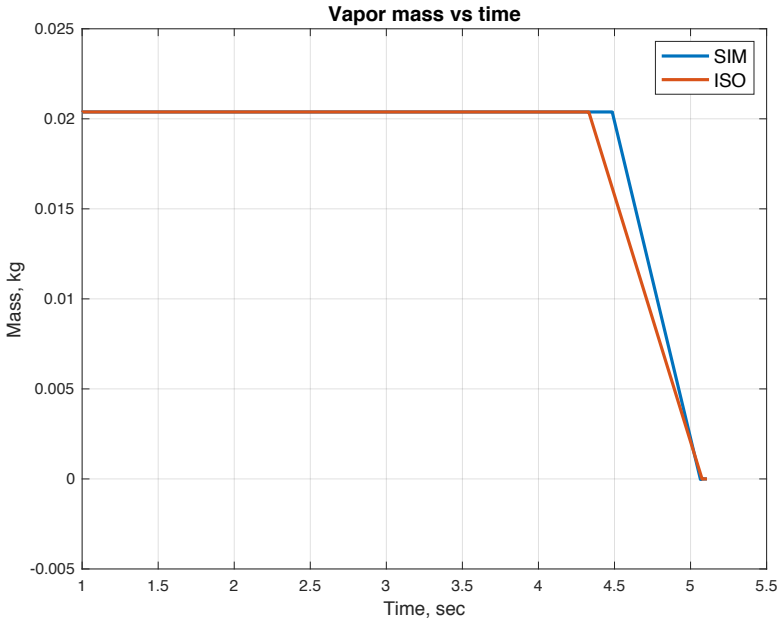

Figure 47, Vapor mass vs time, 7 LPM.

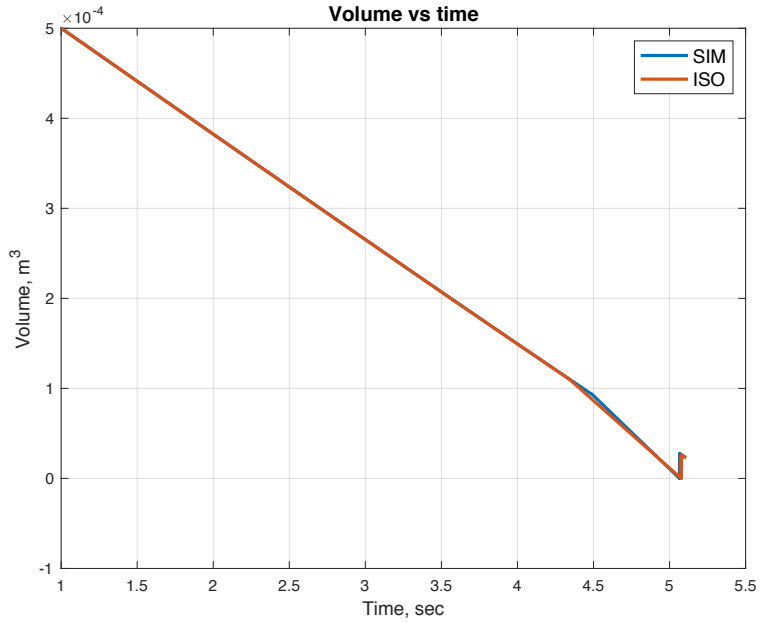

Figure 48, Total volume vs time, 7 LPM.

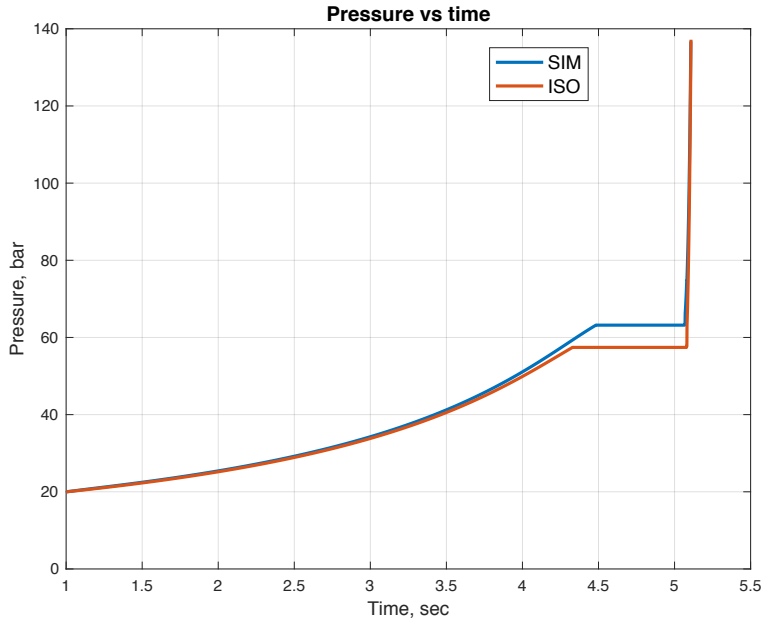

Figure 49, Pressure vs time, 7 LPM.

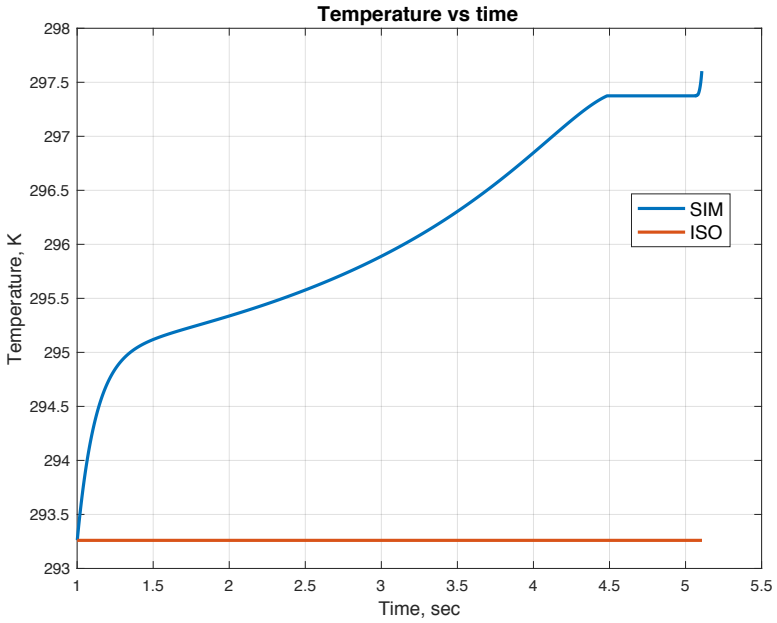

Figure 50, Temperature vs time, 7 LPM.

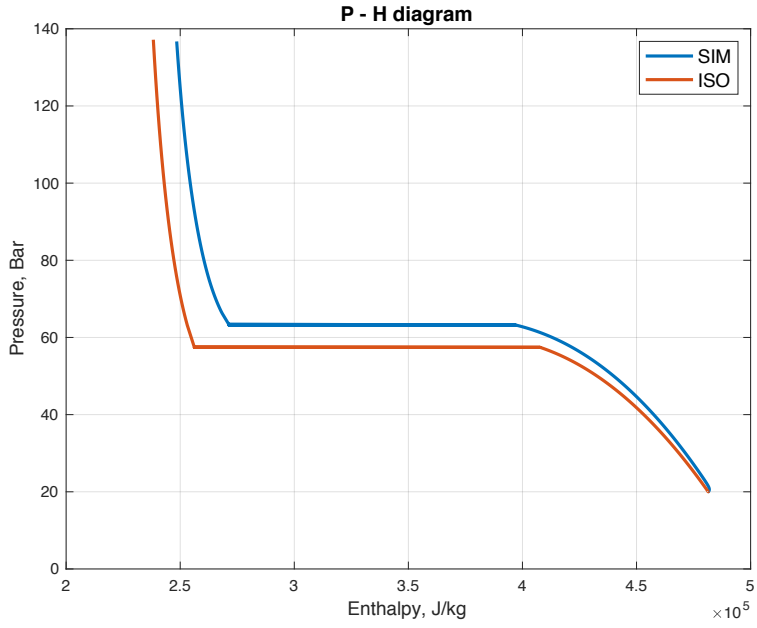

Figure 51, Pressure – Enthalpy Diagram, 7 LPM.

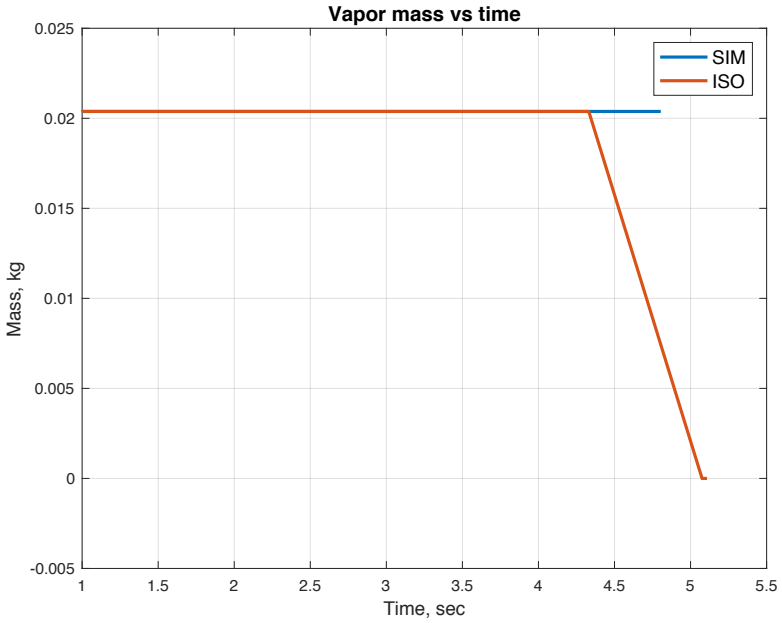

Figure 52, Vapor mass vs time, 7 LPM – no direct heat transfer with droplets.

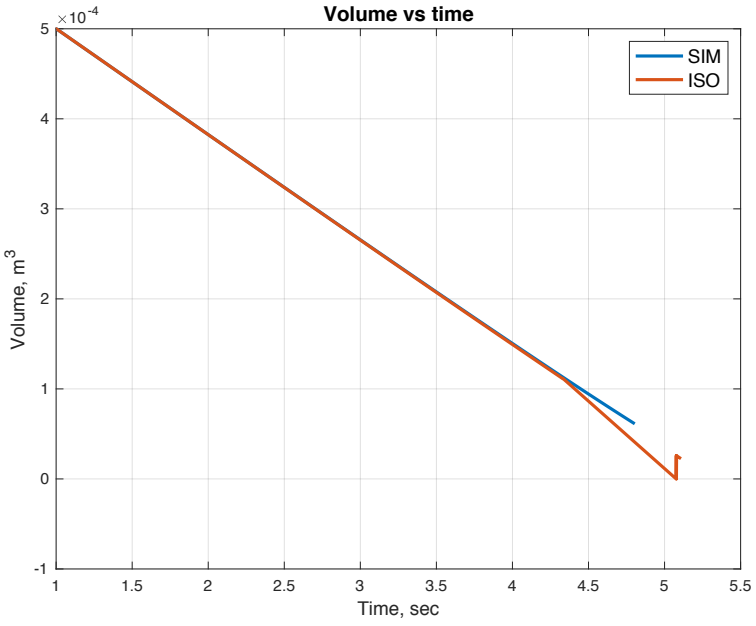

Figure 53, Total volume vs time, 7 LPM – no direct heat transfer with droplets.

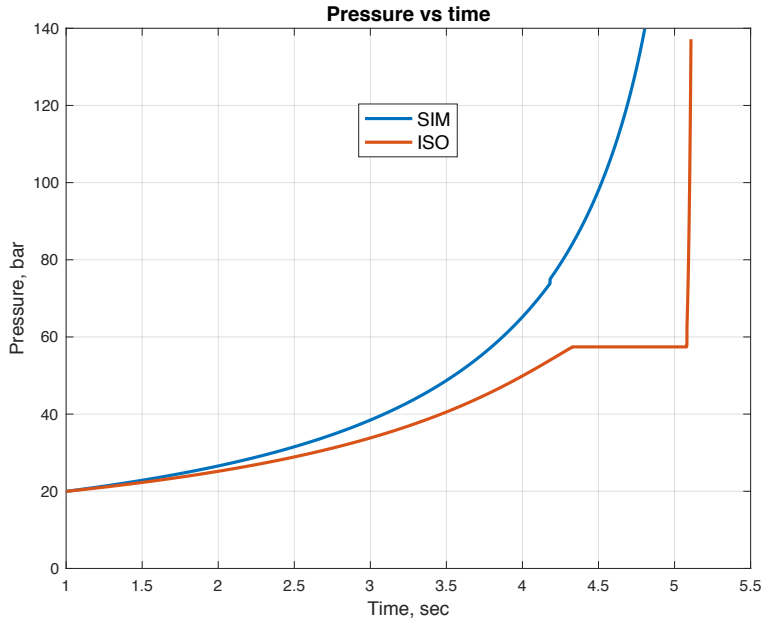

Figure 54, Pressure vs time, 7 LPM – no direct heat transfer with droplets.

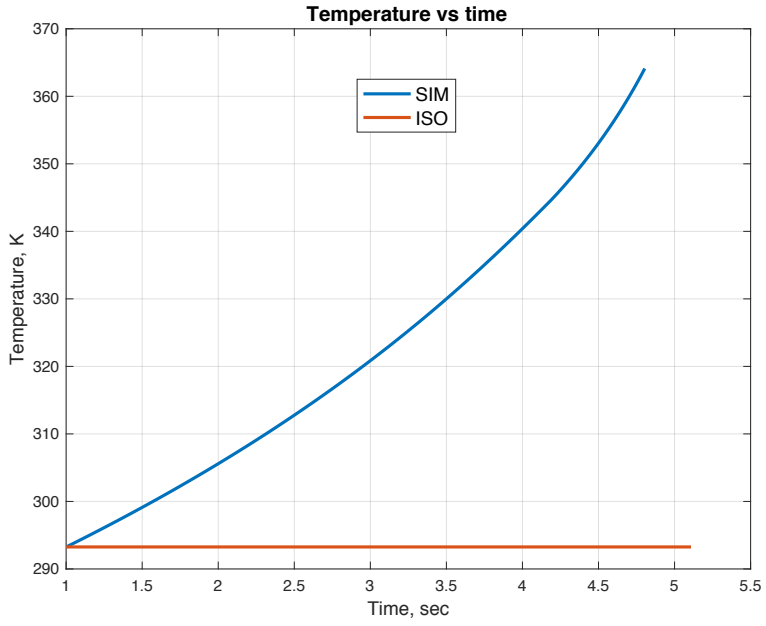

Figure 55, Temperature vs time, 7 LPM – no direct heat transfer with droplets.

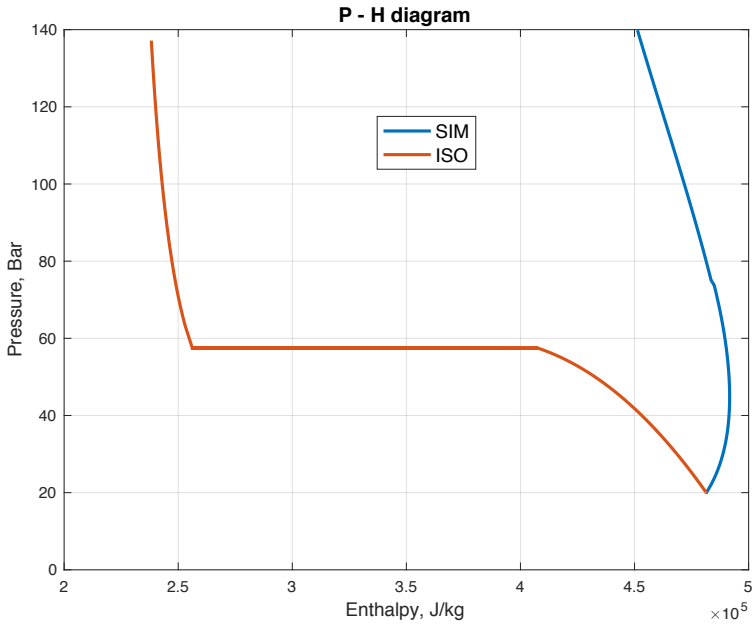

Figure 56, Pressure – Enthalpy, 7 LPM – no direct heat transfer with droplets.

Oil is pumped from the atmospheric-pressure reservoir E-1 to the compression chamber and is sprayed from the top into the compression chamber falling from the top to the existing oil level in the chamber. Flow meter FM-2, watt transducer I-17, and thermocouple I-8 are added to this line to monitor the oil flow rate, power consumption, and oil temperature respectively. Check valve CV-1 is also added for flow control purposes.

6.4.3 Discharge stroke, P&ID

As the compression process continues, the backpressure regulator PR-2 is set to open when the pressure inside the compression chamber reaches the maximum set pressure (140 bar in this study). As shown in Figure 60, with the control valve V-9 open, as the pressure reaches the maximum set pressure, PR-2 opens and high-pressure CO_2 is released flowing through a catch can CC-1 designed to capture any oil and return it to the oil reservoir while releasing CO_2 into the ambient.As the compressed CO_2 is discharged, as explained above and Figure 58, V-12 is opened and low pressure CO_2 enters the compression chamber pushing the oil from the previous cycle out of the compression chamber back to the oil reservoir E-1.

This marks the completion of one full cycle of the IsoLiqComp near-isothermal compressor.

6.5 IsoLiqComp Prototype Parts

As shown in the IsoLiqComp P&IDs, the main equipment which would be used to design and develop the first prototype, include the CO_2 supply cylinder which feeds the CO_2 to the compression chamber, the compression chamber, and the positive displacement hydraulic pump. All the materials needed are summarized in Table 5. Two heat exchangers (one heater and one chiller) are also added to the system and were shown on the P&ID.

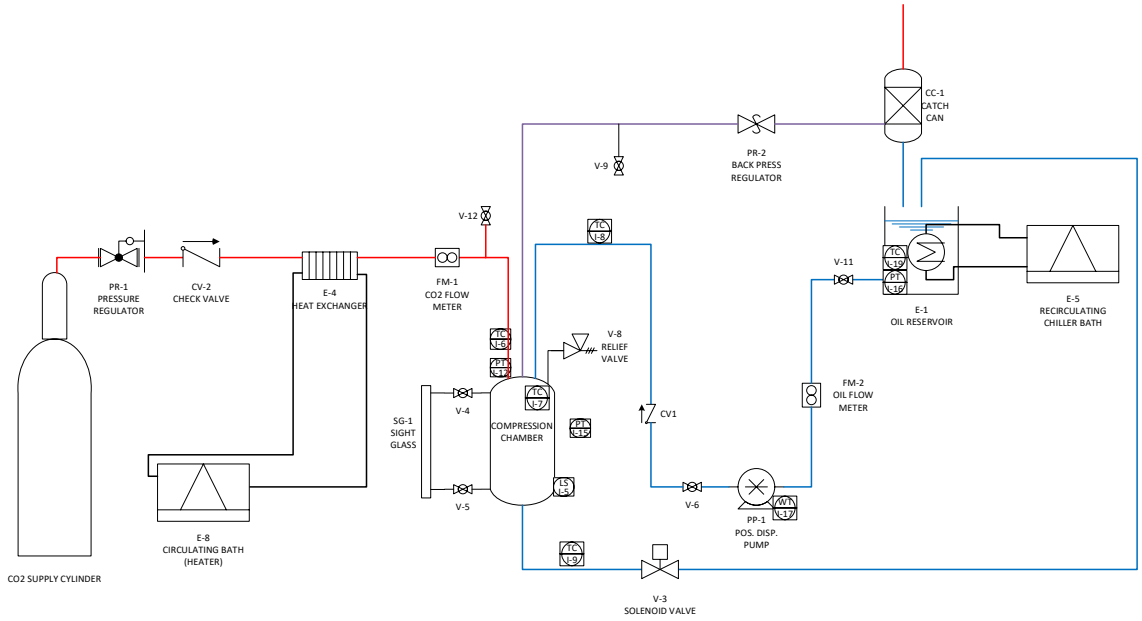

Figure 57, IsoLiqComp P&ID.

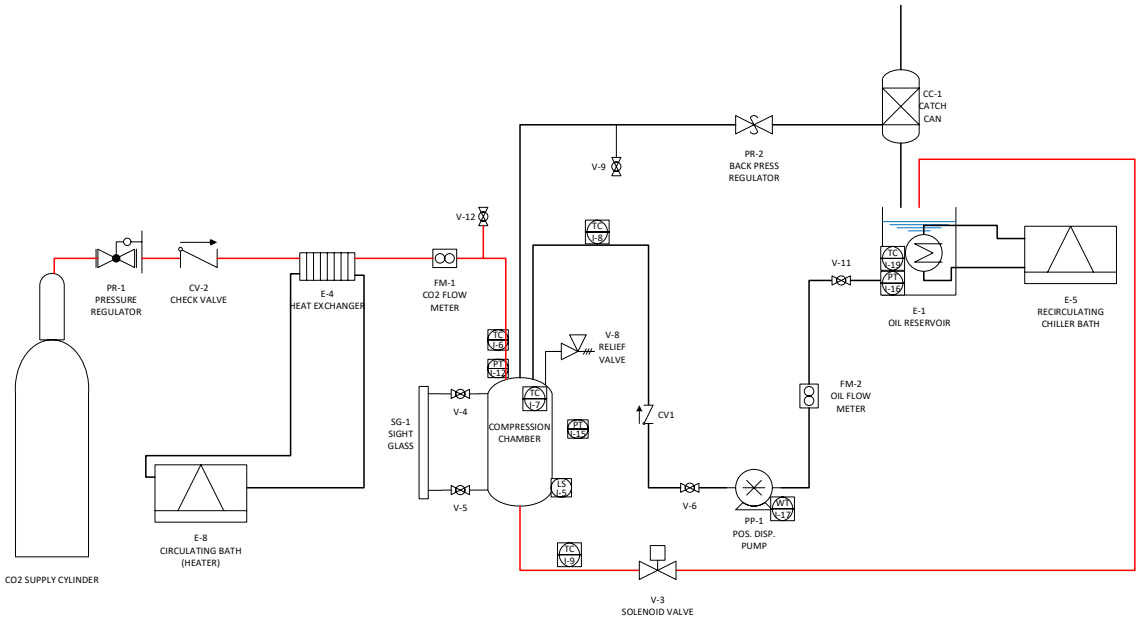

Figure 58, Intake stroke P&ID.

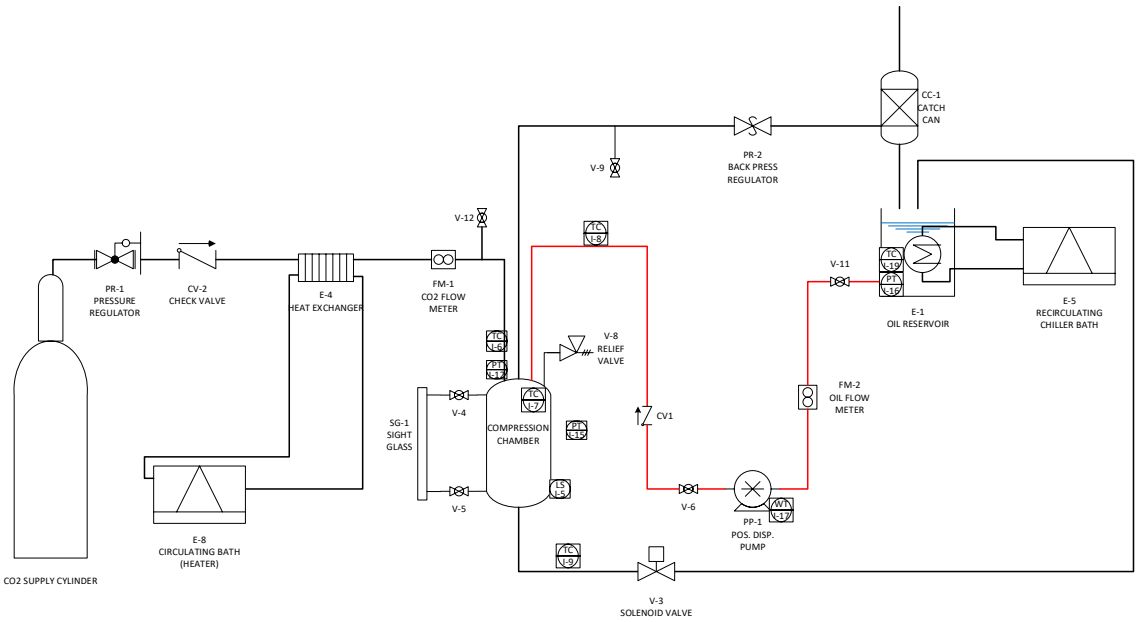

Figure 59, Compression stroke P&ID.

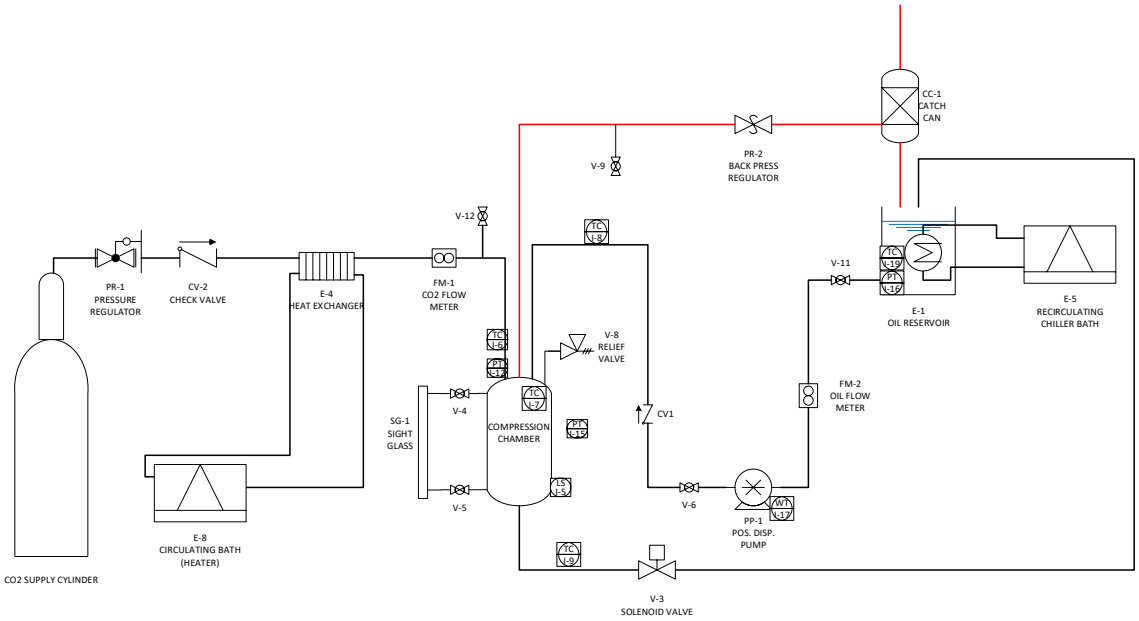

Figure 60, Discharge stroke P&ID.

Table 5, Bill of materials.

Equipment/Instrumentation	Range	Unit
Pressure transducer	140	barg
T-Type thermocouple	-	C
Ball valves	140	bar
Flow meter	50	g/s
Flow meter	7.2	lpm
Watt transducer	3	kW
Level Switch	-	-
Pressure Regulator	275	bar
Oil-Gas separator	17	bar
Backpressure regulator	Adjustable	bar
Sight glass	172	bar
Pump	172	bar
Reservoir	3	gal
Heat exchanger	-	-
Catch can	145	bar
Compression chamber	1	lit

The compression chamber is designed as a 1-liter chamber capable of handling pressures up to 140 bar and temperatures up to 40℃. The detailed design sketch of the compression chamber is shown in Figure 61.

6.6 Future Design

The first-generation prototype of the Isothermal Liquid Compressor, IsoLiqComp, was designed to study the compressor behavior and validate the physics-based performance model using the experimental data. Future design of the compressor involves a double chamber closed-loop compressor capable of circulating the working fluid between the two chambers. An early stage design of the next generation IsoLiqComp was developed and is shown in Figure 63.

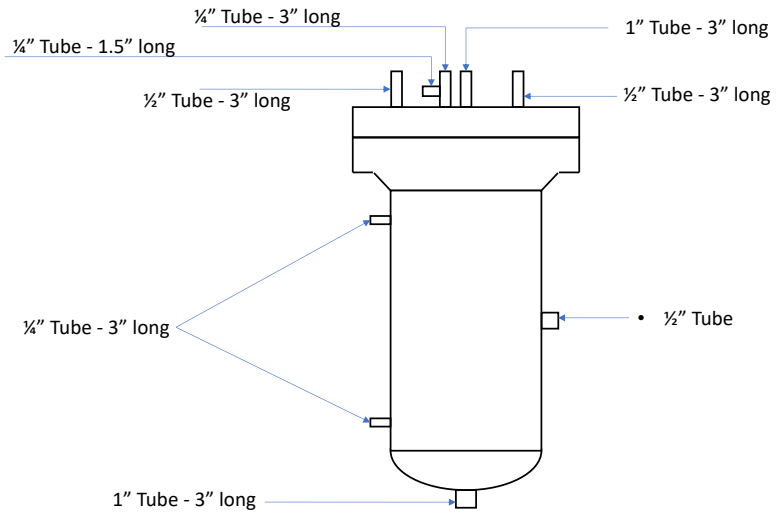

Figure 61, Compression chamber sketch.

Figure 62, IsoLiqComp First Prototype.

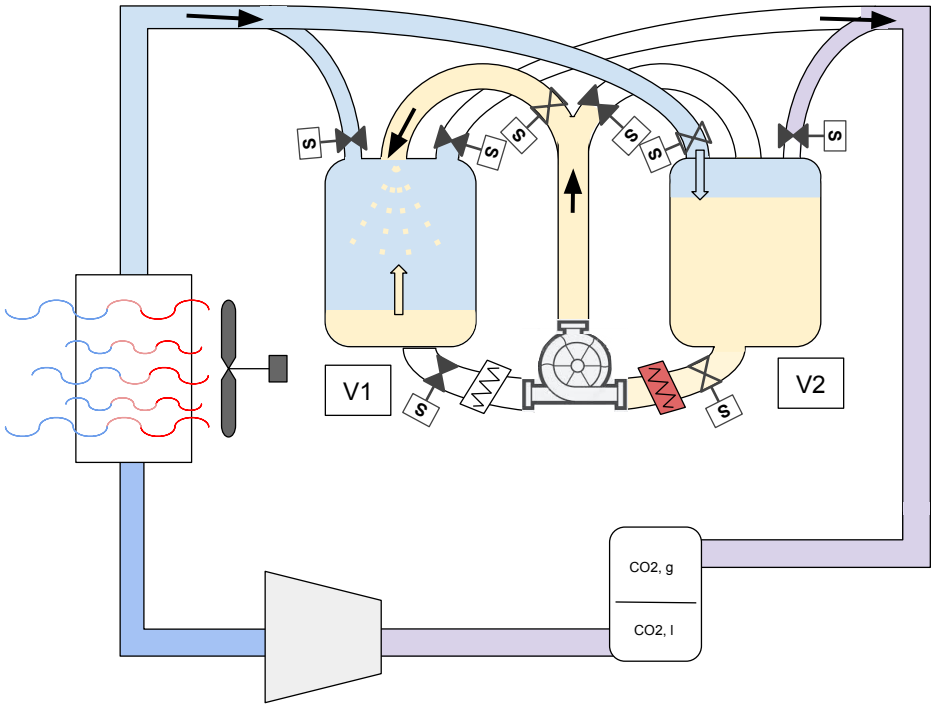

Figure 63, IsoLiqComp 2nd generation design.

Chapter 7: Technoeconomic Analysis

Manufacturing of carbon steel vessels is largely non-automated. High manual labor and welding costs are associated with the manufacturing of steel vessels, causing them to be the dominant cost items of GLIDES. To meet DOE's target cost, several other pressure reservoirs are investigated in this chapter including carbon fiber pressure vessels and high-pressure pipe segments. Carbon fiber vessels and high-pressure pipe segments are less expensive as they are mass manufactured semi-automatically and fully automatically, respectively. A techno-economic model of the GLIDES system (including the performance model explained above and a cost model), detailed results comparing pressure reservoirs, and further cost reduction opportunities are discussed in this chapter.

7.1 Cost Model

To compare the costs associated with the systems using steel vessels, carbon fiber pressure vessels, and high-pressure pipe segments, a cost analysis model was developed using the MATLAB programing package. The cost analysis model is an optimization model that solves for the lowest *$/kWh* system cost based on steel and carbon fiber pressure vessels and high-pressure pipe segments cost data gathered from manufacturers to build the desired GLIDES system size. As shown in Figure 64, the model takes the desired system size (*kWh*), an estimated roundtrip efficiency value, a pressure ratio (max/min pressure), and the pressure reservoir data (diameter, height, volume, maximum pressure, and price per vessel) from the manufacturers as the input. Using these inputs, based on the boundary work relation in a polytropic process ($W_b = \int_1^2 PdV\,, P = CV^n$) the amount of energy which can be stored per unit volume is calculated using (48). It then solves for the total storage volume needed based on the total energy storage needed

and the desired system capacity (kWh) using (49). Based on (49) and vessel volume data from the manufacturer, the number of vessels needed to meet the desired system are calculated. Knowing the number of vessels needed and the cost per vessel, the cost model calculates the total cost and finds the pressure reservoir that results in the minimum cost. Based on the number of vessels, the cost model then adds the cost of the required piping, fittings, and valving along with the cost associated with selected motor/pump and turbine/generator. Summing up these costs, the model then once again looks for the option with the lowest total cost. As the data is different for different pressure reservoirs being studied, separate models were made for each system (pressure reservoir) type.

$$E_{st} = \frac{p_{max}\left(\frac{p_{max}}{p_{min}}\right)^{-\frac{1}{n}} - p_{min}}{1-n} \tag{48}$$

$$V_{st} = \frac{Rated\ Power\ \times\ storage\ time}{\eta_{RTE}\ \times\ E_{st}} \tag{49}$$

As discussed above, one of the inputs into the cost model is the pressure ratio. This is the ratio of maximum to minimum pressure of the working gas in the pressure reservoir, which is the range of pressure the system operates between. As the maximum allowable operating pressures of pressure reservoirs are set input data gathered from the manufacturers, the minimum pressure can be set to any pressure. This minimum pressure is the initial air pressure the system is pre-pressurized to. To determine the optimal pressure ratio (i.e., the best minimum pressure the system should initially be pressurized to), a physics-based performance model was developed. The physics-based performance model simulates the system transient profile (i.e., liquid/gas volume, temperature,

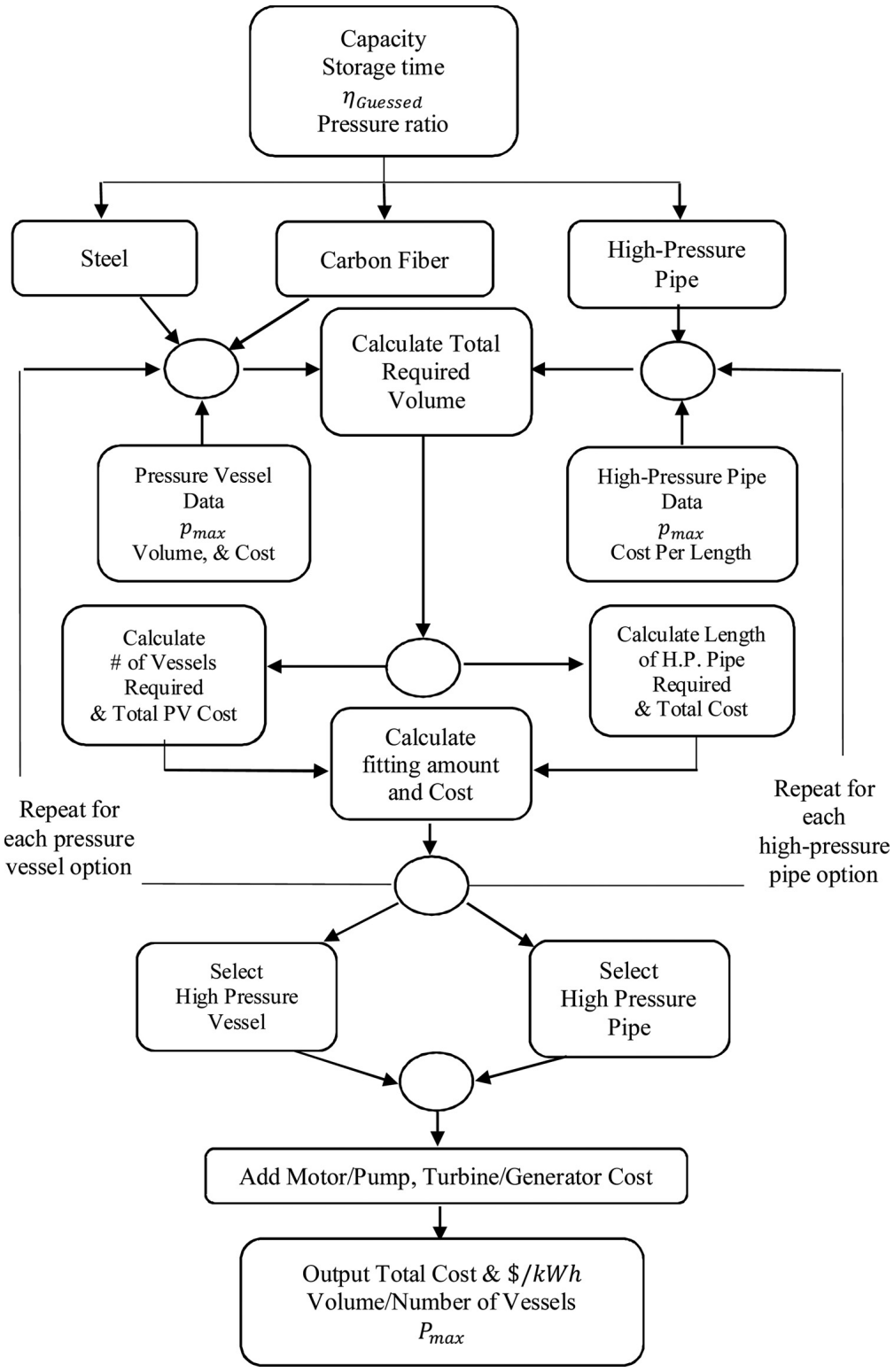

Figure 64, Cost Model flow chart [37].

pressure behavior) and the energy stored in the system at any time. As the required storage volume in the cost model is a function of the roundtrip efficiency, the cost model benefits from interaction with the performance model.

7.2 Entrance Model

To combine the manufacturers' data, the cost model, and the physics-based performance model, an entrance model was introduced Figure 65. With overall system inputs of desired storage capacity (*kWh*) and an estimated value for the roundtrip efficiency, the cost model optimizes the system design for the lowest cost. The cost model outputs the selected pressure reservoir's parameters, maximum pressure, number of vessels, and total projected *$/kWh* capital cost. In taking the system parameters, maximum pressure, and the number of vessels from the cost model, the physics-based performance model simulates the gas/water behavior and outputs work and power profile and an updated roundtrip efficiency based on the performance of the selected system. The overall model then outputs the total system cost, the *$/kWh* cost, transient profile, and the updated roundtrip efficiency. The updated roundtrip efficiency is then fed back into the cost model to now run the calculations/optimization with an improved value for roundtrip efficiency. The system runs the loop until the lowest cost is found and a stope criteria for small change in the roundtrip efficiency is met and outputs the final values for cost, efficiency, and the transient profile.

7.3 Results

Energy storage systems, depending on their scalability, can be used in both household and grid applications. To analyze the cost and performance of GLIDES for these two applications, a system was sized for steel, carbon fiber pressure vessels, and high-pressure pipe segments and for system capacities ranging from 10 *kW* (close to Tesla's Powerwall [38]) to 300 *MW* (close to that of a

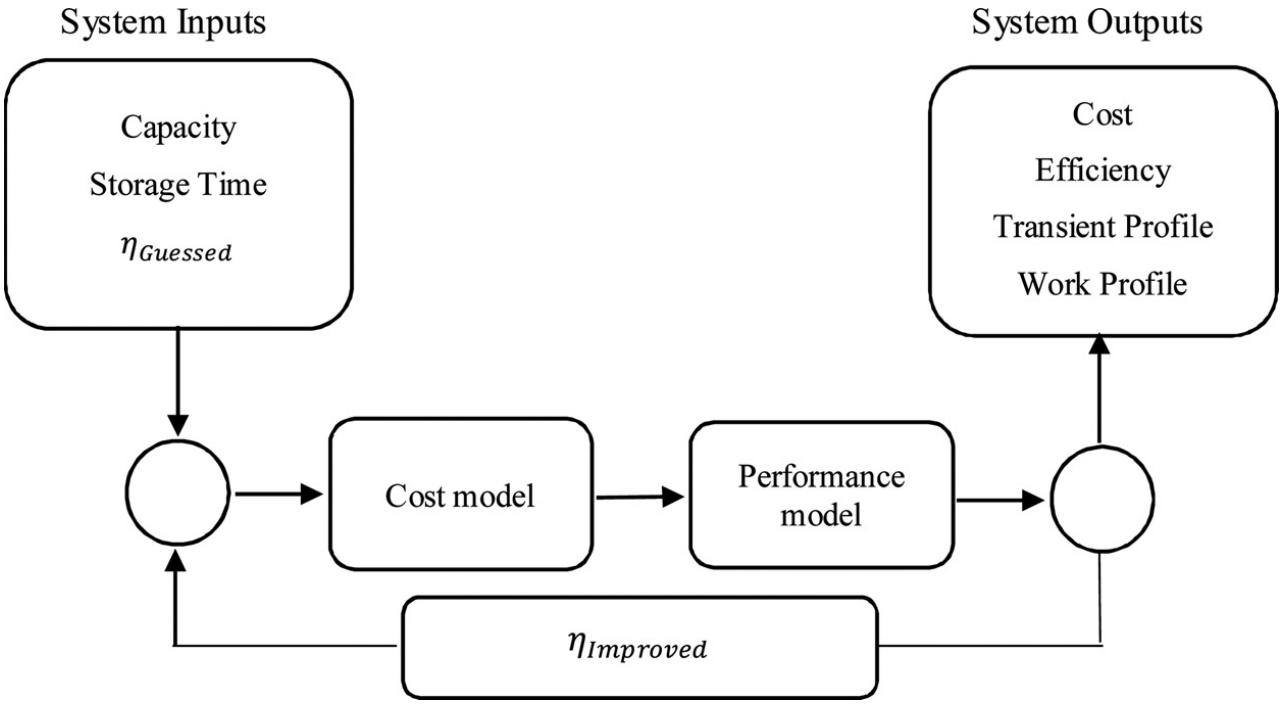

Figure 65, Overall model flow chart [37].

CAES plant). These systems were sized for storage hours ranging from 2 to 6 *hours* and pressure ratios ranging from 1.3 to 20. As explained above, the only controllable parameters in this analysis are the type of the pressure reservoirs, the system's energy capacity, hours of storage, and pressure ratio (P_{max}/P_{min}). On the other hand, the goal of this analysis is to find the system with the highest energy density, highest roundtrip efficiency, and lowest cost. Therefore, to do this analysis, from the studied systems, the change in system cost per *kWh* with the change in the system size (*kWh*) and pressure ratio was significant. As anticipated, the total cost of the system increased with the increase in system size, but the *$/kWh* cost of the system decreased. Another interesting trend was the change in the system *$/kWh* cost and energy density with the change in pressure ratio. To analyze the change in *$/kWh* and the ED with the change in pressure ratio, these data were plotted on the same chart, with *$/kWh* on the left axis and ED on the right axis for a 100 *kW* system with 2, 4, and 6 *hours* of storage and pressure ratios ranging from ~1 to ~20. The system roundtrip efficiency did not change much and ranged between ~75–80%. As shown on the left axis of Figure 66, *$/kWh* system cost decreases between pressure ratios of ~1.3 and ~2.7 and increases from ~2.7 to ~20. The lowest *$/kWh* cost in this trend occurs at a pressure ratio of ~2.7. As shown on the second axis of Figure 66, the energy density of the said system increases between pressure ratios of ~1.3 to ~2.7 and decreases from ~2.7 to ~20. The highest ED of the system is measured at pressure ratio of ~2.7, at which the lowest cost occurs. A pressure ratio of 2.7 means that if the maximum allowable pressure of a pressure reservoir is ~200 *bars* (set by manufacturer), to have a system with the maximum ED and lowest *$/kWh*, each pressure reservoir (within the studied cases) best be pre-pressurized to ~74 *bar* air pressure. This pressure ratio, as shown in Figure 66, is found to be the best pressure ratio for all the pressure reservoirs studied. Experimental results also suggest a polytropic constant of $\mathrm{n} = 1.2$ for the GLIDES system. These data can be proved by

differentiating (48) with respect to the P_{min}, which can give the optimum pressure ratio using (50) (using $n = 1.2$ polytropic constant as during the base configuration), suggesting that the best pressure ratio for the system, at which the energy storage per unit volume is maximized, can be described as:

$$\left(\frac{P_{max}}{P_{min}}\right)_{optimum} = n^{\left(\frac{n}{n-1}\right)} \tag{50}$$

7.3.1 Parametric Analysis

To analyze the cost of GLIDES at various scales, the cost of GLIDES using steel pressure vessels, carbon fiber pressure vessels, and pipe segments was analyzed in this section. Some detailed simulation data including system capacity, number of vessels, and cost are included in Appendix A, B, and C.

7.3.1.1 Steel Pressure Vessels

The cost of GLIDES using steel pressure vessels ranges from *$*4,500*/kWh* for a 300 *MW* and 6 *hours* system with a 2.7 pressure ratio to *$*5,100*/kWh* for a 10 *kW* and 2 *hours* system with a 2.7 pressure ratio.

The cost and efficiency of a 100 *kW* and 2 *hours* system and a 2.7 pressure ratio is analyzed. As shown in Figure 67(a), ~93% of the system cost is associated with the cost of the steel pressure vessels, followed by ~3% in turbine/generator cost, ~3% in valve cost, and ~1% in pump/motor, piping, and fitting costs. For the 200 *kWh* system studied, ~160 3,000-liter steel pressure vessels with a maximum pressure of 200 *bar* are needed to meet the storage requirements.

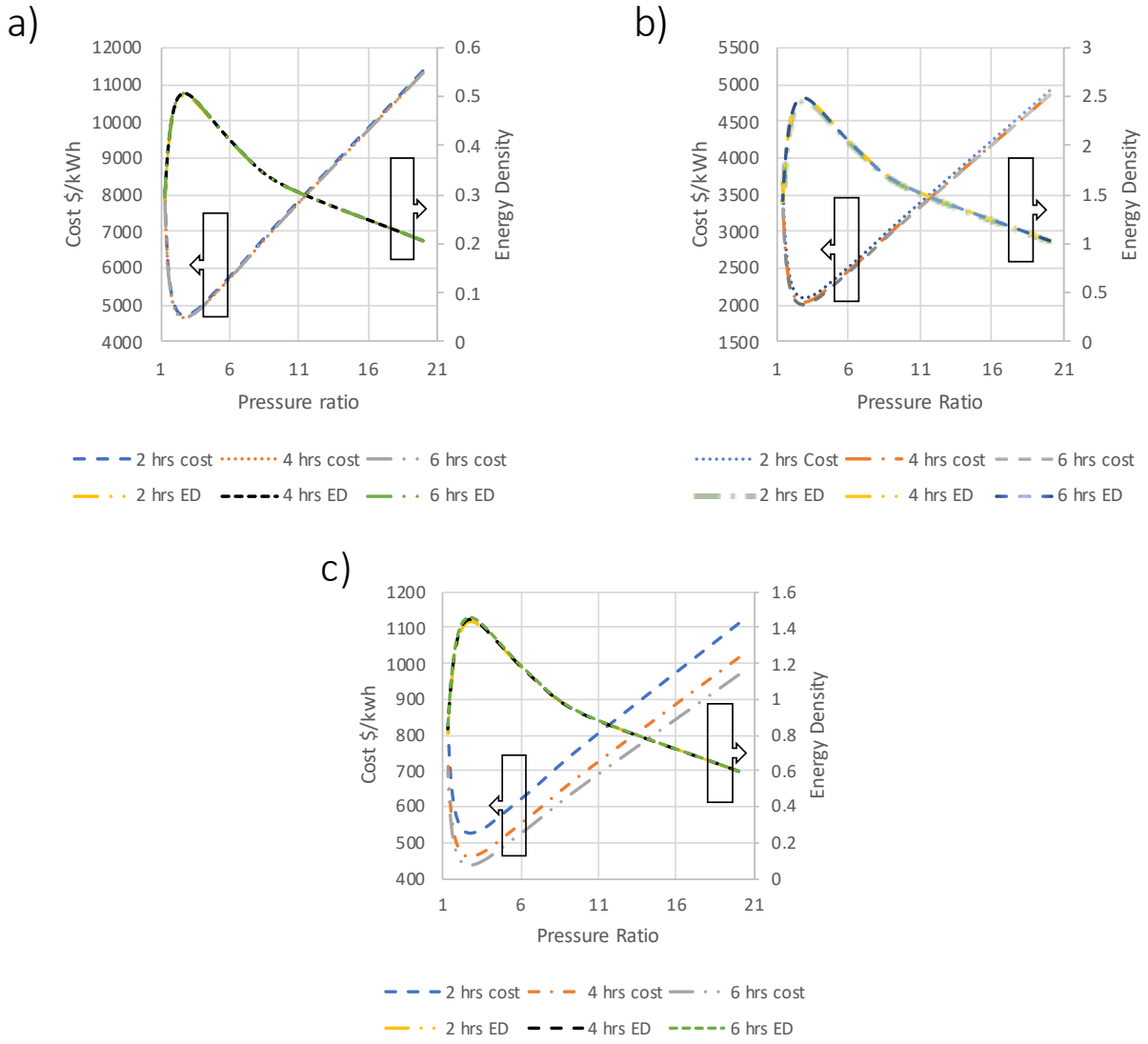

Figure 66, Parametric study, cost ($/kWh) and energy density vs. pressure ratio for the systems with (a) steel pressure vessels, (b) carbon fiber vessels, and (c) high-pressure pipe segments as the pressure reservoir [37].

A total cost of ~*$*1,200k and ~*$*4,700*/kWh* is calculated for this system. This total cost can be broken down into ~*$*1,190k in steel pressure vessel cost, ~$33k in turbine/generator cost, ~*$*8k in motor/pump cost, and ~*$*4k in fitting, valve, and piping cost. As explained above, RTE and ED are two important performance characteristics of any energy storage technology. A pie chart in Figure 67(b) shows the breakdown of efficiency losses in this system (a constant efficiency of 90% is assumed for the turbomachinery of the GLIDES system which has an RTE of ~83% with an energy density of ~0.51 kWh/m^3. The rate of change of cost with changing the storage length is shown in Figure 68.

7.3.1.2 Carbon Fiber Pressure Vessels

The cost of GLIDES using carbon fiber pressure vessels ranges from *$*760*/kWh* for a 10 *MW* and 3 *hours* system and a 2.7 pressure ratio to *$*1,000*/kWh* for a 100 *kW* and 1 *hour* system and a 2.7 pressure ratio.

The cost and efficiency of a 100 *kW* and 2 *hours* system and a 2.7 pressure ratio is analyzed. As shown in Figure 69(a), ~74% of the system cost is associated with the cost of the carbon fiber pressure vessels, followed by ~12% in turbine/generator cost, ~5% in valve cost, and ~8% in pump/motor, piping, and fitting costs. For the 200 *kWh* system studied, ~120 900-liter carbon fiber pressure vessels with a maximum pressure of 248 *bar* are needed to meet the storage requirements. A total cost of ~$650k and ~*$*2,100*/kWh* is calculated for this system. This total cost can be broken down to ~*$*580k in carbon fiber pressure vessel cost, ~*$*33k in turbine/generator cost, ~*$*15k in valve cost, and ~*$*23k in pump/motor, fitting, and piping cost. The pie chart in Figure 69(b) shows the breakdown of efficiency losses in this system which has an RTE of ~74% with an energy density of ~2.45 kWh/m^3. Costs as low as *$*736*/kWh* for a 100 MW 10 hours system can be

achieved and range up to *$835/kWh* for a 10 MW 1 hour system with a 2.7 pressure ratio as seen in Figure 70.

7.3.1.3 High-Pressure Pipe Segments

The cost of GLIDES using high-pressure pipe segments ranged from *$250/kWh* for a 300 *MW* and 6 *hours* system and a pressure ratio of 2.7 to *$1,100/kWh* for a 10 *kW* and 2 *hours* system and a 2.7 pressure ratio.

The cost analysis of a 100 *kW* and 2 *hours* system and a 2.7 pressure ratio is analyzed. As shown in Figure 71(a), ~78% of the system cost is associated with the cost of the high-pressure pipe segments, ~15% in turbine/generator cost, ~4% in motor/pump, and less than 1% in piping, fitting, and valve costs. For the 200 *kWh* system, ~32 30-meter-long pipe segments with a volume of ~6,200 *liters* and a maximum pressure of 145 *bar* are needed to meet the storage requirement.

A total cost of ~*$225k* and ~*$715/kWh* is calculated for this system. This total cost can be broken down to ~*$176k* in pipe segment cost, ~*$33k* in turbine/generator cost, ~*$8k* in motor/pump cost, and ~*$8k* in fitting, valve, and piping cost. The pie chart in Figure 71(b) shows the breakdown of efficiency losses in this system which has an RTE of ~76% with an energy density of ~1.42 kWh/m^3. Figure 72 shows the rate of change of cost.

As explained above, GLIDES cost depends on various parameters including the thermodynamic efficiency. To study the effects of the increase in this efficiency and decrease in compression losses while employing spray cooling, the physics-based performance model developed above is combined with the cost model. To study the effect of thermodynamic efficiency on the total capital cost and energy density, the isothermal, adiabatic, and experimental data were gathered using the physics-based performance model.

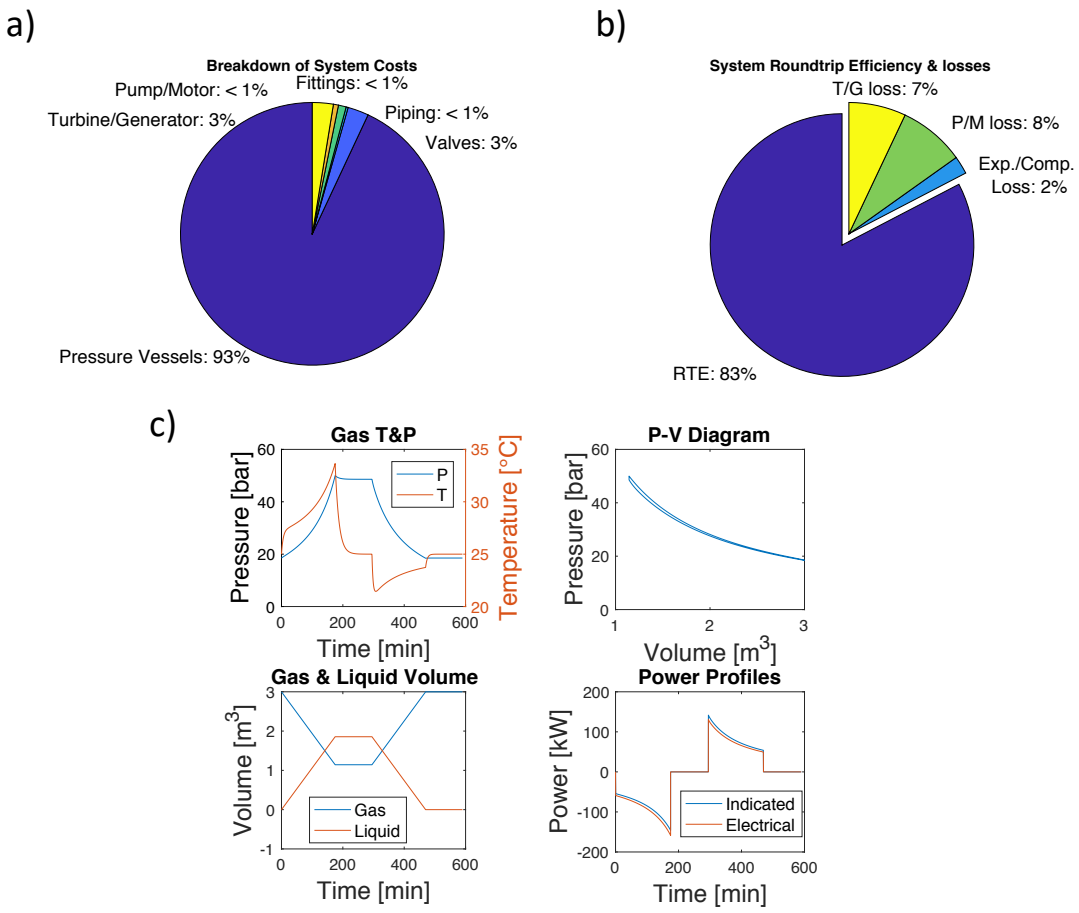

Figure 67, (a) System cost breakdown, (b) roundtrip efficiency/losses, and (c) performance of a 200 kWh system, steel pressure vessel.

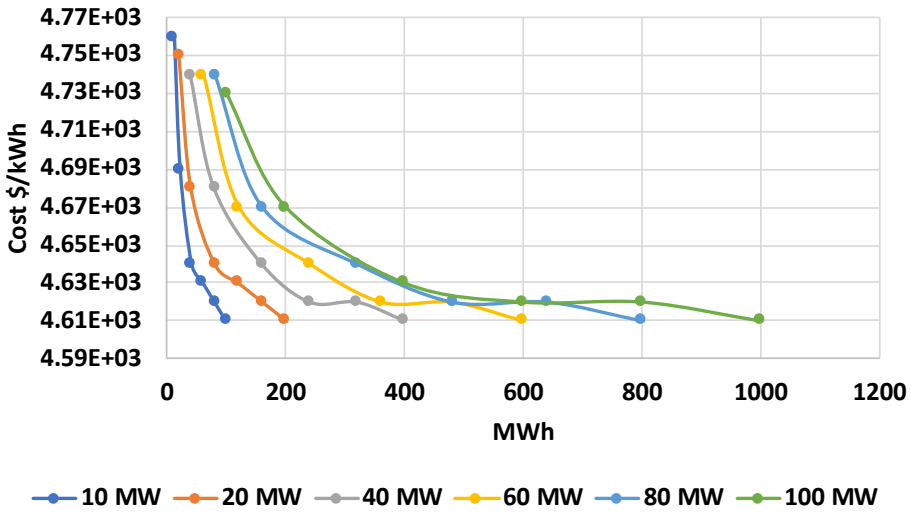

Figure 68, Cost rate of change for a grid-scale GLDIES using steel pressure vessels.

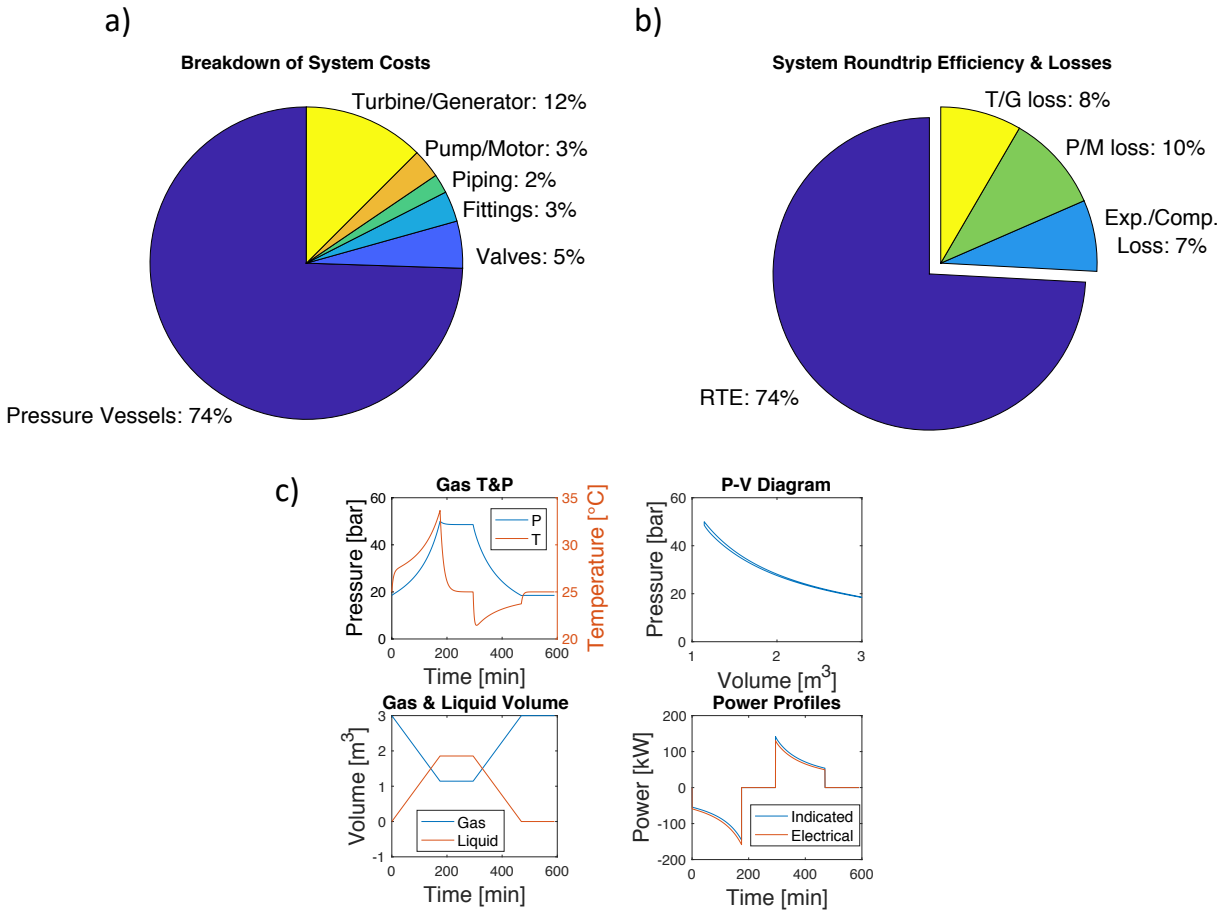

Figure 69, (a) System cost breakdown, (b) roundtrip efficiency/losses, and (c) performance of a 200 kWh system, carbon fiber pressure vessel.

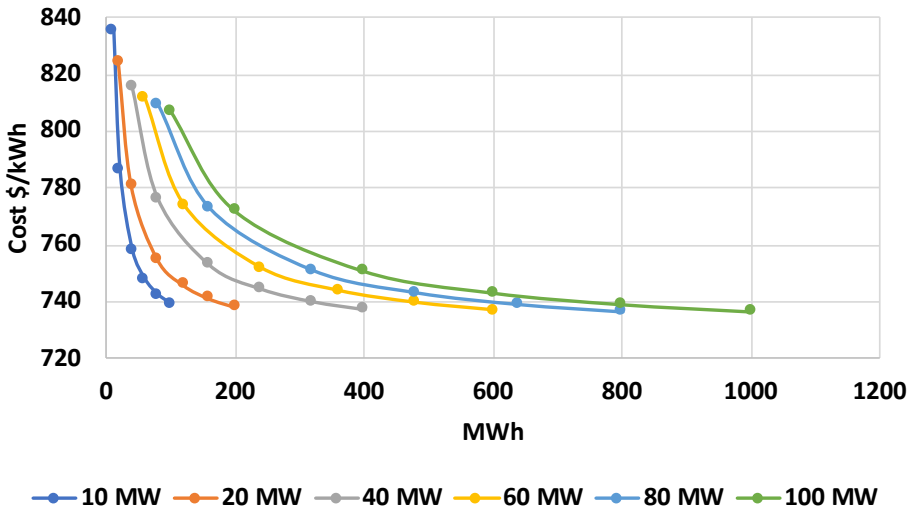

Figure 70, Cost rate of change for a grid-scale GLDIES using carbon fiber pressure vessels.

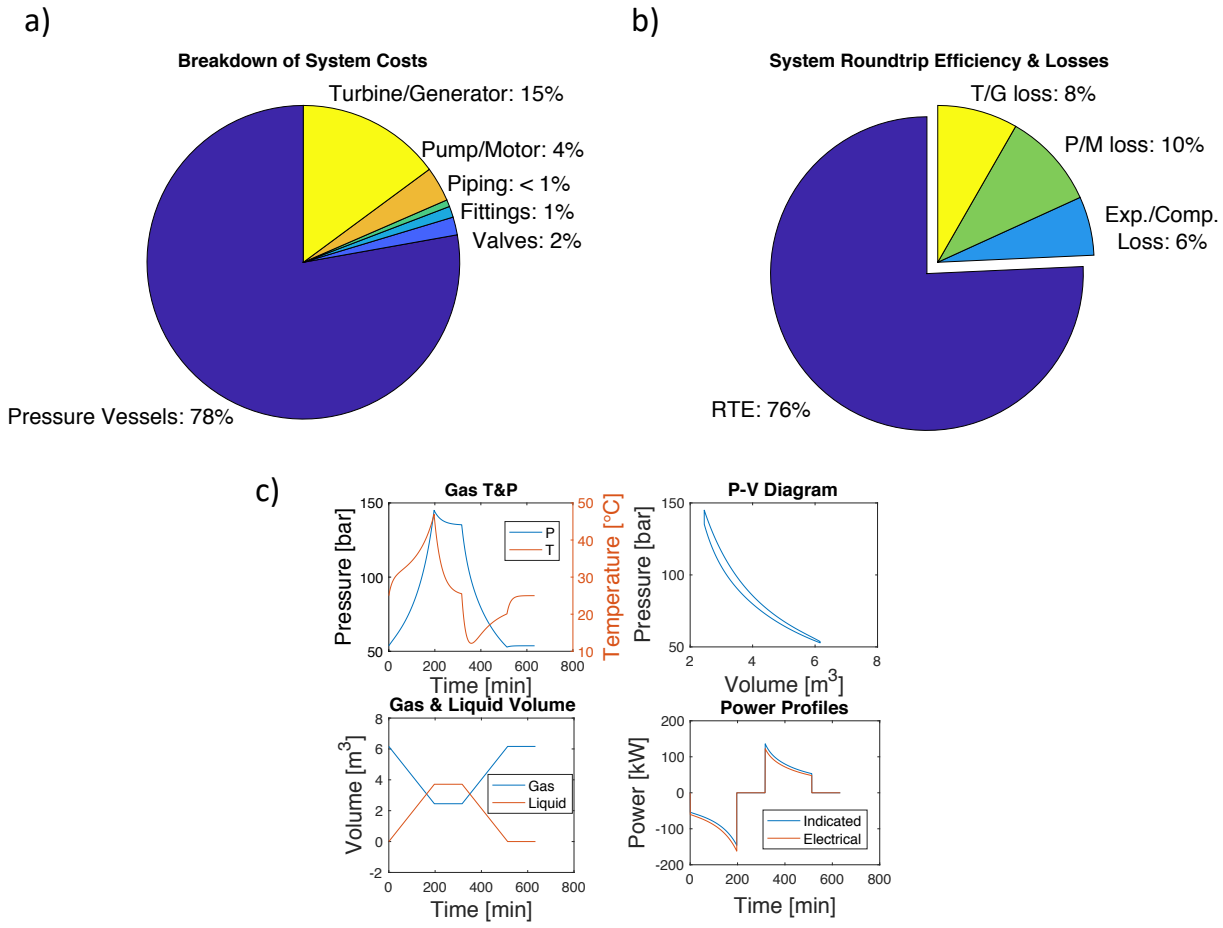

Figure 71, (a) System cost breakdown, (b) roundtrip efficiency/losses, and (c) performance of a 200 kWh system, high-pressure pipe segments.

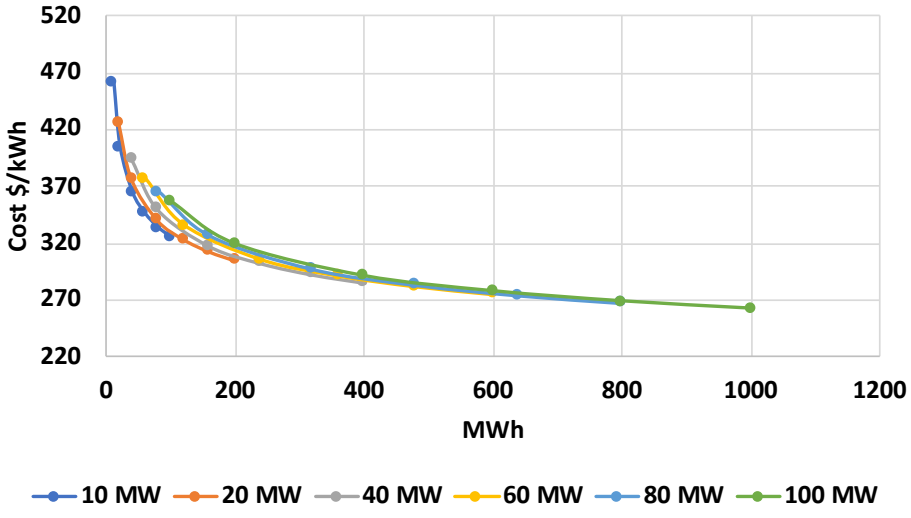

Figure 72, Cost rate of change for a grid-scale GLDIES using high-pressure pipe segments.

Comparing these data for three various pressure reservoirs, by using an isothermal compression process over an adiabatic process, for pipe segments, the energy density increases by 21% and $/kwh capital cost decreased 16%. These data for carbon steel and carbon fiber pressure vessels included an increase of 15% in energy density and decrease of 13% in $/kwh capital cost. Comparing the experimental and isothermal data for various system capacities varying from 1 kW to 1 MW with 2 hours storage time (most beneficial storage time based on the studies done by Abu-Heiba et al. [39] and Chen et al. [32]), it is determined using spray compression, 99% isothermal energy density can be reached using pipe segments, 97% using carbon fiber vessels, and 99% using carbon steel vessels. Other ways to increase GLIDES energy density include using other working gas/fluids including R134a and mineral oil as explained by Odukomaiya et al. [40] or a combination of CO_2 and N_2 as explained by Abu-Heiba et al. [41].

7.4 Cost Reduction Opportunities

Based on the analyzed data using the models discussed in previous sections, energy storage costs as low as ~*$346/kWh* can be achieved for a 60 MWh grid-scale GLIDES using high-pressure pipe segments. This system has an RTE of ~80% and an ED of ~1.46 kWh/m^3 using ~9,000 16-meter-long segments. For comparison, a grid-scale renewable photovoltaic (PV) field capable of producing the same amount of energy (60 MWh) uses around 50,000 PV panels (assuming 1.2 kWh/panel produced in 4 hours each day). As explained in the Results section, most of the cost associated with the GLIDES system is attributed to the pressure vessels. To farther reduce the cost of the system closer to DOE's target, other pressure reservoirs were analyzed including underground reservoirs and abandoned pipelines.

7.4.1 Underground Reservoirs

One cost-reduction option is to use the GLIDES technology underground. Underground reservoirs have been used for natural gas storage for decades [42]. A smaller footprint, larger reservoirs, and lower costs are possible advantages of taking GLIDES underground (Figure 73). Some of the underground reservoirs studied are discussed in this section.

7.4.1.1 Depleted Oil/Gas Reservoir

GLIDES can use depleted oil/gas reservoirs (formed in porous rock) as the pressure reservoir. As the productivity of a well decreases or the well operation is not economical anymore, the operator is required to remove all equipment and seal the abandoned well to prevent leakage. Some wells are plugged, meaning all equipment was removed and the top and bottom of the well was filled with cement as required. In many cases, however, wells are not plugged and are abandoned. This mostly happens when oil prices drop and the operator files for bankruptcy, or in some cases some wells are abandoned, and no operator is filed (especially for wells drilled in early 1980s). Depleted oil and gas reservoirs are the most common underground natural gas storage facilities [43]. These reservoirs occur naturally, but as they are not originally designed to be leak tight, a pressure test is required to determine the maximum pressure the reservoir can practically hold [42]. Around 2.3 million abandoned wells exist in the United States [44,45]. It should be mentioned that most of the depleted fields that were converted to gas storage reservoirs are from depleted gas fields and not oil fields, as the combination of oil, gas, and water causes issues [46]. Typical owners and operators of the storage sites of natural gas are the interstate pipeline companies, distribution companies, and independent companies. The cost associated with using oil and gas reservoirs for storing natural gas is reported between \$5 million and \$6 million per billion ft^3 (between \$177 and \$212 million per billion m^3) [42].

Using Equations (48 and (49, in a 1 billion ft^3 underground reservoir, assuming a maximum pressure range of 10–100 *bar* and around a $1 million cost (around 20 times higher than GLIDES using pressure vessels) associated with the turbomachinery (motor/pump, turbine/generator, and piping), a *$/kWh* cost of *$*13.6/*kWh* to *$*136.91/*kWh* can be achieved, respectively.

7.4.1.2 Aquifers

Another pressure reservoir option for GLIDES is aquifers. They are naturally occurring porous and permeable rock formations which contain freshwater or brine in the pore spaces. Aquifers are typically sandstones or carbonate rocks. Therefore, cap rocks are required in order to make them suitable for storage. Multiple wells can be drilled, depending on geographical conditions, which can give the option of pumping water from two wells into the reservoir and displacing air in another well. Aquifers are known to be capable of storing large volumes of gas. Using this storage volume, water/brine can be pumped down the well to compress existing/compressed air inside the reservoir. Elevation difference and maximum pressure needs to be studied to avoid problems. The air pressure in the reservoir is known to be equal to that of the local water pressure at static conditions when used for CAES. The pressure response of the aquifer is dependent on the permeability of the rock and the viscosity of the fluid, which affects how fast the liquid can flow in the reservoir. The main disadvantage with this system is the low flow rates, which cause this storage type to be only used one annual cycle at steady injection/withdrawal rates. Minimum and maximum mean storage pressures of 20 and 80 *bars* are recommended [42,46,47]. A number of aquifers have operated as natural gas storage reservoirs for many decades.

7.4.1.3 Salt Caverns

Salt caverns could be another underground storage reservoir option for GLIDES. Over the decades, with the oceans and lakes evaporating, the resultant leftover salt was buried underneath layers of

dust. Solution mining is used for extraction of salt from the salt domes or salt beds, which can be as deep as 2 km beneath the surface. Solution mining is done by drilling a well into the salt formation and dissolving the salt by injecting water. As the salt is dissolved in water, the brine is displaced to the earth's surface, creating a large empty space. A blanket medium is injected which has a lower density than both water and brine, keeping the salt in the upper part of the cavern from dissolving in the water to prevent the cavern from collapsing. Leaching can be continued until the planned cavern size is reached; it is recommended not to exceed a height-to-diameter ratio of 5.0 [46,47]. Cavern sealing is not required in solution mined salt caverns due to their low permeability and self-healing characteristics [47]. The cavern construction process can take up to 5 years depending on the desired cavern size (multiple caverns can be mined close to one another to increase the storage volume if desired). As the cavern construction period can be long and the cost expensive, other options can be considered, such as working with salt companies with extensive experience in solution mining or using existing salt caverns. Also, some profit can be made by providing the brine from mining to the salt/chemical companies. Some advantages of using salt caverns for GLIDES technology can include a very large reservoir volume, high safety standards, a much smaller footprint, a much higher RTE than CAES, and a much lower specific investment cost. Some of the disadvantages include the solubility of salt in water (if water is used as the working fluid), which would cause the cavern size and likewise the cavern pressure to change (working fluid/gas would be further investigated). The cost associated with the salt caverns can go upwards of *$*10 *million/Bcf* (*$*353 *million/Bm*^{3}) of working gas capacity. There are two working CAES plants in the world—one in Huntorf, Germany, and one in the United States in Alabama. The CAES plant in Germany consists of two salt caverns which can provide 321 *MW* over a 2 *hour* period and has a total volume of around 310,000 m^3 with a 43 *bar* regular minimum operational

pressure and a 79 *bar* permissible and operational maximum pressure. The Alabama plant can provide 100 *MW* over a 24 *hour* period and has one salt cavern with a volume of around 540,000 m^3 designed to operate between a minimum pressure of 45 *bar* and a maximum pressure of around 74 *bars* [46–48].

Other mining options include hard-rock mining techniques, which can be used to create hard-rock caverns (Figure 74). Hard-rock mining techniques include tunnel boring machine, drilling, and blasting. These caverns can be located at any depth desired with almost any desired shape, but as expected, rock strength improves with depth. Structural strength, low permeability, and adequate volume are required of each selected location. Sealing is most likely needed to prevent leakage in this technique [47]. Hard-rock caverns are expensive, and therefore small scale would be more desirable.

7.4.2 Abandoned Pipelines, Vessels

Pipelines are said to be abandoned when an oil and gas company owner of the pipelines ceases operation and is no longer in need of the pipelines. Regardless of the owner's decision, the pipeline company is required to clean the pipes and if the pipes are to be left in place, the sides must be locked. These pipes could be adapted for use as pressure reservoirs for the GLIDES system. The major cost associated with these pipes mainly involves welding activities. The working pressure of the pipes depends on their thickness.

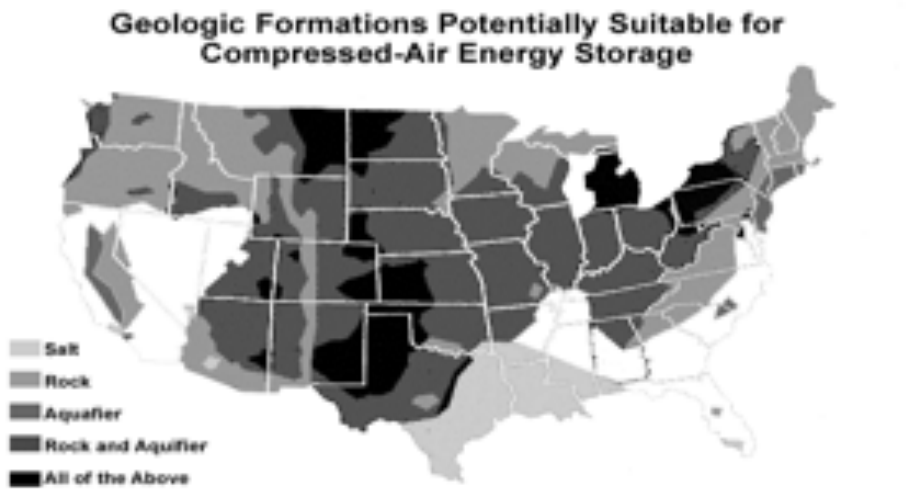

Figure 73, Geologic opportunities for underground storage size in the United States [43].

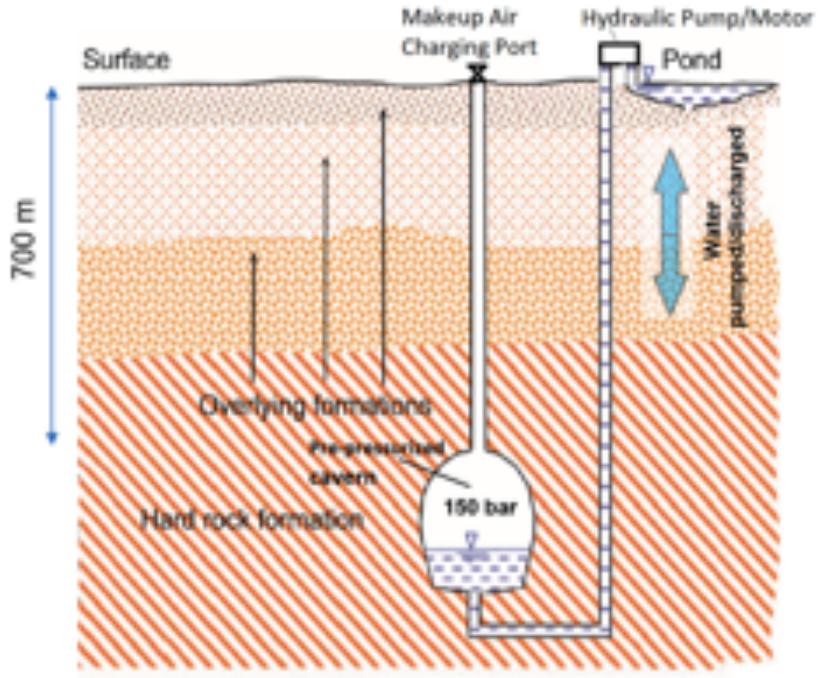

Figure 74, Hard rock cavern as underground reservoir for GLIDES.

Chapter 8: Conclusion

Ground-Level Integrated Diverse Energy Storage (GLIDES) is a hydropneumatics energy storage technology which employs liquid piston and spray cooling to achieve near-isothermal air compression. Using experimental and simulation data, a thorough study on advantages of employing spray compression and expansion on efficiency, energy density, and capital cost in a hydropneumatics energy storage technology, GLIDES, is presented. Based on the experimental data, isothermal compression efficiencies as high as 98.5% are achievable using spray compression. Multiple pressure reservoirs are described, most of which are being used for natural gas storage but can be used for systems like GLIDES, involving water and hydraulic turbomachinery. The advantages of using spray charging also includes as high as 21% increase in energy density compared to an adiabatic compression process and as high as 16% decrease in capital cost $/kwh. The experimental data gathered using the GLIDES 2nd generation prototype along heat transfer equations were used to build a simulation model to further study the behavior of the system. Based on the analyzed data using the models discussed in previous chapters, energy storage costs as low as *~$14/kWh* and *~$346/kWh* (RTE ~80%) can be achieved for a grid-scale GLIDES using depleted oil/gas reservoirs and high-pressure pipe segments respectively. Some advantages of using underground reservoirs include large storage reservoir (grid-scale) and lower *$/kWh* cost; a much smaller footprint compared to above ground reservoirs. Some of the disadvantages of using underground reservoirs include scalability, geographical location with limited access to water reservoirs or renewable energy plants, and hazards, including drinking water contamination. Employing the experimental and analytical data gathered for the GLIDES project, a first in kind near isothermal compressor was designed leveraging the two ORNL studies done on liquid piston compression and advanced heat exchange via micron-sized droplets. A 1st

generation prototype was built at ORNL using a 0.005 m^3 compression chamber and is in characterization process. Based on this research, GLIDES and IsoLiqComp are both promising technologies capable of providing efficient energy storage to stabilize the grid, rising the capacity factor of renewable generation, and provide efficient gas compression to various applications including HVAC systems, natural gas transportation, and CO_2 extraction technologies.

Chapter 9: Future work

As near-isothermal compression has been reached by employing spray compression, to farther increase the GLIDES RTE and ED, farther experimental analysis of isothermal expansion is proposed using spray heating during GLIDES discharge process (Figure 4, c). By employing spray heating, various thermodynamic cycles can be reached resulting in lower losses during GLIDES discharge process, achieving higher RTE. Also, As explained before, improvements to the GLIDES prototypes to increase the technology readiness include improvement in turbomachinery and cost reduction. As GLIDES has extreme head, it requires novel turbomachinery. A new innovative approach is desired to design an efficient and reversible pump/turbine unit to farther increase the GLIDES efficiency and technology readiness for commercialization. Various studies and simulations are needed to analyze specification of the right pump/turbine for scalable GLIDES. Some of these studies can include a) pump size selection for various system sizes and heat transfer needs, b) maximum operating pressure and losses at high pressures, and c) various materials, strength, and frictions. On the other hand, oil and gas wells require clean up after they are no longer profitable and no longer in use as explained before and require costly cleanups. With the power outages due to natural disasters, local energy storage can provide reliability to the grid. Employing abandoned pipelines and depleted oil/gas reservoirs can provide promising low-cost energy storage introducing very competitive market for energy storage. Farther investigation of using such pressure reservoirs and detail studies on system behavior using such pressure reservoirs is beneficial in achieving such low-cost energy storage. Other path to future is to employ Submerged Integrated Diverse Energy Storage (SIDES) to store energy offshore close to offshore windfarms. Farther investigation in this filed invention disclosure is required. The IsoLiqComp

double chamber compressor can provide efficient compression. Integration of this compressor with various technologies including heat pumps gas transportation is required.

References

[1] Hollett D. Grid Modernization Initiative. 2015.

[2] Energy Information Administration U. U.S. Battery Storage Market Trends. Washington, DC: 2018. doi:10.1136/ard.2007.083022.

[3] REN21. Ren21: Renewables 2018 global status report. 2018. doi:978-3-9818911-3-3.

[4] Los Angeles Times. California Assembly advances 100% clean energy bill - Los Angeles Times 2018. http://www.latimes.com/politics/la-pol-ca-renewable-energy-goal-bill-20180828-story.html (accessed November 4, 2018).

[5] California ISO. 2019 Annual Report On Market Issues & Performance 2020.

[6] DOE OE Global Energy Storage Database | Energy Storage Systems 2020. https://www.sandia.gov/ess-ssl/global-energy-storage-database-home/ (accessed December 6, 2020).

[7] May GJ, Davidson A, Monahov B. Lead batteries for utility energy storage: A review. J Energy Storage 2018;15:145–57. doi:10.1016/J.EST.2017.11.008.

[8] Dunn B, Kamath H, Tarascon J. Elecfor the Grid : A Battery of Choices 2011;334:928–35. doi:10.1126/science.1212741.

[9] NHA. NHA Pumped Storage Report. Washington, DC: 2018.

[10] Chen H, Cong TN, Yang W, Tan C, Li Y, Ding Y. Progress in electrical energy storage system: A critical review. Prog Nat Sci 2009;19:291–312. doi:10.1016/j.pnsc.2008.07.014.

[11] Luo X, Wang J, Dooner M, Clarke J. Overview of current development in electrical energy storage technologies and the application potential in power system operation. Appl Energy 2015;137:511–36. doi:10.1016/j.apenergy.2014.09.081.

[12] Akhil AA, Huff G, Currier AB, Hernandez J, Bender DA, Kaun BC, et al. DOE/EPRI

Electricity Storage Handbook in Collaboration with NRECA 2016. doi:10.2172/1431469.

[13] Hart D, Sarkissian A. GMU GRID-SCALE BATTERIES CASE STUDY-1 Deployment of Grid-Scale Batteries in the United States. 2016.

[14] U.S. EIA. Annual Energy Outlook 2018 with projections to 2050. Annu Energy Outlook 2018 with Proj to 2050 2018;44:1–64. doi:DOE/EIA-0383(2012) U.S.

[15] Ulvestad A. A Brief Review of Current Lithium Ion Battery Technology and Potential Solid State Battery Technologies 2018. doi:10.4236/gsc.2012.24020.

[16] ARPA-E. GRIDS Program Overview. 2010.

[17] Gyuk I, Johnson M, Vetrano J, Lynn K, Parks W, Handa R, et al. Grid Energy Storage. 2013.

[18] Gür TM. Review of electrical energy storage technologies, materials and systems: Challenges and prospects for large-scale grid storage. Energy Environ Sci 2018;11:2696–767. doi:10.1039/c8ee01419a.

[19] Mongird K, Viswanathan V, Balducci P, Alam J, Fotedar V, Koritarov V, et al. Energy Storage Technology and Cost Characterization Report | Department of Energy 2019.

[20] Aneke M, Wang M. Energy storage technologies and real life applications – A state of the art review. Appl Energy 2016;179:350–77. doi:10.1016/j.apenergy.2016.06.097.

[21] IRENA. Costs and Markets to 2030. Electr Storage Renewables Costs Mark to 2030, Https//WwwIrenaOrg/Publications/2017/Oct/Electricity-Storage-and-Renewables-Costs-and-Markets 2017.

[22] Van de Ven JD, Li PY. Liquid piston gas compression. Appl Energy 2009;86:2183–91. doi:10.1016/j.apenergy.2008.12.001.

[23] Budt M, Wolf D, Span R, Yan J. A review on compressed air energy storage: Basic

principles, past milestones and recent developments. Appl Energy 2016;170:250–68. doi:10.1016/j.apenergy.2016.02.108.

[24] Morgan R, Nelmes S, Gibson E, Brett G. Liquid air energy storage - Analysis and first results from a pilot scale demonstration plant. Appl Energy 2015;137:845–53. doi:10.1016/j.apenergy.2014.07.109.

[25] Coney MW, Stephenson P, Malmgren A, Linnemann C, Morgan RE. Development Of A Reciprocating Compressor Using Water Injection To Achieve Quasi- Isothermal Compression. Int Compress Eng Conf 2002:10.

[26] Qin C, Loth E. Liquid piston compression efficiency with droplet heat transfer. Appl Energy 2014;114:539–50. doi:10.1016/j.apenergy.2013.10.005.

[27] Kersey J, Loth E, Lankford D. Effects of evaporating droplets on shock waves. AIAA J 2010;48:1975–86. doi:10.2514/1.J050162.

[28] Patil VC, Acharya P, Ro PI. Experimental investigation of water spray injection in liquid piston for near-isothermal compression. Appl Energy 2020;259:114182. doi:10.1016/j.apenergy.2019.114182.

[29] Fong IDA, Us CA, Crane SE, Rosa S. (12) United States Patent, 2011.

[30] M. Momen, K. J. Gluesenkamp, O. A. Abdelaziz, E. A. Vineyard, A. Abu-Heiba AOO. Near isothermal combined compressed gas/pumped-hydro electricity storage with waste heat recovery capabilities. 15/254,137, n.d.

[31] Odukomaiya A, Abu-Heiba A, Gluesenkamp KR, Abdelaziz O, Jackson RK, Daniel C, et al. Thermal analysis of near-isothermal compressed gas energy storage system. Appl Energy 2016;179:948–60. doi:10.1016/j.apenergy.2016.07.059.

[32] Chen Y, Odukomaiya A, Kassaee S, O'Connor P, Momen AM, Liu X, et al. Preliminary

analysis of market potential for a hydropneumatic ground-level integrated diverse energy storage system. Appl Energy 2019;242:1237–47. doi:10.1016/j.apenergy.2019.03.076.

[33] Odukomaiya A, Abu-Heiba A, Graham S, Momen AM. Experimental and analytical evaluation of a hydro-pneumatic compressed-air Ground-Level Integrated Diverse Energy Storage (GLIDES) system. Appl Energy 2018;221:75–85. doi:10.1016/j.apenergy.2018.03.110.

[34] Kassaee S, Abu-Heiba A, Ally MR, Mench MM, Liu X, Odukomaiya A, et al. PART 1-techno-economic analysis of a grid scale Ground-Level Integrated Diverse Energy Storage (GLIDES) technology. J Energy Storage 2019;25. doi:10.1016/j.est.2019.100792.

[35] Data sheet PAH pumps; Data sheet PAH pumps. n.d.

[36] Welcome to CoolProp — CoolProp 6.4.1 documentation n.d. http://www.coolprop.org/ (accessed April 2, 2021).

[37] Kassaee S, Odukomaiya A, Abu-Heiba A, Liu X, Mench MM, O'Connor P, et al. Ground Level Integrated Diverse Energy Storage (GLIDES) Cost Analysis. Vol. 6B Energy, vol. 6B: Energy, Pittsburgh, PA: ASME; 2018, p. V06BT08A059. doi:10.1115/IMECE2018-87517.

[38] Tesla Inc. Powerwall | The Tesla Home Battery. TeslaCom 2017. https://www.tesla.com/powerwall (accessed January 8, 2019).

[39] Abu-Heiba A, Gluesenkamp KR, Odukomaiya WO, Momen AM, O'connor PW. Diverse energy storage technology. Oak Ridge Natl Lab ORNL 2018:1–12.

[40] Odukomaiya A, Kokou E, Hussein Z, Abu-Heiba A, Graham S, Momen AM. Near-isothermal-isobaric compressed gas energy storage. J Energy Storage 2017;12:276–87. doi:10.1016/j.est.2017.05.014.

[41] Abuheiba A, Ally MR, Smith B, Momen A. Increasing compressed gas energy storage density using CO2–N2 gas mixture. Energies 2020;13. doi:10.3390/en13102431.

[42] FERC. Current State of and Issues Concerning Underground Natural Gas Storage. 2004. doi:AD04-11-000.

[43] EPRI, U.S. Department of Energy. EPRI-DOE: Handbook of Energy Storage for Transmission & Distribution Applications. vol. 2. 2003. doi:1001834.

[44] Fall MW, Avery ML, Campbell T a., Egan PJ, Engeman RM, Pimentel D, et al. Rodents and other vertebrate invaders in the United States. Biol Invasions 2011:381–410. doi:10.1002/2015GL067623.Received.

[45] Raza A, Gholami R, Rezaee R, Bing CH, Nagarajan R, Hamid MA. Well selection in depleted oil and gas fields for a safe CO2storage practice: A case study from Malaysia. Petroleum 2017;3:167–77. doi:10.1016/j.petlm.2016.10.003.

[46] Kruck O, Crotogino F, Prelicz R, Rudolph T. Overview on all Known Underground Storage Technologies for Hydrogen. 2013.

[47] Kushnir R, Ullmann A, Dayan A. Thermodynamic and hydrodynamic response of compressed air energy storage reservoirs: A review. Rev Chem Eng 2012;28:123–48. doi:10.1515/revce-2012-0006.

[48] American petroleum Institute. Design and Operation of Solution-mined Salt Caverns Used for Liquid Hydrocarbon Storage. 2018.

Vita

Saiid Kassaee was born in Denton, Texas and grew up in Tehran, Iran since he was 2 years old. He moved back to the United States when he was 20 years old with hopes to achieve higher education. During his first two years, he attended Pellissippi State Community College and continued to finish his Bachelor of Science degree in Aerospace Engineering at the University of Tennessee in Knoxville TN. After completing his Bachelor of Science degree, he decided to take a year off from school to give himself some time to decide what his next step would be while working for American Airlines. During his year off, he got the chance to travel round the earth visiting 5 countries. Deciding to pursue higher education, he pursued his PhD in Mechanical Engineering at the University of Tennessee while doing research at Oak Ridge National Laboratory and continued working at American Airlines. His research interests include energy efficiency, energy storage, grid modernization, and compression efficiency. After graduation, he will begin his new position as research and development staff at Oak Ridge National Laboratory. Saiid is incredibly grateful for all the support from his family and friends as he begins his new career.